



Simplified Control Strategies for Modular
Multilevel Matrix Converter for Offshore
Low Frequency AC Transmission System

Jiankai Ma

A thesis submitted for the degree of

Doctor of Philosophy

September, 2018

School of Engineering

Newcastle University

United Kingdom

Abstract

The Low frequency AC (LFAC) transmission system is considered as the most cost-saving choice for the short and intermediate distance. It not only improves the transmission capacity and distance but also has higher reliability which makes it more advantageous than the HVDC transmission system. Modular Multilevel Matrix Converter (M^3C) is recognized as the most suitable frequency converter for the LFAC transmission system which is responsible for connecting 16.7 Hz and 50 Hz ac systems. In such applications, the ‘double $\alpha\beta 0$ transform’ control method is most popular technique that realizes the decoupled control of the input current, output current and circulating current. However, the derivation process of the mathematical model is so complicated that it gives too much burden on the controller of the M^3C system.

Therefore, this thesis is focusing on simplifying the M^3C control strategies when used in LFAC systems and the primary contribution to the knowledge is outlined as follows:

- (1) A simplified hierarchical energy balance control method which employs an independent control for each of three sub-converters in M^3C is proposed in Chapter 5. The output frequency circulating current is injected and utilized to balance the energy between the three arms of the sub-converter. The proposed method achieves a reduced execution time and a simplified control structure, with which a low-cost processor is applicable and the control bandwidth of the system is improved.
- (2) An improved energy balance control method with injecting both input and output frequency circulating currents is proposed in Chapter 6. The magnitudes of the circulating current responsible for the energy balance control in either frequency are half reduced as compared to the single frequency injection method in Chapter 5. This arrangement alleviates the negative impact of the injected circulating current on the external grid and allows the M^3C systems work through larger grid unbalance situations.

Finally, the effectiveness of the proposed control strategy is demonstrated by extensive simulation results and validated experimentally using a scaled-down laboratory prototype.

Contents

Chapter 1	Introduction	1
1.1	Motivation and objectives	1
1.2	Contribution to knowledge	3
1.3	List of publications	4
1.4	Thesis overview	4
Chapter 2	Literature Review	6
2.1	Transmission systems for the offshore wind farm.....	6
2.1.1	<i>High-voltage Alternating-current (HVAC) transmission system</i>	<i>7</i>
2.1.2	<i>High-voltage Direct-current (HVDC) transmission system</i>	<i>7</i>
2.1.3	<i>Low Frequency AC (LFAC) transmission system</i>	<i>9</i>
2.2	The Modular Multilevel Converters family.....	11
2.2.1	<i>Multilevel Converters</i>	<i>11</i>
2.2.2	<i>The Modular Multilevel Converters family</i>	<i>13</i>
2.3	The Overview of M^3C	17
2.3.1	<i>The history of M^3C.....</i>	<i>17</i>
2.3.2	<i>The modeling and arm power analysis for M^3C.....</i>	<i>19</i>
2.3.3	<i>Capacitor voltage balance control strategy of M^3C.....</i>	<i>20</i>
2.3.4	<i>Research on special working conditions of M^3C.....</i>	<i>21</i>
2.3.5	<i>Research on the failure operation of M^3C.....</i>	<i>22</i>
2.4	Summary.....	23
Chapter 3	Modelling and Analysis of Modular Multilevel Matrix Converter	24
3.1	Circuit topology of M^3C	24
3.2	The mathematical model of M^3C	25
3.3	The mathematical model of sub-module in M^3C	26
3.4	The spectrum analysis of the M^3C arm instantaneous power.....	30
3.5	Illustrative simulation results.....	33
3.5.1	<i>The selection of capacitor and arm inductor</i>	<i>34</i>
3.5.2	<i>FFT Analysis of the capacitor voltage and the arm current.....</i>	<i>34</i>
3.6	Summary.....	36
Chapter 4	The ‘double $\alpha\beta 0$ transformation’ control method of M^3C	37
4.1	The mathematical model of M^3C based on $\alpha\beta 0$ frame	37
4.2	Power analysis based on $\alpha\beta 0$ frame.....	39

4.2	The ‘double $\alpha\beta 0$ transformation’ control method.....	40
4.2.1	<i>Capacitor voltage control</i>	41
4.2.2	<i>Input, output and circulating current control</i>	44
4.3	Illustrative simulation results under output voltage step change operation.....	47
4.3.1	<i>Case I: Steady state operation</i>	47
4.3.2	<i>Case II: Dynamic output power operation</i>	48
4.4	Summary.....	49
Chapter 5	Hierarchical Energy Balance Control Method for M ³ C based on Injecting Output Frequency Circulating Currents	50
5.1	The mathematical model of sub-converter a	50
5.2	The proposed control strategy	52
5.2.1	<i>Sub-converter Energy Balance Control</i>	52
a.	<i>Active and Reactive Power Control</i>	53
b.	<i>Overall capacitor voltage control</i>	54
5.2.2	<i>Energy Balance Control between the three arms of the sub-converter (Capacitor voltage balancing control)</i>	55
5.2.3	<i>The arm current Control</i>	58
5.2.4	<i>Energy balance control between n SMs of each arm (Selective Voltage Mapping Modulation)</i>	58
5.3	Illustrative Simulation Results	60
5.3.1	<i>Case I: Steady-state operation</i>	61
5.3.2	<i>Case II: Dynamic output power operation</i>	62
5.3.3	<i>Case III: Unbalanced grid voltage condition</i>	63
5.4	Summary.....	64
Chapter 6	Hierarchical Energy Balance Control Method for M ³ C based on Injecting Two Frequency Circulating Currents	66
6.1	Circuit topology of M ³ C.....	66
6.2	The mathematical model of M ³ C.....	67
6.3	The Proposed control strategy	69
6.3.1	<i>Energy balance control of M³C</i>	70
6.3.2	<i>Energy balance control between the three arms in the sub-converter A (circulating current control)</i>	72
6.3.3	<i>Energy balance control between three arms of the sub-converter a (circulating current control)</i>	75

6.3.4	<i>The arm current control</i>	78
6.3.5	<i>Energy balance control between n SMs of each arm (SVMM)</i>	79
6.4	Illustrative simulation results.....	79
6.4.1	<i>Case I: Steady-state operation</i>	79
6.4.2	<i>Case II: Dynamic output power operation</i>	80
6.5	Comparison between the ‘double $\alpha\beta$ 0 transformation’ control method and proposed control methods.....	81
6.6	Summary.....	83
Chapter 7	Experimental Validation	84
7.1	Experimental setup	84
7.2	Design and function of M ³ C prototype	85
7.2.1	<i>Distributed control network of M³C prototype</i>	85
7.2.2	<i>Communication Network</i>	88
7.2.3	<i>The design of the software for the distributed control network of M³C</i> ..	92
7.3	The design of the arm board of M ³ C	92
7.4	The design of the full-bridge sub-module	94
7.5	Experimental Results.....	97
7.5.1	<i>The design of the pre-charge and soft-start process of the prototype</i>	98
7.5.2	<i>The experimental results of the Hierarchical Energy Balance Control Method for M³C based on Injecting Output Frequency Circulating Currents</i>	99
7.5.3	<i>The experimental results of the Hierarchical Energy Balance Control Method for M³C based on Injecting Two Frequency Circulating Currents</i>	105
7.6	Summary.....	109
Chapter 8	Conclusions and Future Work	110
8.1	Conclusions	110
8.2	Future work	111
Reference	113

List of Figures

Figure 2.1 Main components of an offshore wind farm: (a) Wind turbines (b) Collection cables (c) Export cables (d) Transformer station (e) Converter station (f) Meteorological mast (g) Onshore stations ^[1]	6
Figure 2.2 Three major offshore transmission systems	6
Figure 2.3 Typical layout of the HVAC transmission system for offshore wind farm	7
Figure 2.4 Typical layout of the HVDC transmission system for offshore wind farm	8
Figure 2.5 Investment for three offshore transmission systems	9
Figure 2.6 The LFAC transmission system based on conventional wind turbines.....	10
Figure 2.7 The LFAC transmission system based on re-designed wind turbines.....	10
Figure 2.8 (a) Three-level NPC (b) Four-level FC	12
Figure 2.9 Categories of the multilevel converters.....	13
Figure 2.10 (a) Half-bridge SM (b) Full-bridge SM (c) Clamp double SM.....	14
Figure 2.11 (a) Five-level cross-connected SM (b) Unipolar-voltage full-bridge SM.....	15
Figure 2.12 Members of the Modular Multilevel Converters family	16
Figure 2.13 (a) Conventional matrix converter (b) First published structure of M ³ C.....	18
Figure 2.14 Circuit diagram of the M ³ C with an arm inductor	19
Figure 3.1 The circuit diagram of Modular Multilevel Matrix Converter.....	24
Figure 3.2 Circuit diagram of sub-converter a in M ³ C.....	25
Figure 3.3 Circuit diagram of the SM in sub-converter a of M ³ C.....	27
Figure 3.4 Status of SM in M ³ C	28
Figure 3.5 Status of SM in M ³ C	28
Figure 3.6 Status of SM in M ³ C	29
Figure 3.7 Status of SM in M ³ C	29
Figure 3.8 The linear steady state model of the arm_{xa}	30
Figure 3.9 The relationship between the frequency ratio and the capacitor voltage ripple ^[95]	32
Figure 3.10 (a) Capacitor voltage (b) FFT analysis of the capacitor voltage	35
Figure 3.11 (a) Arm current (b) FFT analysis of the arm current.....	36

Figure 4.1 The block diagram for the ‘double $\alpha\beta 0$ transformation’ control.....	41
Figure 4.2 The overall capacitor voltage control block diagram.....	42
Figure 4.3 The capacitor voltage balancing control block diagram	44
Figure 4.4 The block diagram of the input current control	45
Figure 4.5 The block diagram of the output current control	46
Figure 4.6 The block diagram of the circulating current control.....	46
Figure 4.7 Simulation results under the steady-state operation.....	48
Figure 4.8 Simulation results under a dynamic output power operation.....	49
Figure 5.1 The circuit diagram of Modular Multilevel Matrix Converter.....	50
Figure 5.2 The block diagram of the proposed control method in sub-converter a	52
Figure 5.3 Active and reactive power control block diagram	53
Figure 5.4 The block diagram of the overall capacitor voltage control	54
Figure 5.5 The block diagram of the capacitor voltage balancing control in sub-converter a	56
Figure 5.6 One possible power exchange path.....	57
Figure 5.7 Arm current control block diagram.....	58
Figure 5.8 (a) Full bridge SM (b) PWM signals of five SMs.....	59
Figure 5.9 PWM signals mapping of SVM.....	60
Figure 5.10 Simulation results under steady-state operation.....	62
Figure 5.11 Simulation results under a dynamic output power operation.....	63
Figure 5.12 Simulation results under unbalanced grid voltage condition	64
Figure 6.1 Circuit diagram for M^3C divided into sub-converters a, b and c	66
Figure 6.2 Circuit diagram for M^3C divided into sub-converters A, B and C.....	67
Figure 6.3 The block diagram of the proposed control method in sub-converter a and sub- converter A	70
Figure 6.4 Active and reactive power control block diagram	71
Figure 6.5 The overall capacitor voltage control block diagram.....	71
Figure 6.6 The block diagram of the capacitor voltage balancing control in sub-converter A	73

Figure 6.7 An example power exchange path (a) Sub-converter A (b) Sub-converter a, b and c.....	74
Figure 6.8 The block diagram of the capacitor voltage balancing control in sub-converter a	76
Figure 6.9 An example power exchange path (a) Sub-converter a (b) Sub-converter A, B and C.....	77
Figure 6.10 Arm current control block diagram	78
Figure 6.11 Simulation results under steady-state operation.....	80
Figure 6.12 Simulation results under dynamic output power operation.....	81
Figure 6.13 Comparison of the mathematical calculation between three control methods	82
Figure 6.14 Comparison of the operation time between three control methods.....	82
Figure 7.1 Experiment platform of the three phase to three phase M ³ C	84
Figure 7.2 The distributed control network of M ³ C	85
Figure 7.3 Function of the master controller	86
Figure 7.4 Function of the arm controller	87
Figure 7.5 The distributed control network of M ³ C in details.....	87
Figure 7.6 Four typical structures of the communication network.....	88
Figure 7.7 The distributed control network (ring structure) based on EtherCAT for MMC	89
Figure 7.8 Structure of the CAN bus in the distributed control network of M ³ C	90
Figure 7.9 Schematic of the CAN interface	91
Figure 7.10 The communication of the distributed control network by using CAN.....	91
Figure 7.11 The design of the software for the distributed control network of M ³ C	92
Figure 7.12 (a) Circuit diagram of the arm in M ³ C (b) The arm board.....	93
Figure 7.13 Schematic of the DSP controller	93
Figure 7.14 Schematic of the full-bridge SM in M ³ C	94
Figure 7.15 Inner schematic and peripheral circuit of DIPIPM	94
Figure 7.16 Feedback circuit of the fault signal	96

Figure 7.17 The relationship between input current and output voltage of hall voltage sensor.....	96
Figure 7.18 Sampling and processing circuit of the capacitor voltage.....	97
Figure 7.19 An example current flow path at the uncontrolled rectifier stage	98
Figure 7.20 Experimental results of the pre-charge and soft-start process	99
Figure 7.21 Experimental results under steady-state operation.....	100
Figure 7.22 The simulation results of arm current and the corresponding FFT analysis when $f_i=16.7$ Hz and $f_o=50$ Hz.....	101
Figure 7.23 The simulation results of arm current and the corresponding FFT analysis when $f_i=50$ Hz and $f_o=16.7$ Hz.....	102
Figure 7.24 Simulation results of the proposed control method when $f_i=50$ Hz and $f_o=16.7$ Hz	103
Figure 7.25 Experimental results under output frequency step change operation.....	104
Figure 7.26 Experimental results under output voltage step change operation.....	105
Figure 7.27 Experimental results under steady-state operation.....	106
Figure 7.28 Experimental results under output frequency step change operation.....	107
Figure 7.29 Experimental results under output voltage step change operation.....	108

List of Tables

Table 3.1 Switching states of SM in M ³ C	27
Table 3.2 Simulation parameters	33
Table 4.1 Simulation parameters of the proposed control method	47
Table 6.1 The relationship between nine arms and six sub-converters	67
Table 7.1 Experimental parameters of the proposed control methods	97

Acronyms and symbols

List of Symbols

P	Rated active power
E_i	Input phase RMS voltage
f_i	Input frequency
L_i	Input inductance
E_o	Output phase RMS voltage
f_o	Output frequency
L_o	Output inductance
R_o	Load Resistance
L	Arm inductance
L_g	Grid-connected filter inductance
C_g	Grid-connected filter capacitance
f_s	Switching frequency
C_{xyz}	Capacitance of SM's capacitor
U_{Cxyz}^*	Rated dc capacitor voltage
n	Number of SMs per arm
$e_{\alpha_i}, e_{\beta_i}$	Input voltage in the $\alpha\beta 0$ frame
$e_{\alpha_o}, e_{\beta_o}$	Input voltage in the $\alpha\beta 0$ frame
$u_{\alpha\alpha}, u_{\beta\alpha}, \dots, u_{00}$	Nine arm voltages in the $\alpha\beta 0$ frame
$i_{\alpha\alpha}, i_{\beta\alpha}, \dots, i_{00}$	Nine arm currents in the $\alpha\beta 0$ frame
L_e	Equivalent inductance
$p_{\alpha\alpha}, p_{\beta\alpha}, \dots, p_{00}$	Nine arm power in the $\alpha\beta 0$ frame
$U_{C\alpha\alpha}, U_{C\beta\alpha}, \dots, U_{C00}$	DC capacitor voltages in the $\alpha\beta 0$ frame
p_i	Input power
p_o	Output power
i_{d_i}, i_{q_i}	Input current in the dq frame
K_1, K_2, \dots, K_6	Proportional gain
$T_{abc/\alpha\beta 0}, [T_{abc/\alpha\beta 0}]^T, T_{abc/dq}, T_{dq/abc}$	Transformation matrix

$i_{\alpha\alpha}, i_{\beta\alpha}, i_{\alpha\beta}, i_{\beta\beta}$	Circulating current in the $\alpha\beta 0$ frame
ω_o	Angular frequency of the output side
ω_i	Angular frequency of the input side
φ_A	relative phase angle of the input current <i>wrt</i> the input voltage
φ_a	relative phase angle of the output current <i>wrt</i> the output voltage
θ	Rotating frequency of the input or output grid voltage
θ_i	Rotating frequency of the input grid voltage
θ_o	Rotating frequency of the output grid voltage
E_A, E_B, E_C	RMS value of the input voltages
I_A, I_B, I_C	RMS value of the input current
E_a, E_b, E_c	RMS value of the output voltage
I_a, I_b, I_c	RMS value of the output current
arm_{xy}	Each arm in M ³ C
i_{xy}	Output current of the corresponding arm
u_{xy}	Output voltage of the corresponding arm
u_{xyz}	Output voltage of each SM
i_{xy_i}	Input current component
i_{xy_o}	Output current component
i_{xy_cir}	Circulating current component
$i_{xy_cir_i}$	Circulating current component with input frequency
$i_{xy_cir_o}$	Circulating current component with output frequency
u_{Cxyz}	Capacitor voltage of each SM
u_{xyz}	Output voltage of each SM
i_{Cxyz}	Current go through the capacitor of each SM
i_{xyz}	Output current of each SM
u_{xy}	Arm voltage

u_{Cxy}	Sum of capacitor voltages of the corresponding arm
p_{Cxy}	Active power of each SM
p_{xy}	Arm power
w_{xy}	Arm's energy
U_{Cxy}	DC capacitor voltage
u_{Cxa}	Capacitor voltage ripple
ε	Percentage of the capacitor voltage ripple
Δi	Maximum ripple of the arm current
k	E_o/ E_i
h	I_o/ I_i
λ	ω_o/ω_i

List of acronyms

M ³ C	Modular Multilevel Matrix Converter
LFAC	Low Frequency AC transmission system
HVAC	High voltage AC transmission system
HVDC	High voltage DC transmission system
AC	Alternating current
DC	Direct current
SVMM	Selective voltage mapping modulation
MMC	Modular Multilevel Converter
SM	Sub-module
CHBC	Cascaded H-bridge converter
LCC	Line commutated converter
VSC	Voltage source converter
IGBT	Insulated gate bipolar transistor
FFTS	Fractional frequency transmission system
THD	Total Harmonic distortion
NPC	Neutral point clamped converter

FC	Flying capacitor converter
STATOCM	Static synchronous compensator
UPFC	Unified power flow controller
SVM	Space vector modulation
PI	Proportional integral
PWM	Pulse width modulation
FCS-MPC	Finite control set-model predictive control
DSP	Digital signal processor
FPGA	Field-Programmable Gate Array
CAN	Controller area network

Chapter 1 Introduction

1.1 Motivation and objectives

Energy shortage, climate warming and environmental degradation have become the biggest public crises for the sustainable development of human society. Therefore, the transformation to green and low-carbon structure with clean energy and emission reduction has become the priority of all countries in the world. The UK government has set a goal for the deployment of renewable energy for the next decade which is that 20% of the UK's total energy should come from renewable sources [1]. Typically, due to geographic problem and the rapid growing capacity of wind farm. A wind farm is normally very far away from the major power grid or load centers. Considering these cases, the transmission of wind power from remote offshore wind farm has been raised as an important issue. The main task is exploring the way to increase transmission distance and capacity.

Apart from the traditional High voltage AC (HVAC) transmission system and the mature High voltage DC (HVDC) transmission system, the Low Frequency (16.7 Hz) AC (LFAC) transmission system is considering as the solution for the future development of offshore wind farm. The LFAC transmission system has two main advantages: 1) Compared with the HVAC transmission system, the low frequency reduced the charging current which provides higher transmission capacity and longer transmission distance; 2) Compared with the HVDC transmission system, the construction and maintenance cost less since there is only one onshore ac/ac converter for the LFAC transmission system [2].

The onshore ac/ac converter is obviously the most important part of the LFAC transmission system. The most commonly used frequency converter is the cycloconverter. However, it suffers from the heavy harmonics and low power factors which limits its future development [3]-[4]. The Modular Multilevel Matrix Converter (M^3C) has been recognized as the next generation of the ac/ac converter, with merits of high flexibility and scalability, high power quality and being able to control both sides' power factor, but the control of M^3C brings difficulty for the application to the LFAC transmission system.

There are eight current degrees of freedom and nine voltage degrees of freedom in M^3C . Two frequency components from both sides of the ac networks within the arm current cause highly coupled relationship between these degrees of freedom and brings the main challenge in controlling M^3C . The commonly used mathematical model of M^3C is based on the ‘double $\alpha\beta$ transformation’ control method which was proposed in [5] where the control algorithm is designed based on the sophisticated mathematical calculation which requires multiple $\alpha\beta$ transformations to decouple the input current, output current and circulating current. It results in a very complex analysis of the mathematical relationship between the arm power and the capacitor voltage. According to that mathematical relationship, the circulating current which contains both input and output frequency components is used to balance the capacitor voltage. Reference [6] proposed the ‘dq transformation’ control method based on [5] where the current is transformed to dq axis dc signals for a better performance. The capacitor voltage fluctuations of M^3C is significant when the input/output frequency get close to each other. In order to solve this problem, reference [7] reallocates the arm currents by only using inner circulating currents. However, this control method is also developed from [5]. A generalized control method for Modular Multilevel Converter topologies (MMC, M^3C etc.) is proposed in [8]. It presents a current control based on the state-space representation and an optimized arm energy balancing control which has been applied to M^3C as an example. It concluded that reference [5] are boundary cases of their proposed control method and their method has better performance. However, these two methods both need a very complex control algorithm and associated mathematical calculation. Reference [9] proposed the method which decouples the sub-converter currents into positive, negative and zero sequences in order to control the input current, circulating current and output current independently. It uses the negative sequence circulating current, which is running at the input frequency, to balance the inter-arm dc-link voltages within each sub-converter. This idea is similar to the commonly used “negative sequence current injection” methods in the star-connected cascaded H-bridge converters (CHBC) [10]. Several predictive control methods are also developed for M^3C such as [11]. However, predictive control method needs accurate system parameters and a huge amount of real time calculation which makes it less practical.

The focus of this thesis is on the design of the control algorithm for M³C. The simplification of the inter-arm dc-link capacitor voltage balancing control reduced the control complexity and the associated mathematical calculation. More specifically, three main research objectives are as follows:

- Investigate and identify the relationship between the eight current degrees of freedom and nine voltage degrees of freedom in M³C. Quantify the mathematical relationship between the arm power and capacitor voltage which is the major energy balance control elements;
- Design the control algorithm which should not be developed from the commonly used control method to balance the capacitor voltage. The injection of the circulating current should be designed without affecting the input/output side.
- Validate the proposed control methods using an ‘close-to-reality’ simulation model and a real-time three phase-to-three phase M³C (three sub-modules in each arm) laboratory test bench.

1.2 Contribution to knowledge

The original contributions of this research work are concluded as follows:

- A simplified hierarchical energy balance control method with injecting output frequency circulating current is proposed in Chapter 5 to achieve an independent sub-converter control of M³C. The circulating current control has been designed easily and accurately for the purpose of compensating the energy difference between the three arms of each sub-converter. The complexity and associated mathematical calculation has been dramatically reduced compared with earlier methods proposed in the literature, achieving a reduced execution time and a simplified control structure, so that a low-cost processor is applicable and the control bandwidth of the system is improved. Experimental results confirm the simulation results and further demonstrated a comparable performance with other relevant papers presented in the literature.
- An improved energy balance control method with injecting both input and output frequency circulating currents is proposed in Chapter 6. The magnitudes of the circulating current responsible for the energy balance control in either frequency are half reduced as compared

to the single frequency injection method in Chapter 5. This arrangement alleviates the negative impact of the injected circulating current on the external grid and allows the M³C systems work through larger grid unbalance situations.

Furthermore, a distributed hardware control structure of the M³C system is proposed in Chapter 7 to experimentally validate the effectiveness of the proposed two control strategies. This hardware structure is on the basis of the distributed local processor which further alleviates the control burden of the master controller.

1.3 List of publications

The early research has been published as conference papers and further research based on that is written as one journal paper which has been submitted to the power electronics.

[C1] J. Ma, M. Dahidah, V. Pickert and J. Yu, "Simplified Hierarchical Energy Balance Control Method for M³C with Frequency Decoupling Strategy," submitted to the IEEE Transactions on Power Electronics.

[J1] J. Ma, M. Dahidah, V. Pickert and J. Yu, "Modular multilevel matrix converter for offshore low frequency AC transmission system," *2017 IEEE 26th International Symposium on Industrial Electronics (ISIE)*, Edinburgh, 2017, pp. 768-774.

[C2] J. Liu, W. Yao, Z. Lu and J. Ma, "Design and implementation of a distributed control structure for modular multilevel matrix converter," *2018 IEEE Applied Power Electronics Conference and Exposition (APEC)*, San Antonio, TX, 2018, pp. 1934-1939.

1.4 Thesis overview

A brief description of each chapter is as follows: Chapter 2 reviewed three transmission systems for offshore wind farm. M³C which function as the frequency converter is also reviewed in terms of its history of and various control methods. Chapter 3 presents the circuit topology and the mathematical model of the proposed M³C with the spectrum analysis of its arm power. Chapter 4 presents the most commonly used control method of M³C which is names as ‘double $\alpha\beta$ transformation’ control method. Chapter 5 proposed a simplified hierarchical energy balance control method of M³C with injecting output frequency circulating current. Chapter 6

proposed an improved energy balance control method with injecting both input and output frequency circulating currents. Chapter 7 presented the experimental validation based on a small laboratory prototype. Finally, Chapter 8 concluded the work and presented the recommendations for the future work.

Chapter 2 Literature Review

2.1 Transmission systems for the offshore wind farm

Different with onshore wind farms, the offshore wind farm requires the submarine cables to transmit electricity to the onshore grid. Figure 2.1 presents a typical structure of the offshore wind power station [12].

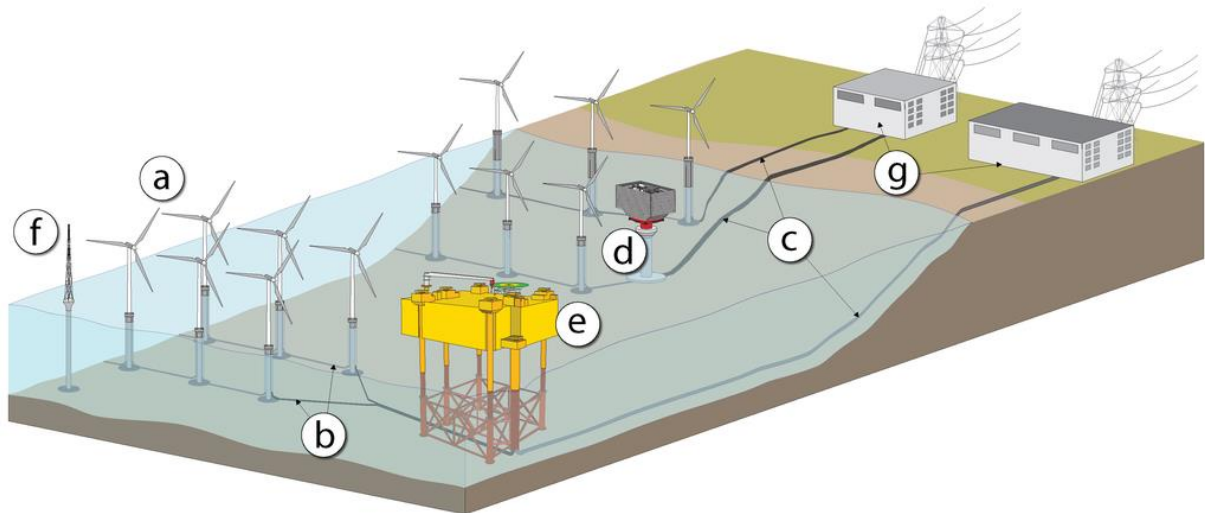


Figure 2.1 Main components of an offshore wind farm: (a) Wind turbines (b) Collection cables (c) Export cables (d) Transformer station (e) Converter station (f) Meteorological mast (g) Onshore stations^[1]

Since the cable length and the transmission voltage are determined by the distance and the rated power of the offshore wind farm, the only variable is the frequency. Currently, there are three major transmission technologies as illustrated Figure 2.2: High-voltage Alternating-current (HVAC) transmission system, High-voltage Direct-current (HVDC) transmission system and Low frequency AC (LFAC) transmission system.

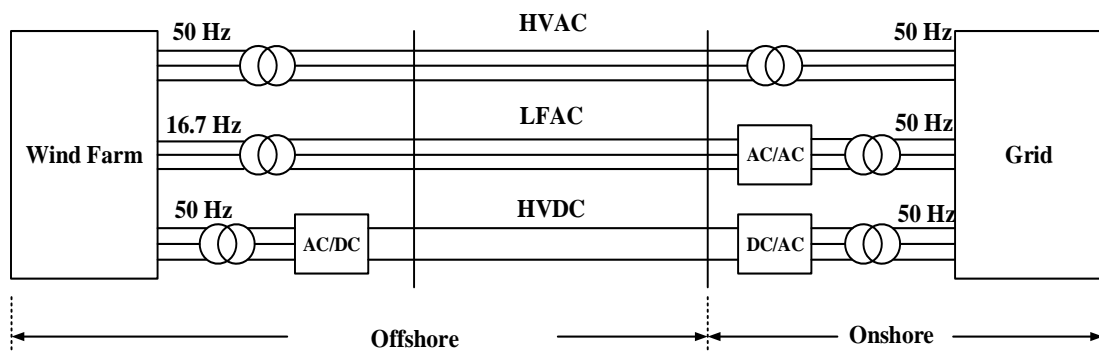


Figure 2.2 Three major offshore transmission systems

2.1.1 High-voltage Alternating-current (HVAC) transmission system

The High-voltage Alternating-current (HVAC) transmission system (operating at 50Hz or 60Hz) is the common choice because of its simplicity of construction [13]. Figure 2.3 shows the typical layout of the HVAC transmission system for offshore wind farm. The submarine cables connect the offshore wind farm and the onshore substation to transmit the electricity.

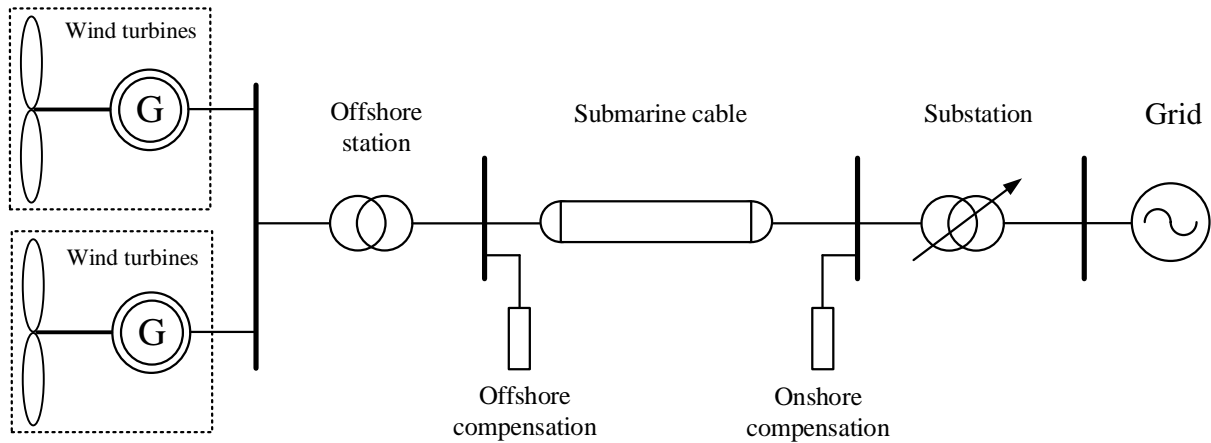


Figure 2.3 Typical layout of the HVAC transmission system for offshore wind farm

However, the submarine cables' high parasitic capacitance generates charging current, which means the reactive power compensation is required before the connection to the grid [14]. Therefore, the HVAC transmission system is less suitable for high capacity offshore wind farm when the transmission distance is long [15]. In addition, when fault situations happen offshore, both sides of the HVAC transmission system will be affected, since the onshore grid is directly connected to the offshore wind farm [16].

2.1.2 High-voltage Direct-current (HVDC) transmission system

Compared with AC transmission technology, DC configurations do not have the charging current or the need for the reactive power compensation. Hence, the High-voltage Direct-current (HVDC) transmission system has been regarded as the best solution for the middle to long range (>150 km) transmission over the last decades. As shown in Figure 2.4, the HVDC transmission system contains three major components which are the offshore converter platform, submarine cables and the onshore converter stations.

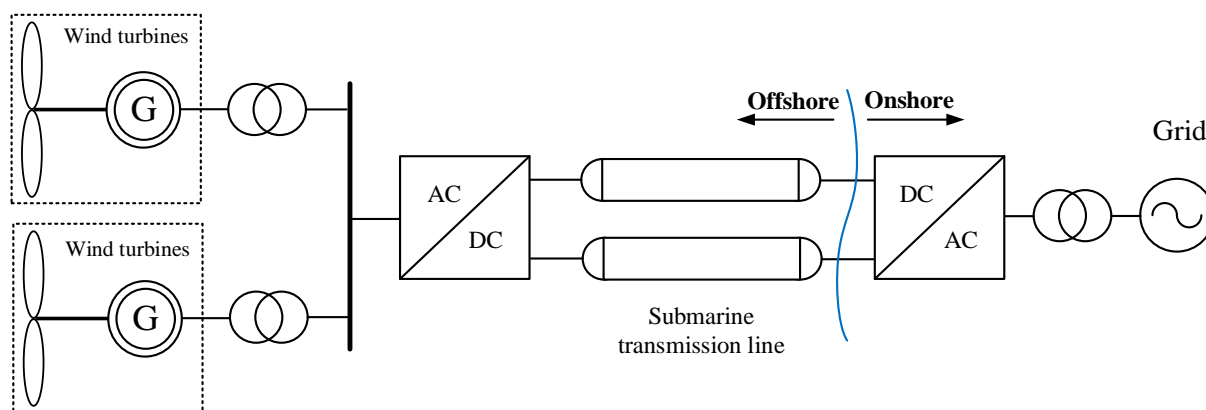


Figure 2.4 Typical layout of the HVDC transmission system for offshore wind farm

The power converters that have been applied in the HVDC transmission system are usually divided into two categories: (1) LCC (Line commutated converters) based on thyristors and (2) VSC (Voltage source converters) based on fully-controllable power switches (such as IGBT). LCC is a mature technology which has been applied to many transmission systems all over the world. However it is still important to mention that the LCC requires strong network on both sides of the converter and additional auxiliary equipment to filter the low-order harmonics [17]. Hence, researchers consider that the HVDC transmission system using LCC is not suitable for offshore wind farm. Conversely, the VSC-HVDC which utilizes the controllable power device realizes the independent control of the active power and reactive power with no commutation failure and low/no extra filter requirement [18]. Although this topology is comparatively new, it has developed so quickly that many existing projects have adopted the VSC-HVDC transmission system [18]-[19]. So far, three main topologies in terms of the power converters are utilized in the VSC-HVDC transmission system: two-level converters, three-level converters and multilevel converters in order to deal with the high voltage and high power transmission [20]. However there still exists technical challenges in the VSC-HVDC transmission system such as the lack of reliable DC circuit breakers and dc/dc transformers [14]. Since an extra converter station needs to be built offshore, it brings many constraints on the design, manufacture and installation of the offshore platform. Therefore, the VSC-HVDC transmission system requires quite a large investment in the construction and maintenance. Some researchers have also stated that the transmission cables have an insulation problem and shorter life time when carrying DC current [21]-[22].

2.1.3 Low Frequency AC (LFAC) transmission system

In addition to the two transmission schemes presented in the previous sub-sections, there is another transmission system which is the Low Frequency AC (LFAC) transmission system. LFAC decreases the transmission frequency to 16.7 Hz thus increasing the transmission capacity and extending the transmission distance when compared with the HVAC transmission system. Compared to the HVDC transmission system, it doesn't need the offshore substation, and instead requires an AC/AC onshore station to transform the low frequency (16.7 Hz) to the desired grid frequency (50 Hz) [23]. As a result, this solution does not only deal with the drawbacks of the HVAC transmission system but also avoids the high investment of the HVDC transmission system. For short and intermediate distance (30 km-150 km), the LFAC transmission system is the most cost-competitive choice. However, when the distance increases further than 150 km, the HVDC transmission system will inevitably become cheaper. Figure 2.5 presents a comparison of investment between the three transmission systems [24]. It should be noted that Figure 2.5 is illustrative and does not present the exact cost of each transmission system.

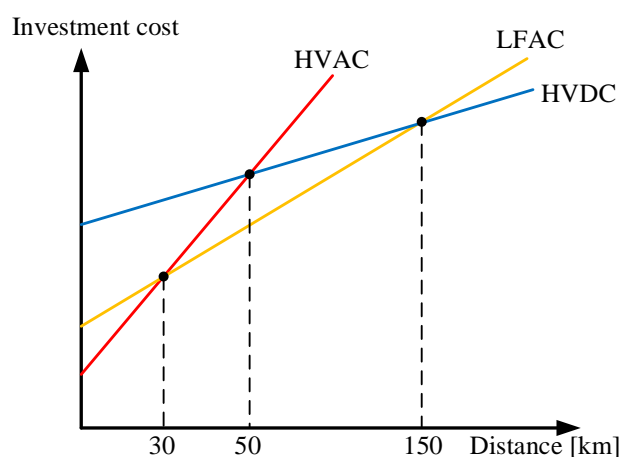


Figure 2.5 Investment for three offshore transmission systems

In 1994 the Fractional Frequency Transmission System (FFTS) was first proposed to increase the transmission capacity for remote hydro power plants [25]. Later, a more comprehensive case study was carried out in [26] which looked at 10000 MW rating wind farms via FFTS. In 2001, the LFAC transmission system was proposed for use in offshore wind farms [27]. Figure 2.6 and Figure 2.7 show two possible designs for LFAC transmission system according to the

different output frequencies of the wind turbines [28]. The design as shown in Figure 2.6 is based on conventional wind turbines (output frequency: 50 Hz) so it does not require extra equipment or modifications. However, an offshore power converter does need to be installed to transform the 50Hz back to the desired low transmission frequency 16.7 Hz.

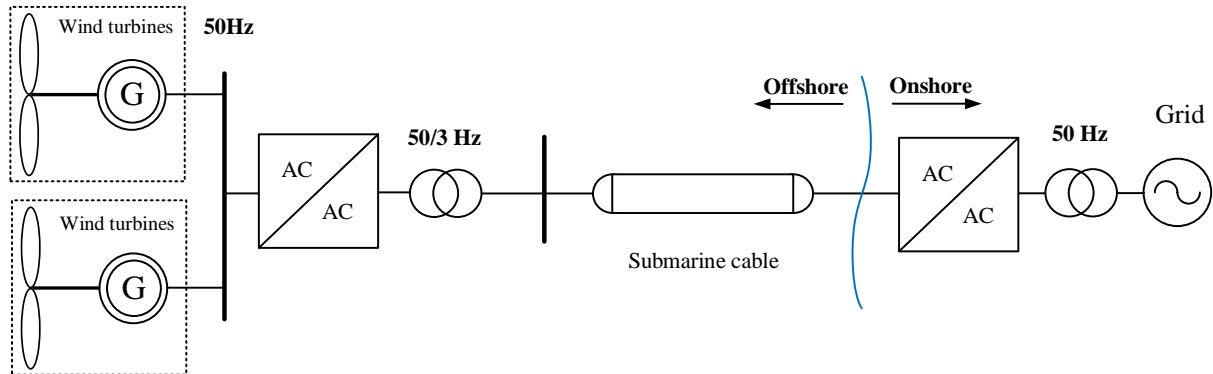


Figure 2.6 The LFAC transmission system based on conventional wind turbines

The second topology is presented in Figure 2.7 where the output frequency of the wind turbines is 16.7 Hz. It means that the offshore frequency converter can be omitted. This largely reduces the maintenance and control complexity. However, the equipment for the conventional three phase power system (50 Hz) requires re-qualification and perhaps alterations. At certain power rating the dimensions of a transformer are inversely proportional to the frequency so that the magnetic core's volume for the transformer offshore will be three times larger than the conventional one [29].

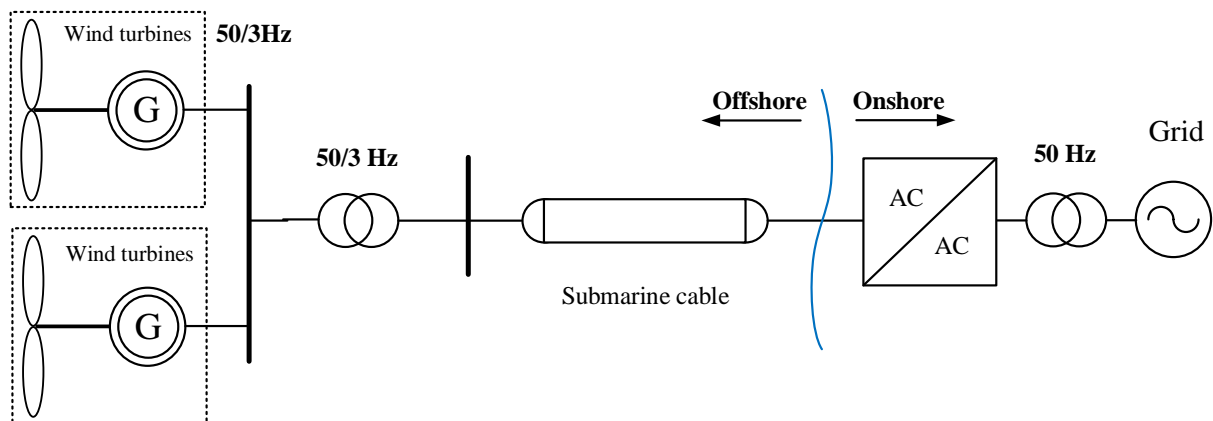


Figure 2.7 The LFAC transmission system based on re-designed wind turbines

Different converters have been considered and discussed in the literature and the 6-pulse cyclo-converter was attempted to triple the frequency in LFAC, from 16.7 Hz to 50 Hz in [30]. Experimental results confirmed its usability but the high total harmonic distortion (THD) makes

it inefficient. A different variation was then presented in [31] where the 6-pulse cycloconverter is replaced by a 12-pulse cycloconverter aiming to reduce the THD. However, as confirmed by [32], the 12-pulse cycloconverter still requires large filters to suppress the lower-order harmonics. Therefore, back-to-back AC-DC-AC converters are considered as an alternative by researchers instead of the conventional AC-AC converter [33]. The Modular Multilevel Converter (MMC) is a mature technology in VSC-HVDC, which apparently the back-to-back arrangement is a good candidate for LFAC system. Reference [34] highlighted that the modular design of MMC provides capability to meet any voltage level requirements. Meanwhile, compared with the cycloconverter, it has a superior harmonic performance [35]. However, as discussed in [30] the structure of the half-bridge sub-module in MMC does not allow clearing the dc bus short circuit fault, which is a major limitation. As the member of Modular Multilevel Converter family, M³C which is the research target of this project will be discussed in details in the later chapters.

2.2 The Modular Multilevel Converters family

2.2.1 Multilevel Converters

Due to the high voltage level of the wind farm, the conventional two-level converters are limited by the voltage rating of the switching devices. To overcome this limitation, there are two possible solutions. The first solution is to improve the voltage rating of the switching devices. For example, this can be achieved by the SiC devices which has been widely researched and applied or using the high blocking voltage switches made by the series connected small voltage rating devices. However, this solution introduces extra voltage and current balancing problems and in addition the high step up voltage will cause the issue of electromagnetic compatibility. The second solution is to use multilevel topologies which means that the voltage level of the converter's output voltage is equal or bigger than three. For example, considering the three-level neutral point clamped converter (NPC) and the four-level flying capacitor converter (FC) as shown in Figure 2.8 (a) and (b) [36].

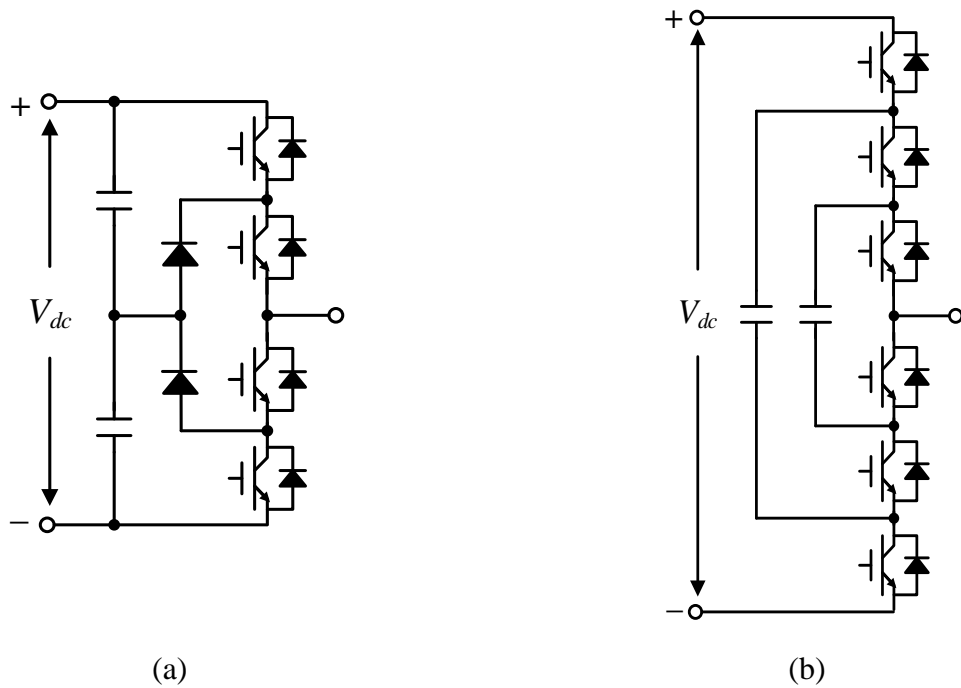


Figure 2.8 (a) Three-level NPC (b) Four-level FC

Compared with the two-level converter, the multilevel converter reduces the dv/dt of the output voltage thus decreasing the output's THD. Meanwhile, the design of the multilevel converter is very helpful in decreasing the switching frequency and the size of the passive filter. Therefore, the multilevel converter is the preferred choice for high power applications and has attracted wide attention in both academic and industrial fields. Figure 2.9 classifies the common topologies of multilevel converters [37].

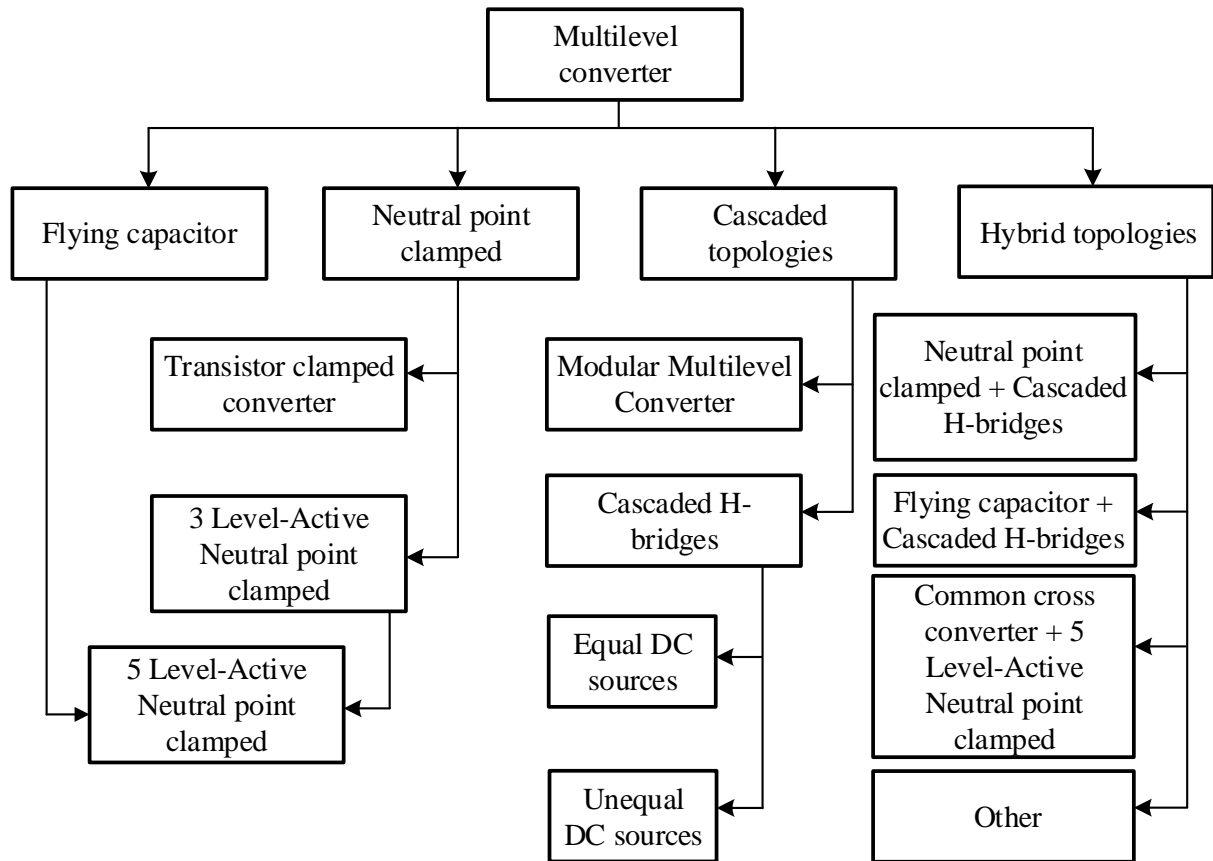


Figure 2.9 Categories of the multilevel converters

2.2.2 The Modular Multilevel Converters family

Modular Multilevel Converter (MMC) is a member of the cascaded topologies family which was first proposed in 2003, by the German researcher, Rainer Marquardt [38]. Compared to other multilevel converters, the MMC utilizes the cascade half-bridge or full-bridge sub-modules (SMs) without the external clamping diode, flying capacitor or transformer. It allows the low voltage rating devices to be applied to medium/high voltage scenarios. Therefore, MMC is not only suitable for high-voltage power transmission system but also can be used for electric drive system at the medium/high voltage rating. The characteristics of such topology are summarized as follows:

- The MMC is composed by SMs and so any voltage level can be easily and flexibly extended via series connected SMs.
- Redundant design can be implemented since all the SMs within the MMC are the same as each other. Once any SM is invalid, it can be quickly replaced by the redundant SMs to

ensure reliability.

- When the number of SMs increase, the equivalent switching frequency of the serial SMs in MMC will also increase. Therefore, the switching frequency of each SM should not be too high in order to reduce the switching loss and improve the efficiency of the converter.

Following continuous research and development, a series of topologies are derived from the MMC. These are named as the Modular Multilevel Converters Family (MMCs) in this thesis. Although, there is not a strict definition for such topologies it has a general and common feature, all topologies are only composed by arms where each arm includes serial basic SMs and one arm inductor. Three common structures of SM is shown in Figure 2.10 which includes the half-bridge SM, the full-bridge SM and the clamp double SM [39]-[40].

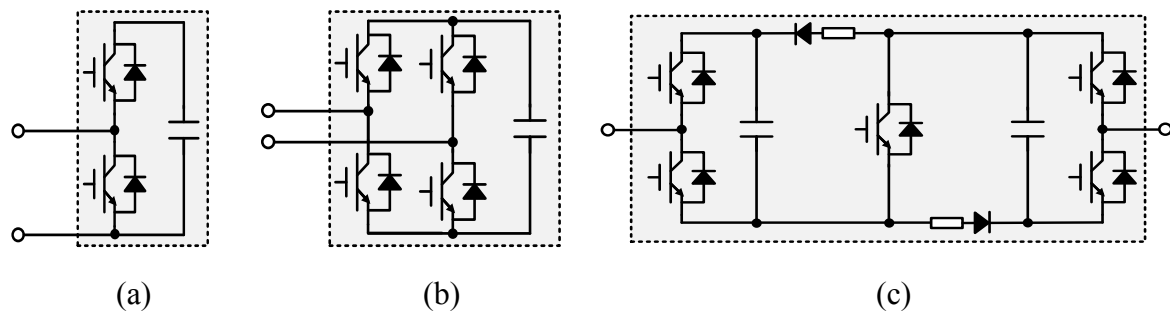


Figure 2.10 (a) Half-bridge SM (b) Full-bridge SM (c) Clamp double SM

The half-bridge SM as illustrated in Figure 2.10(a) is the good option for the DC/AC or the AC/DC converter when only the unipolar arm voltage is required. Therefore, the half-bridge SM is the option with minimal loss in terms of the voltage transformation. However, such SM lacks the capability of handling the DC side short-circuit fault. Once the short circuit fault happens at the DC side of the converter, the anti-parallel diodes in the half-bridge SM still provide the AC energy flow path. As a result, the converter behaves as a rectifier with the short-circuit currents and the DC failures cannot be cleared until the circuit breakers on the AC side are switched on [41]. To solve this problem and ensure the DC fault ride-through capability of the MMCs, researchers proposed two other structures as shown in Figure 2.10(b) and (c). The full-bridge SM is the other typical structure which can provide a bipolar output voltage and hence is suitable for the AC/AC converter. In terms of the DC side short circuit fault, the full-bridge SM can block the arm current by imposing reasonable arm voltage which ensure the DC fault ride-through capability. Compared with the half-bridge SM, the numbers of power

switches are doubled in terms of the full-bridge SM which increases both the cost and the switching losses. Therefore, some scholars proposed a hybrid structure which combines these two kinds of SMs within the one arm. It not only has the DC fault ride-through capability but also needs less power devices and hence generates lower power losses [42]. Another special solution was proposed by Marquardt in 2010 and was named as the clamp double SM as illustrated in Figure 2.10(c) [43]. By increasing additional switches such an SM can be configured as a half bridge or full-bridge SM to ensure the DC fault ride-through capability. It should be noted that the additional switches do not operate at high frequency when choosing switches with good conduction characteristics, which contribute little to the conduction losses. The other two alternative structures of the SM are presented in Figure 2.11. For example, Nami *et al.* [44] connected two half-bridges in a crossed fashion as shown in Figure 2.11(a) which offers similar performance as the clamp double SM. The unipolar-voltage full-bridge SM topology was first proposed in [45], and is a simplification of the conventional full-bridge SM.

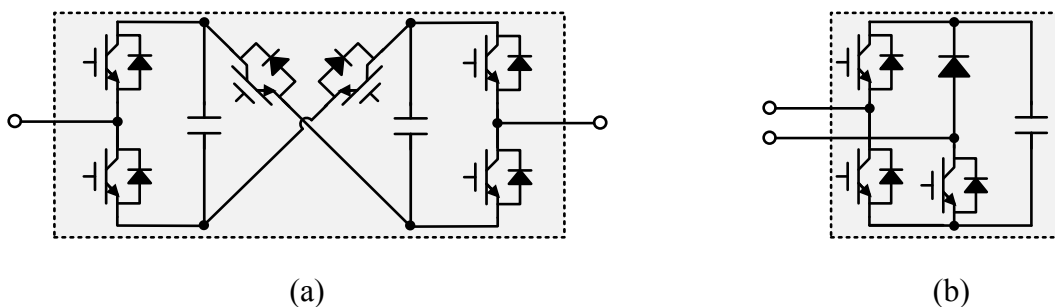


Figure 2.11 (a) Five-level cross-connected SM (b) Unipolar-voltage full-bridge SM

Different structures for the SM have been discussed previously, it is important to mention again that each arm is composed by serial SMs and various combinations of the arm can implement different modular multilevel topologies. The common members in the MMCs are presented in Figure 2.12 [46]. Figure 2.12(a) shows the star-type STATCOM which does not provide active power to the power grid. Compared with the traditional cascade multilevel converter, since it adopts a flying capacitor to stabilize the DC voltage, the DC source can be omitted. Therefore, this topology saves multiple transformers and avoids the energy feedback problem [47]-[48]. As an important part in the flexible AC power transmission system, the STATCOM is one of the most popular research subjects in the power system research area.

The single-phase MMC as shown in Figure 2.12(b) is also proposed by Rainer Marquardt and

Martin Glinka [49]-[50] who applied it to the single-phase AC/AC conversion. They utilized such topology into the high-voltage and high-power electric traction field. The output of the converter is the square wave and connects to the middle-frequency transformer which reduces the transformer volume and omit the filter and resonant circuit.

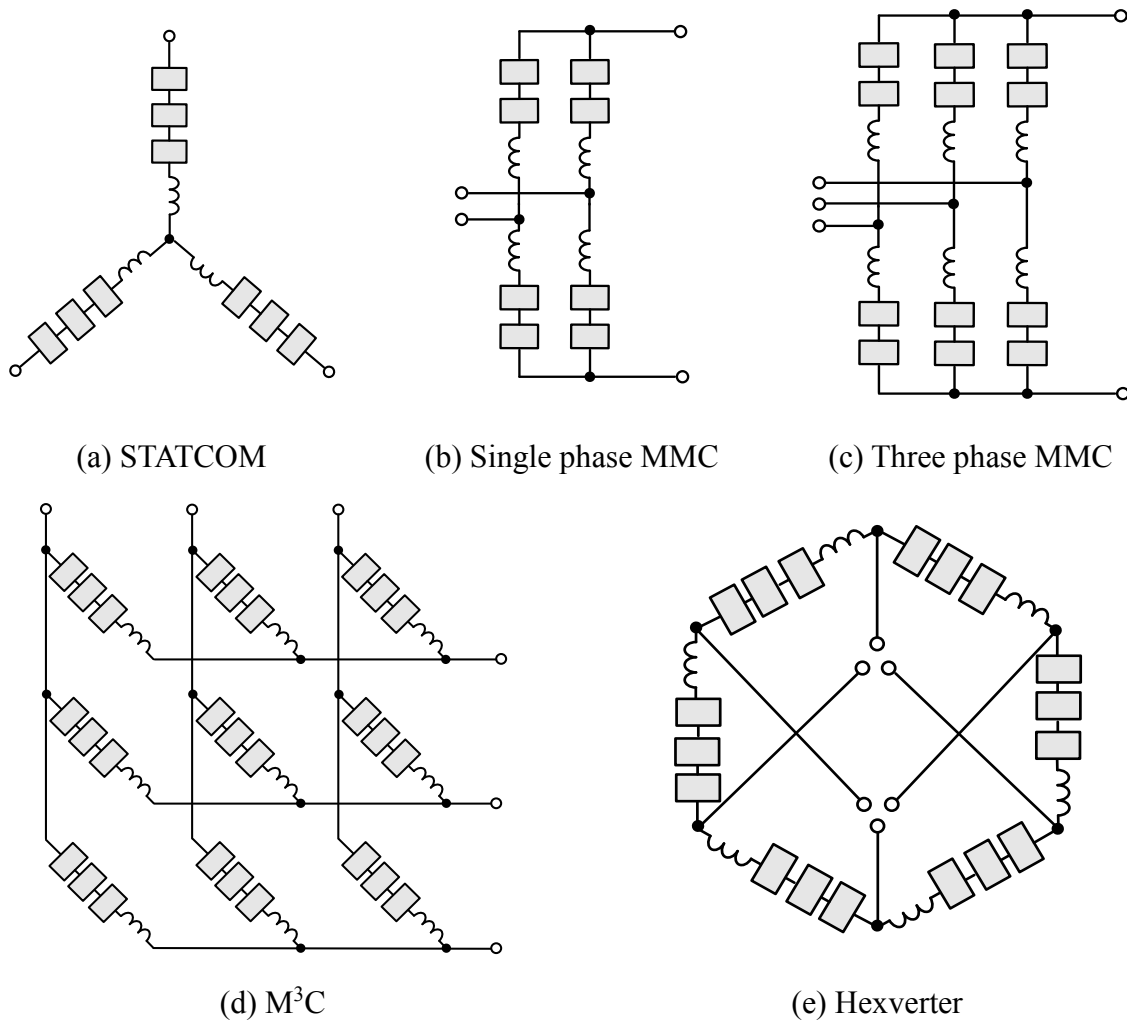


Figure 2.12 Members of the Modular Multilevel Converters family

They also proposed other topologies in the MMCs with any phase of the input and output that can be deduced based on the single phase MMC, including the MMC and M³C as illustrated in Figure 2.12(c) and (d). However, the corresponding control strategy is not discussed in their paper. Based on this fact, other researchers presented the predictive control method for the single phase MMC which minimizes the error in each of the input, output and circulating current control and the DC capacitor voltage balancing control [51].

The Modular Multilevel Matrix Converter (M³C) is one of the very potential topologies and is also a direct AC/AC converter. It is able to realize any power factor of the input and the

bidirectional energy flow [52]. In addition M^3C is very suitable for functioning as the motor drive with the requirement of high torque and low rotation speed such as a mill, conveyor and extruder, etc. [53]. Until now, M^3C has not been applied in industry and still needs further research but it has attracted interests and attentions from researchers and is very likely become a popular research subject in the future.

The Hexverter as illustrated in Figure 2.12(e) reduces by one third of the number of the arms compared with M^3C . Therefore, it has certain advantages such as reducing the quantity and complexity of the hardware but it also reduces the degrees of freedom. If the input and output of the Hexverter have big reactive power difference, then the circulating current and the large common mode voltage should be injected [54]-[55] which will unavoidably increase the system losses. In addition, the Hexverter is regarded as the fault status of M^3C [56] which can improve the failure redundancy capabilities of M^3C . The Hexverter is also used as a high-power, multi-terminal cascade multilevel converter in the unified power flow controller (UPFC) and has good potential for application in the distributed power grid.

2.3 The Overview of M^3C

2.3.1 *The history of M^3C*

As the research target of this thesis, M^3C was first proposed by R.Erickson and O.Al-Naseem from university of colorado in 2001. They were studying how to improve the efficiency of a wind wheel, and they innovatively proposed a new topology based on the features of the traditional matrix converter and multilevel converter [57]. Subsequently the space vector modulation was adapted to control this converter while the single capacitor control strategy was proposed in references [58]-[59]. These studies also confirm the ability of M^3C to overcome the dominated matrix converters' limitation of low voltage conversion ratio (i.e. $E_{out}/E_{in}=0.866$). The three-level matrix converter significantly improves the power transmission efficiency in the variable-speed constant frequency wind power generation especially at a low wind speed. As shown in Figure 2.13(b), the first published M^3C does not have an arm inductor which means each arm is regarded as a controllable voltage source. To avoid the short-circuit situation,

certain restrictions need to be applied to the arm connection and the common control strategy is the space vector modulation (SVM). References [60]-[61] improve the SVM control method by reducing the complexity of calculation via a coordinate transformation. However, when the number of SMs increase, the calculation of SVM will realize multiple of geometric growth which limits the flexibility and scalability of this topology.

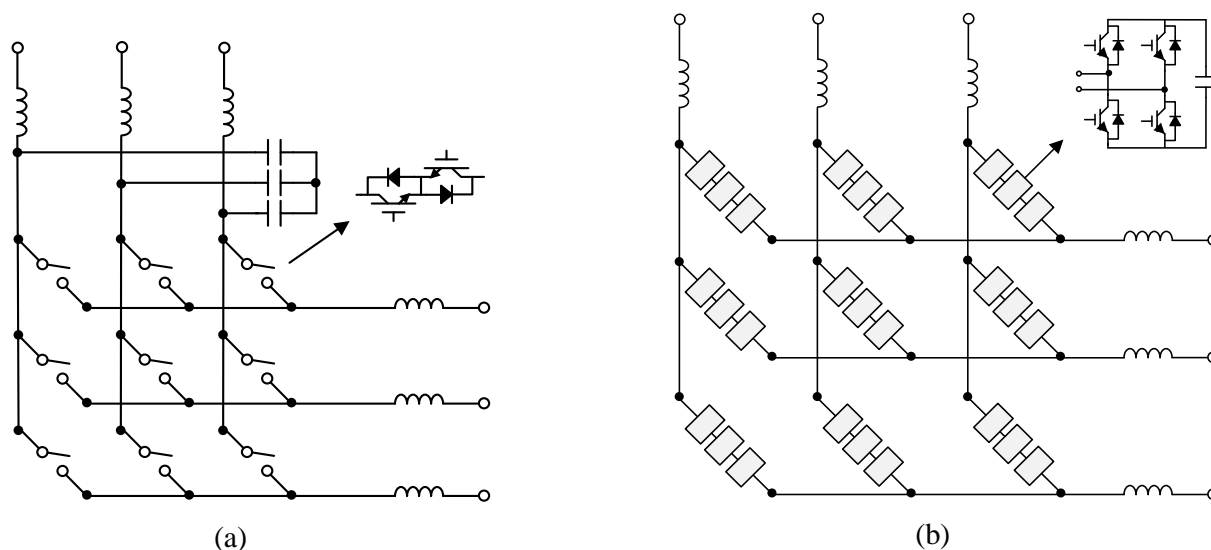


Figure 2.13 (a) Conventional matrix converter (b) First published structure of M^3C

Restricted by the connection principles as discussed previously and the associated control complexity of M^3C , SVM has not received further study for next several years. In order to change this situation, reference [62] proposed an M^3C with an arm inductor as shown in Figure 2.14 which was inspired by the MMC. Each arm is now regarded as a controllable current source to avoid the short circuit possibility. The arm current is controlled by changing the number of SMs that are inserted into the arm. The design and control idea proposed in [62] are the foundation for controlling M^3C .

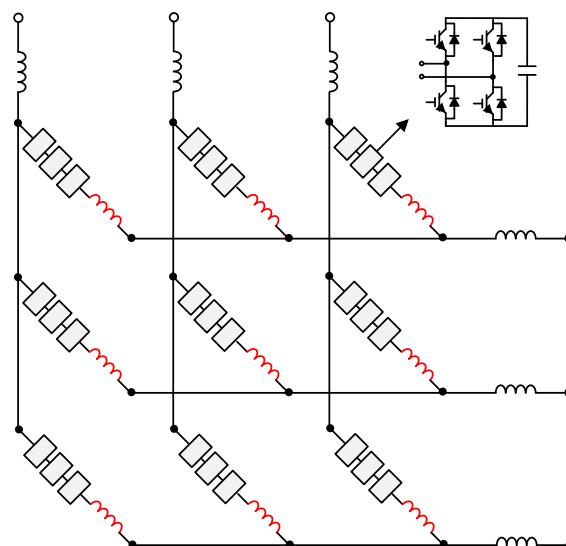


Figure 2.14 Circuit diagram of the M³C with an arm inductor

M³C transfers the active power from the input to the output which means the active power flows through the arms. Therefore, the control difficulty for M³C is balancing the capacitor voltage under the active power transmission condition. It means the secure operation of M³C is mainly determined by the balancing of the capacitor voltage. Reference [63] proposed the capacitor voltage balancing control method based on [62] which used four independent current loops inside of M³C. However, it did not analyze the mathematical relationship between the active power and the capacitor voltage ripple. It only used the sum of the variance between the capacitor voltage and the given value as the cost function for the adjustment of the current loop. However, the author still proposes a new idea for other researchers on how to balance the capacitor voltage.

2.3.2 The modeling and arm power analysis for M³C

It brings the control difficulty since there are nine arms in M³C and its voltage and current components are coupled. Therefore, it is necessary to have the equivalent model for M³C. In order to effectively simplify the mathematical model, the parameters of each full-bridge SM are regarded as consistent which means that each SM can be treated as equivalent to a uniform model. In addition, the dead time and additional circuit or switching losses are ignored.

Until now, the commonly used mathematical model of M³C is based on the ‘double $\alpha\beta 0$ transformation’ control method. The first ‘ $\alpha\beta 0$ transformation’ control method was proposed in

2011. This method decouples the input and output current of M^3C [52]. Then, references [64]-[65] proposed an improved ‘ $\alpha\beta 0$ transformation’ control method in 2012 which was developed based on [52]. It added the balance control of the two diagonal dimensions to decouple the input, output and circulating currents from the nine arm currents in M^3C . References [5], [67] proposed a similar ‘double $\alpha\beta 0$ transformation’ control method in the meantime. The difference between this control method when compared with [52] is that the balance control is based on the $\alpha\beta 0$ transformation of each arm’s output power in M^3C . Finally, four circulating currents are defined as two $\alpha\beta$ components inside M^3C to simplify it as two internal three-phase systems, so that the nine arm currents and arm voltages of M^3C can be represented as four space vectors and one zero vector (common mode component) [68]-[69]. Chile scholars have also applied the same method to MW wind energy conversion system in 2016 and proposed the corresponding control strategy based on that [70]-[72].

Apart from the modelling methods discussed previously, other researchers have divided M^3C into three sub-converters and divided the current flowing through the sub-converters into the positive sequence, zero sequence and negative sequence current. These three currents enable independent control of the input and output current and balancing of the capacitor voltages [9], [73]. Such strategy simplifies the control difficulty and complexity, but it neglects the energy exchange between sub-converters and manually reduces the number of degrees of freedom.

There are also some researchers who analyze M^3C from the view of the matrix state equation [74]. They summarized the laws of MMC, M^3C and Hexverter and proposed a generic mathematical model and control method for the MMCs [8], [75]-[76]. The reference [77] analyzed how to independently control the internal circulating currents in the MMCs’ symmetric topology and presents the deduction for the corresponding transformation matrix.

2.3.3 Capacitor voltage balance control strategy of M^3C

The capacitor voltage balance control is the kernel task for controlling M^3C besides the input and output control. Generally, it includes the arm-level balance control and the SM-level balance control. The latter has been studied thoroughly in the control of MMC where the SM-level balance control methods such as the sorting algorithm and the independent balance control

can be directly applied to M^3C . However, the arm-level balance control of M^3C is more difficult than that of MMC, because both the input and output of M^3C are AC which means the frequency spectrum of the arm power are complicated which makes it hard to derive mathematical equations. The balance control strategy in references mainly utilizes M^3C 's circulating currents or the common mode voltage. Apart from the control methods that have been discussed previously which are all based on the 'double $\alpha\beta 0$ transformation' control method, there are control schemes using the dq frame [6], [78]. However, the author does not give the specific mathematical relationship between each arm's output power and the capacitor voltage under the dq frame. In addition, some predictive control strategies were proposed in [11], [79]-[80]. Similar to MMC, the cascade multilevel topology such as M^3C contains massive state variables. Therefore, the calculation load that is required for finite control set-model predictive control (FCS-MPC) is too heavy to be implemented. The values of the injected circulating current and common mode voltage can be directly calculated according to the feedback of the capacitor voltage which is more practical when compared with other predictive control methods [81].

2.3.4 Research on special working conditions of M^3C

There are mainly four kinds of frequency components in the arm power which cause the fluctuation of the capacitor voltage. The integral of these frequency components are inversely proportional to its frequency which means the frequency component with zero frequency leads to the infinite ripple that fails M^3C .

➤ Special working condition 1: when the output frequency is low

When the output frequency is low, the integral of the second-order harmonic generates large capacitor voltage ripple which affects the steady operation of M^3C .

➤ Special working condition 2: when the input frequency is equal to output frequency

When the input and output frequency are almost equal with each other, the difference frequency component (difference between the input and output frequency) within the arm power will become the dc value and directly affect the balance of the capacitor voltage. The low-pass filter is used to get the dc value of the capacitor voltage and the voltage ripple is usually not controlled. Therefore, two special working conditions as discussed should be paid attention to ensure that

M^3C has the whole range of operation. References [82]-[83] proposed that by using the open-loop injection of the circulating current, the low frequency or difference frequency component is eliminated, which can suppress the low-frequency ripple. Based on that, the additional common mode voltage is added to compensate the active power deviation among the arms in M^3C [67], [84]-[85]. However, these two solutions will increase the system losses. References [7], [86] researched M^3C from the view of the frequency domain. It analyzed the equivalent working points when the input and output frequency are equaled with each other. This solution reallocates the arm current and then the ripple of the capacitor voltage can be suppressed without injecting additional circulating current. Some other scholars discussed the whole range of operation of M^3C from the view of SVM [87]. References [88]-[89] proposed the generalized low-frequency envelope control method which inject the high-frequency circulating current and symmetric-frequency circulation current.

➤ **Special working condition 3: when the output frequency is high**

When M^3C is operating under the working condition with high output frequency, the second-order harmonic in the output frequency is reduced while the second-order harmonic in the input frequency is increased. The fluctuation of the capacitor voltage can be reduced by injecting the circulating currents for compensation which is also meaningful for the reduction of the capacitance [90].

2.3.5 Research on the failure operation of M^3C

Similar to other MMCs' members, M^3C also have the redundancy capability which is a huge advantage for the future industrial application. In terms of MMC, many scholars have proposed various methods for the failure detection [91]. There is no reference that analyzes and discusses the failure detection for M^3C until now. However, researchers did propose the solutions for the failure of the SM. Reference [92] proposed a solution that bypassed the failed SMs and also increased the desired voltage of other serial SMs to ensure the total capacitance of each arm is unchanged. But it did not present experimental results under such condition. When the whole arm is failed, such arm must be cut off which means the nine arms in M^3C are decreased to eight arms. If multiple arms fail, then M^3C is working as the Hexverter which is analyzed in

details in references [55], [93]-[94]. The aim of these references is optimizing the arm current to reduce the loss of the power capacity when the arm failure happens. It realizes the smooth transition between M³C and Hexverter.

2.4 Summary

Three transmission systems for the offshore wind farm have been discussed and compared in this chapter. The LFAC transmission system is the most cost-competitive choice in terms of short to intermediate distance. Meanwhile, the lower frequency (16.7 Hz) enables the increasing of transmission capacity and extending of the transmission distance which makes the LFAC transmission system is the future solution for the offshore wind power transmission. Then, the converters that are suitable for offshore wind power transmission have been presented and M³C in the MMCs is the major research target in this thesis.

Chapter 3 Modelling and Analysis of Modular Multilevel Matrix Converter

3.1 Circuit topology of M³C

Figure 3.1 shows the circuit diagram for M³C, which is functioning as an interface between two power systems with different frequencies. In this work, the input of M³C is connected to the offshore wind farm (16.7 Hz), where the three-phase voltages and currents are denoted by uppercase letters: e_A and i_A ; e_B and i_B ; e_C and i_C respectively. Conversely, the output of M³C is connected to the on-shore grid (50 Hz), where the three-phase output voltages and currents are denoted by lowercase letters: e_a and i_a ; e_b and i_b ; e_c and i_c respectively.

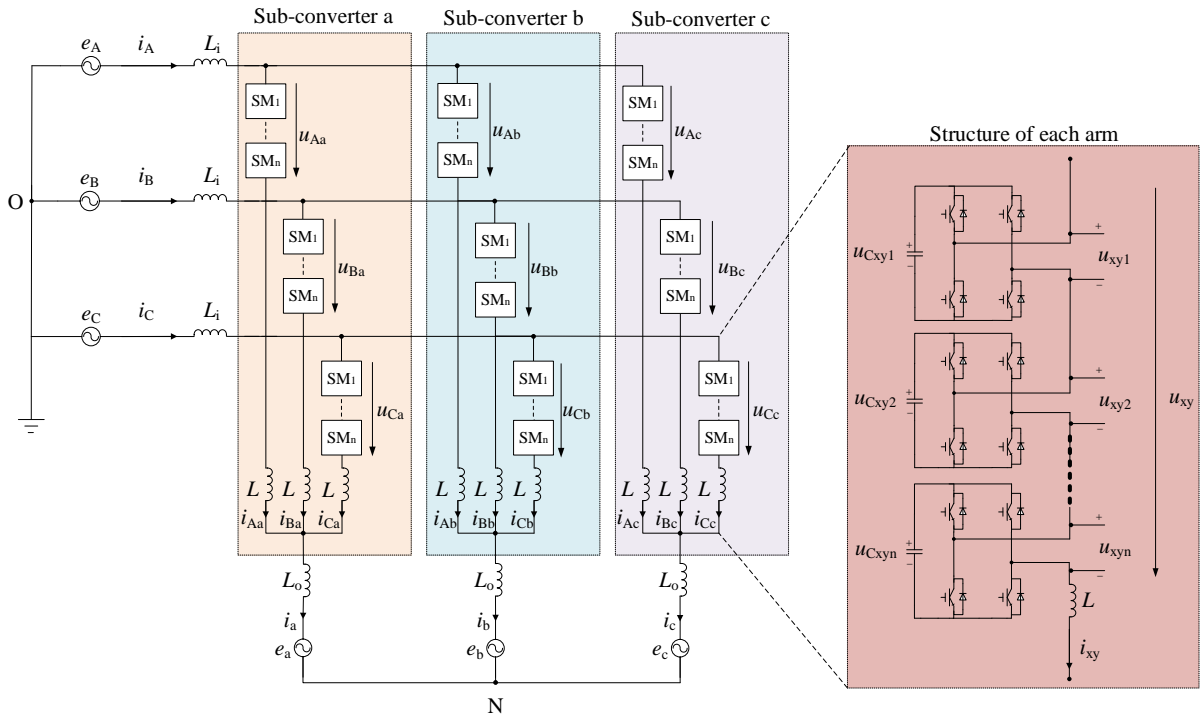


Figure 3.1 The circuit diagram of Modular Multilevel Matrix Converter

Each arm is numbered consecutively according to the three phases of the input and output sides. The input side of each arm is denoted as x (i.e. $x=A, B, C$) according to phase A, B and C, respectively. Similarly, the output side of each arm is denoted as y (i.e. $y=a, b, c$) according to phase a, b and c, respectively. Therefore, each arm in M³C is represented as: arm_{xy} and the arm current of the corresponding arm is: i_{xy} while the arm voltage of the corresponding arm is: u_{xy} . In each arm, there are n SMs connected in series with an arm inductor. Each SM is constructed

from a full bridge converter cell using four IGBT switches with their associated antiparallel diodes and one dc capacitor. The capacitance of each SM's capacitor is denoted by C_{xyz} (i.e. $z=1,2,\dots,n$). The output voltage of each SM: u_{xyz} has three different possible voltage levels, i.e. u_{Cxyz} , 0 and $-u_{Cxyz}$, which are determined by the states of the four IGBT switches.

3.2 The mathematical model of M³C

As illustrated in Figure 3.1, M³C is divided into three identical sub-converters. For simplicity and owing to the symmetry properties, only sub-converter a is considered for deriving the mathematical model in this section. However, this can be equally applied to the other sub-converters of M³C.

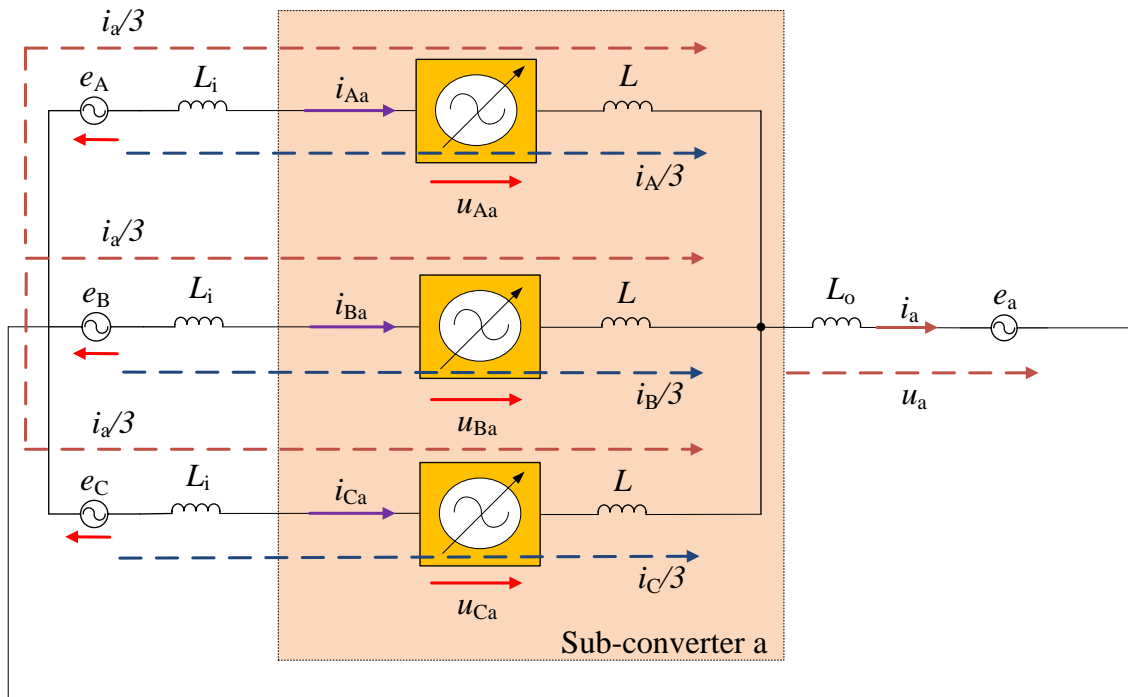


Figure 3.2 Circuit diagram of sub-converter a in M³C

There are two current components in the arm current: input current component and the output current component. For better presentation and discussion in the following chapters, the input is represented by abbreviated letter: i and the output is represented by abbreviated letter: o . Therefore, the arm current in sub-converter a is given by (3.1) as follows:

$$\begin{cases} i_{Aa} = \frac{i_A}{3} + \frac{i_a}{3} \\ i_{Ba} = \frac{i_B}{3} + \frac{i_a}{3} \\ i_{Ca} = \frac{i_C}{3} + \frac{i_a}{3} \end{cases} \quad (3.1)$$

The input and output voltage, current are defined as:

$$\begin{cases} e_A = E_A \cos(\omega_i t) \\ e_B = E_B \cos(\omega_i t - \frac{2\pi}{3}) \\ e_C = E_C \cos(\omega_i t + \frac{2\pi}{3}) \\ e_a = E_a \cos(\omega_o t) \end{cases}, \begin{cases} i_A = I_A \sin(\omega_i t + \varphi_A) \\ i_B = I_B \sin(\omega_i t + \varphi_A - \frac{2\pi}{3}) \\ i_C = I_C \sin(\omega_i t + \varphi_A + \frac{2\pi}{3}) \\ i_a = I_a \cos(\omega_o t + \varphi_a) \end{cases} \quad (3.2)$$

where ω_i and ω_o are the angular frequency of the input and the output side, respectively while φ_A and φ_a are the relative phase angle of the input/output current with respect to the input/output voltage, respectively.

Hence, the arm voltage of sub-converter a can be calculated according to Figure 3.2:

$$\begin{cases} u_{Aa} = e_A - (3L_1 + L) \frac{di_A}{dt} - (3L_o + L) \frac{di_a}{dt} - e_a \\ u_{Ba} = e_B - (3L_1 + L) \frac{di_B}{dt} - (3L_o + L) \frac{di_a}{dt} - e_a \\ u_{Ca} = e_C - (3L_1 + L) \frac{di_C}{dt} - (3L_o + L) \frac{di_a}{dt} - e_a \end{cases} \quad (3.3)$$

3.3 The mathematical model of sub-module in M³C

Figure 3.3 is the circuit diagram of the SM in the sub-converter a of M³C. It is clear that the output voltage and current of the SM is determined from:

$$\begin{cases} u_{xaz} = S_{xaz} \cdot u_{Cxaz} \\ i_{Cxaz} = S_{xaz} \cdot i_{xaz} \end{cases} \quad (3.4)$$

where the switching states of each SM is defined as S_{xyz} ($S_{xyz} \in \{-1, 0, 1\}$).

Therefore, the capacitor voltage of the SM is calculated as:

$$\frac{du_{C_{xaz}}}{dt} = i_{C_{xaz}} \cdot \frac{1}{C_{xaz}} = S_{C_{xaz}} \cdot i_{xa} \cdot \frac{1}{C_{xaz}} = \frac{u_{xaz}}{u_{C_{xaz}}} \cdot i_{xa} \cdot \frac{1}{C_{xaz}} = \frac{p_{xaz}}{u_{C_{xaz}}} \cdot \frac{1}{C_{xaz}} \quad (3.5)$$

where the instantaneous power of each SM is defined as: p_{xyz} .

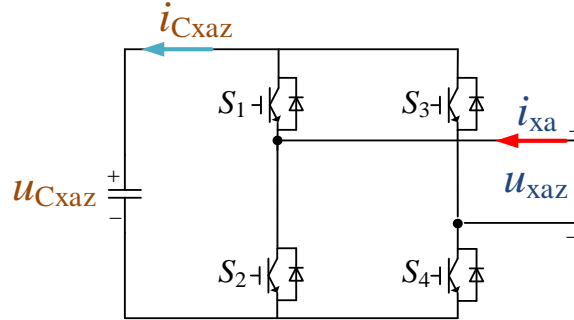


Figure 3.3 Circuit diagram of the SM in sub-converter a of M^3C

According to (3.5), the instantaneous power of each SM is proportional to the differential of the capacitor voltage. Consequently, the dc capacitor of each SM has three states, i.e. charging, discharging and bypassed, according to the switching states of the IGBT switch and the direction of the arm current as shown in Table 3.1 below.

Table 3.1 Switching states of SM in M^3C

Status	S_1	S_2	S_3	S_4	i_{xy}	p_{xy}	u_{xyz}	Capacitor
1	0	1	1	0	<0	>0	$-u_{C_{xyz}}$	Charging
2	0	1	1	0	>0	<0	$-u_{C_{xyz}}$	Discharging
3	1	0	0	1	<0	<0	$u_{C_{xyz}}$	Discharging
4	1	0	0	1	>0	>0	$u_{C_{xyz}}$	Charging
5	0	1	0	1	$>0/<0$	0	0	Bypassed
6	1	0	1	0	$>0/<0$	0	0	Bypassed

As shown in Figure 3.4, when S_1 , S_4 are switched on and S_2 , S_3 are switched off, the SM is connected with the arm and its output voltage is U_C . In the Figure 3.4(a), when the current is positive and it flows through the antiparallel diode of S_1 , S_4 and the capacitor is being charged. Therefore, when the current is negative and the capacitor is being discharged in Figure 3.4(b).

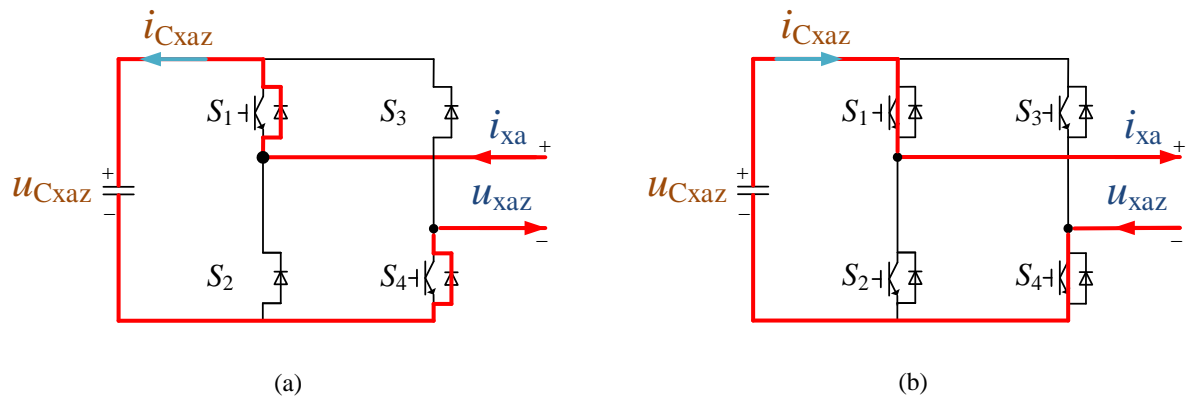


Figure 3.4 Status of SM in M³C

In Figure 3.5, when S_1, S_4 are switched off and S_2, S_3 are switched on, the output voltage of the SM is $-U_C$. In the Figure 3.5(a), when the current is negative and it flows through the switches of S_1, S_4 and the capacitor voltage is being discharged. Thereby, when the current is positive and the capacitor is being charged in Figure 3.5(b).

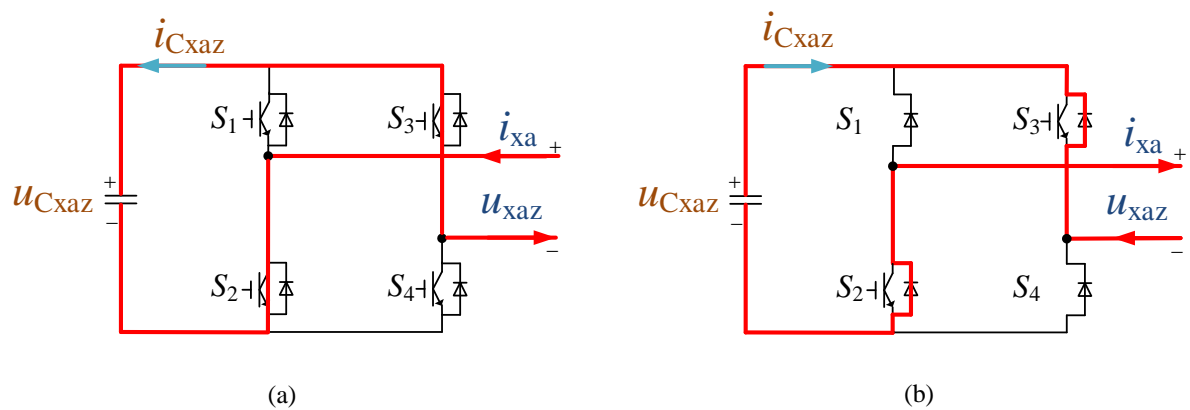
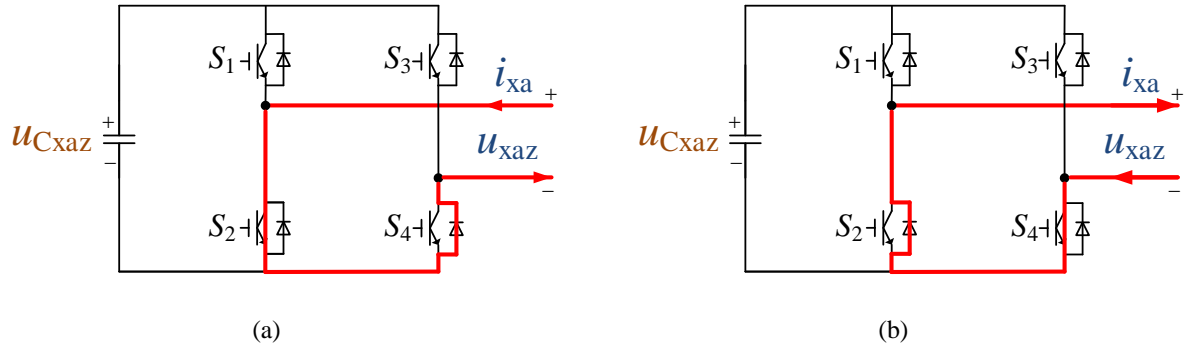
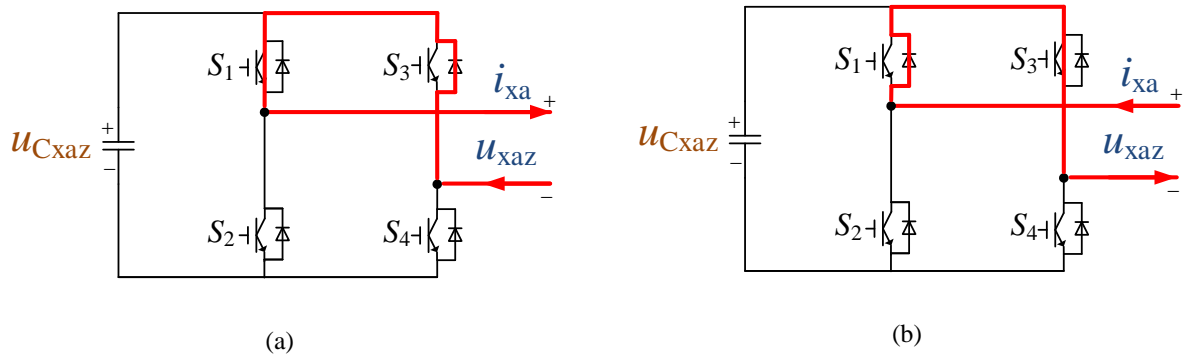


Figure 3.5 Status of SM in M³C

In Figure 3.6, when S_2 and S_4 are switched on, S_1 and S_3 are switched off, the SM is bypassed with zero output voltage. In Figure 3.6(a) and (b), the capacitor is bypassed whether the arm current is positive or negative.

Figure 3.6 Status of SM in M³C

When S_2 and S_4 are switched off, S_1 and S_3 are switched on in Figure 3.7. Its output voltage is zero regardless of the direction of the current.

Figure 3.7 Status of SM in M³C

Then, the mathematical model of the arm_{Aa} is deduced as:

$$\begin{cases} u_{xa} = \sum_{z=1}^N u_{xaz} \\ u_{Cxa} = \sum_{z=1}^N u_{Cxaz} \end{cases} \quad (3.6)$$

Therefore, the differential function of the u_{Cxy} is calculated as:

$$\frac{du_{Cxa}}{dt} = \sum_{z=1}^N \left(\frac{p_{xaz}}{u_{Cxaz}} \cdot \frac{1}{C_{xaz}} \right) \quad (3.7)$$

Under the steady state operation, it is reasonable to assume that the capacitance and the capacitor voltage are all equaled with each other in M³C. Therefore:

$$\begin{cases} u_{Cxa} = n \cdot u_{Cxaz} \\ p_{xa} = n \cdot p_{xaz} \end{cases} \quad (3.8)$$

Hence, (3.5) could be further simplified as:

$$\frac{du_{C_{xa}}}{dt} = \frac{n}{C_{xaz}} \cdot \frac{p_{xaz}}{u_{C_{xaz}}} = \frac{n}{C_{xaz}} \cdot \frac{p_{xa}}{u_{C_{xa}}} \quad (3.9)$$

According to (3.9), it is easy to deduce that when $p_{xa} > 0$, the $\frac{du_{C_{xa}}}{dt} > 0$, which means the capacitors in arm_{Aa} is being charged. Conversely, when $p_{xa} < 0$, the capacitors in arm_{Aa} is being discharged. Thereby, in order to realize the capacitor voltage balance:

$$w_{xa} = \int_t^{t+T} p_{xa} dt = 0 \quad (3.10)$$

It means the active power have to be zero and only reactive power could be stored within capacitors. Assuming the capacitor voltage of arm_{Aa} is composed of dc capacitor voltage $U_{C_{xa}}$ and the ac fluctuation $u_{C_{xa}}$, while $u_{C_{xa}} \ll U_{C_{xa}}$.

$$u_{C_{xa}} = U_{C_{xa}} + u_{C_{xa}} \approx U_{C_{xa}} + \frac{n}{C \cdot U_{C_{xa}}} \cdot \int_t^{t+T} p_{xa} dt = U_{C_{xa}} + \frac{n}{C \cdot U_{C_{xa}}} \cdot \int_t^{t+T} u_{xa} i_{xa} dt \quad (3.11)$$

The linear steady state model is shown in Figure 3.8. The input variables are arm current i_{xa} and the arm voltage u_{xa} .

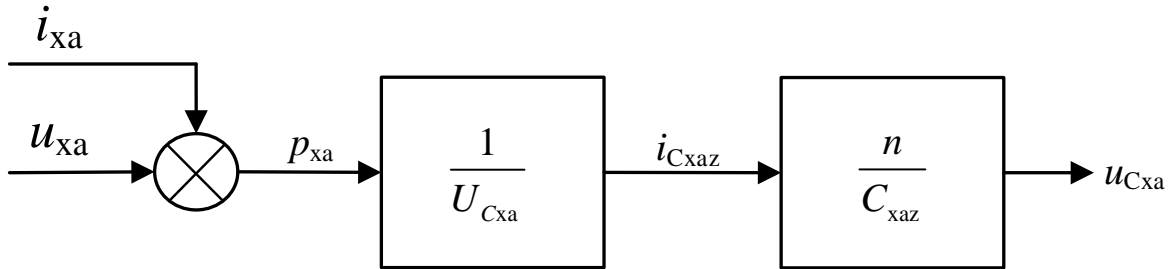


Figure 3.8 The linear steady state model of the arm_{xa}

3.4 The spectrum analysis of the M³C arm instantaneous power

The capacitor voltage balance is the key factor for the steady-state operation of M³C, therefore it is essential to analyze the frequency components that could affect the voltage ripple of the capacitor. In order to simplify the analysis, assuming the system is using open loop control, the input and output is symmetrical and the arm inductance's voltage is neglected while the circulating current is zero. In Figure 3.2, the instantaneous power of arm_{Aa} is given by:

$$p_{Aa} \approx (e_A - e_a) \cdot \frac{1}{3} (i_A + i_a) \quad (3.12)$$

Therefore:

$$\begin{aligned} p_{Aa} &\approx (e_A - e_a) \cdot \frac{1}{3} (i_A + i_a) \\ &= \frac{1}{3} [E_A \sin(\omega_1 t) - E_a \sin(\omega_0 t)] [I_A \sin(\omega_1 t + \varphi_A) + I_a \sin(\omega_0 t + \varphi_a)] \\ &= \frac{1}{6} (E_A I_A \cos \varphi_A - E_a I_a \cos \varphi_a) - \frac{1}{6} E_A I_A \cos(2\omega_1 t + \varphi_A) + \frac{1}{6} E_a I_a \cos(2\omega_0 t + \varphi_a) \\ &\quad - \frac{1}{6} E_a I_A \cos[(\omega_1 - \omega_0)t + \varphi_A] + \frac{1}{6} E_A I_a \cos[(\omega_1 - \omega_0)t - \varphi_a] \\ &\quad + \frac{1}{6} E_a I_A \cos[(\omega_1 + \omega_0)t + \varphi_A] - \frac{1}{6} E_A I_a \cos[(\omega_1 + \omega_0)t + \varphi_a] \end{aligned} \quad (3.13)$$

Assuming that the input power is equal to output power, which means $E_A I_A \cos \varphi_A = E_a I_a \cos \varphi_a$. Therefore, according to (3.11), the ac fluctuation of the capacitor voltage in arm_{Aa} is calculated as:

$$\begin{aligned} u_{CAa} &= \frac{n}{6CU_{CAa}} \left\{ -\frac{1}{2\omega_1} E_A i_A \sin(2\omega_1 t + \varphi_A) + \frac{1}{2\omega_0} E_a i_a \sin(2\omega_0 t + \varphi_a) \right. \\ &\quad - \frac{1}{\omega_1 - \omega_0} E_a i_A \sin[(\omega_1 - \omega_0)t + \varphi_1] + \frac{1}{\omega_1 - \omega_0} E_A i_a \sin[(\omega_1 - \omega_0)t - \varphi_o] \\ &\quad \left. + \frac{1}{\omega_1 + \omega_0} E_a i_A \sin[(\omega_1 + \omega_0)t + \varphi_A] - \frac{1}{\omega_1 + \omega_0} E_A i_a \sin[(\omega_1 + \omega_0)t + \varphi_a] \right\} \end{aligned} \quad (3.14)$$

Thereby, there are four frequency components: u_{CAa, ω_1} , u_{CAa, ω_0} , $u_{CAa, \omega_1 - \omega_0}$, $u_{CAa, \omega_1 + \omega_0}$ and the amplitude of these four frequency components could be calculated as:

$$u_{CAa, 2\omega_1} = \frac{nE_A I_a}{12CU_{CAa} \omega_1} \quad (3.15)$$

$$u_{CAa, 2\omega_0} = \frac{nE_a I_a}{12CU_{CAa} \omega_0} \quad (3.16)$$

$$u_{CAa, \omega_1 - \omega_0} = \frac{n}{6CU_{CAa} |\omega_1 - \omega_0|} \cdot \sqrt{E_A^2 I_a^2 + E_a^2 I_A^2 - 2E_A E_a I_A I_a \cos(\varphi_1 + \varphi_o)} \quad (3.17)$$

$$u_{CAa, \omega_1 + \omega_0} = \frac{n}{6CU_{CAa} |\omega_1 + \omega_0|} \cdot \sqrt{E_A^2 I_a^2 + E_a^2 I_A^2 - 2E_A E_a I_A I_a \cos(\varphi_1 - \varphi_o)} \quad (3.18)$$

As the input side is connected with the offshore wind farm, the parameters are determined,

therefore the parameters of the output side could be defined according to the input side:

$$\begin{cases} k = \frac{E_a}{E_A} \\ h = \frac{I_a}{I_A} \\ \lambda = \frac{\omega_o}{\omega_i} \end{cases} \quad (3.19)$$

As the input side $u_{CAa,2\omega_i}$ is maintained not changed, then the other three frequency components could analyzed based on the $u_{CAa,2\omega_i}$.

$$T_{2\omega_o} = \frac{u_{CAa,2\omega_o}}{u_{CAa,2\omega_i}} = \frac{kh}{\lambda} \quad (3.20)$$

$$T_{\omega_i - \omega_o} = \frac{u_{CAa,\omega_i - \omega_o}}{u_{CAa,2\omega_i}} = \frac{2}{|1 - \lambda|} \sqrt{k^2 + h^2 - 2kh \cos(\varphi_A + \varphi_a)} \quad (3.21)$$

$$T_{\omega_i + \omega_o} = \frac{u_{CAa,\omega_i + \omega_o}}{u_{CAa,2\omega_i}} = \frac{2}{|1 + \lambda|} \sqrt{k^2 + h^2 - 2kh \cos(\varphi_A - \varphi_a)} \quad (3.22)$$

The λ is the key factor. When $\varphi_A = \varphi_a = \pi/2$, $k=2$, $h=0.5$, the relationship between the capacitor voltage ripple and the frequency components is presented in Figure 3.9 [95].

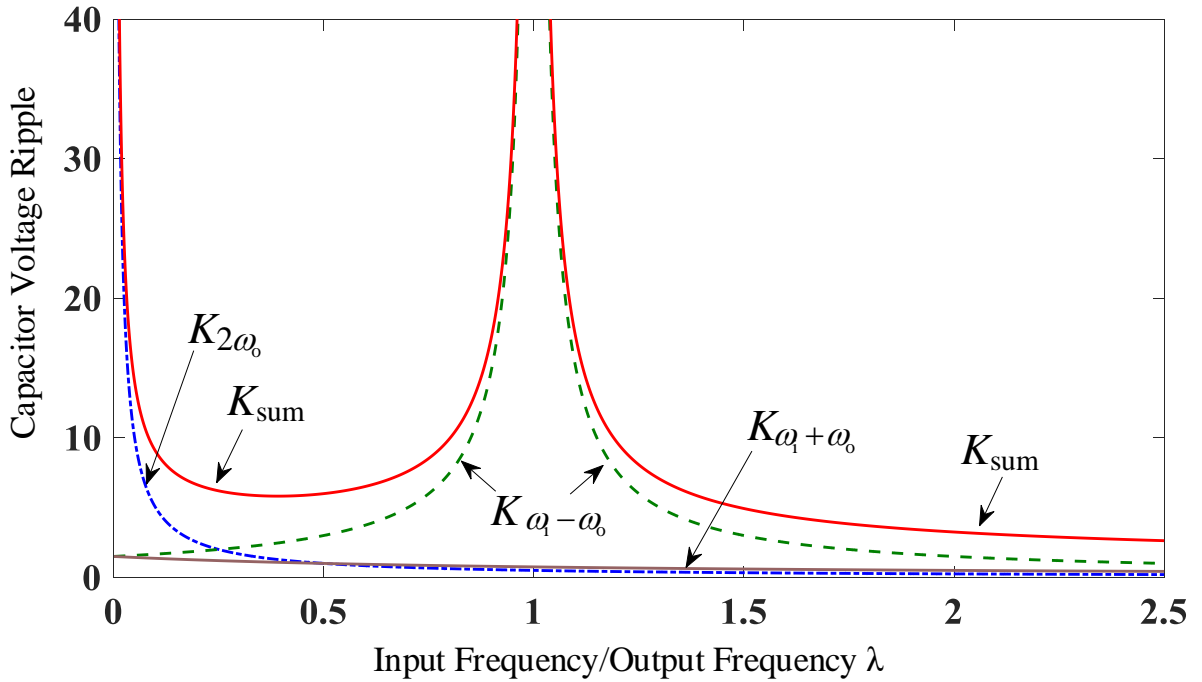


Figure 3.9 The relationship between the frequency ratio and the capacitor voltage ripple^[95]

As shown in Figure 3.9, it is easy to deduce that:

$$\left\{ \begin{array}{l} \lambda = \frac{\omega_o}{\omega_i} \rightarrow 0, T_{2\omega_o} \rightarrow \infty \\ \lambda = \frac{\omega_o}{\omega_i} \rightarrow 1, T_{\omega_i - \omega_o} \rightarrow \infty \end{array} \right. \quad (3.23)$$

Therefore, it is easy to conclude that:

- ◆ When the output frequency is being decreased, the capacitor voltage ripple in the frequency components $2\omega_o$ is increasing which will unbalance the system.
- ◆ When the output frequency is close to the input frequency, the capacitor voltage ripple in the frequency components $\omega_i - \omega_o$ is increasing which will unbalance the system.

3.5 Illustrative simulation results

The simulation model of M³C for LFAC is developed using MATLAB/SIMULINK software. The input side of M³C is connected to the offshore wind farm (16.7 Hz) while the output side is connected with the on-shore power grid (50 Hz). The simulation parameters is shown in Table II. There are five capacitors in each arm. The standard 6.6 kV 1.5 kA IGBT module such as the product from Infineon is considered as the power switch to build the SM. The proposed system is tested under steady-state operating conditions (without circulating current control) to analysis the frequency components of M³C.

Table 3.2 Simulation parameters

Description	Parameters	Value
Rated Active Power	P	10 MW
Input RMS line voltage	E_i	11 kV
Input frequency	f_i	16.7 Hz
Input inductance	L_i	4 mH (3.4%)
Output RMS line voltage	E_o	11 kV
Output frequency	f_o	50 Hz
Output inductance	L_o	4 mH (3.4%)
Arm inductance	L	5 mH (4.3%)

Capacitance of SM's capacitor	C_{xyz}	5.1 mF
Rated dc capacitor voltage	$U_{C_{xyz}}^*$	5 kV
Number of SMs per arm	n	5
Switching frequency	f_s	5 kHz

3.5.1 The selection of capacitor and arm inductor

According to Equation (3.24), there are four kinds of frequency components in the arm power of arm_{Aa} : $2\omega_i$, $2\omega_o$, $\omega_i - \omega_o$ and $\omega_i + \omega_o$. Then the capacitor voltage ripple of arm_{xy} , u_{CAa} , is calculated as:

$$u_{CAa} = \frac{n}{6C \cdot U_{CAa}} \left[\int_0^t (p_{Aa,2\omega_i} + p_{Aa,2\omega_o} + p_{Aa,\omega_i - \omega_o} + p_{Aa,\omega_i + \omega_o}) \right] \quad (3.24)$$

The selection of the capacitance is based on limiting the capacitor voltage ripple within a specified value. As the capacitor voltage ripple should be less than ε , therefore:

$$u_{CAa} \leq \varepsilon \cdot U_{CAa} \quad (3.25)$$

The ε is set as $\pm 10\%$ [95] and considering the experimental parameters, the capacitance of each SM in the simulation and experiment are selected as 5.1 mF and 1 mF, respectively.

The arm inductance is relatively simple to determine by setting up a limitation at the arm current ripple (usually 10% to 15%). The design of the conventional inverter's inductor is considered as a reference therefore the arm inductance is calculated as:

$$L = \frac{0.5(1 + \varepsilon) \cdot U_{CAa} / n}{\Delta i \cdot f_s} \quad (3.26)$$

where Δi is the maximum ripple of the arm current and f_s is the switching frequency.

Hence the arm inductance is calculated as 4 mH.

3.5.2 FFT Analysis of the capacitor voltage and the arm current

Four frequency components in Figure 3.10(a) should be calculated as discussed previously:

$$\begin{cases} \omega_i + \omega_o = 66.7 \text{ Hz}, & 2\omega_o = 100 \text{ Hz} \\ 2\omega_i = 33.4 \text{ Hz}, & \omega_i - \omega_o = 33.4 \text{ Hz} \end{cases} \quad (3.27)$$

Therefore, four frequency components that have been analysed above could be observed in

Figure 3.10(b). It is important to mention that as the simulation is based on the closed loop control, therefore the amplitude of the frequency components is not equal to the value that have been calculated in (3.20).

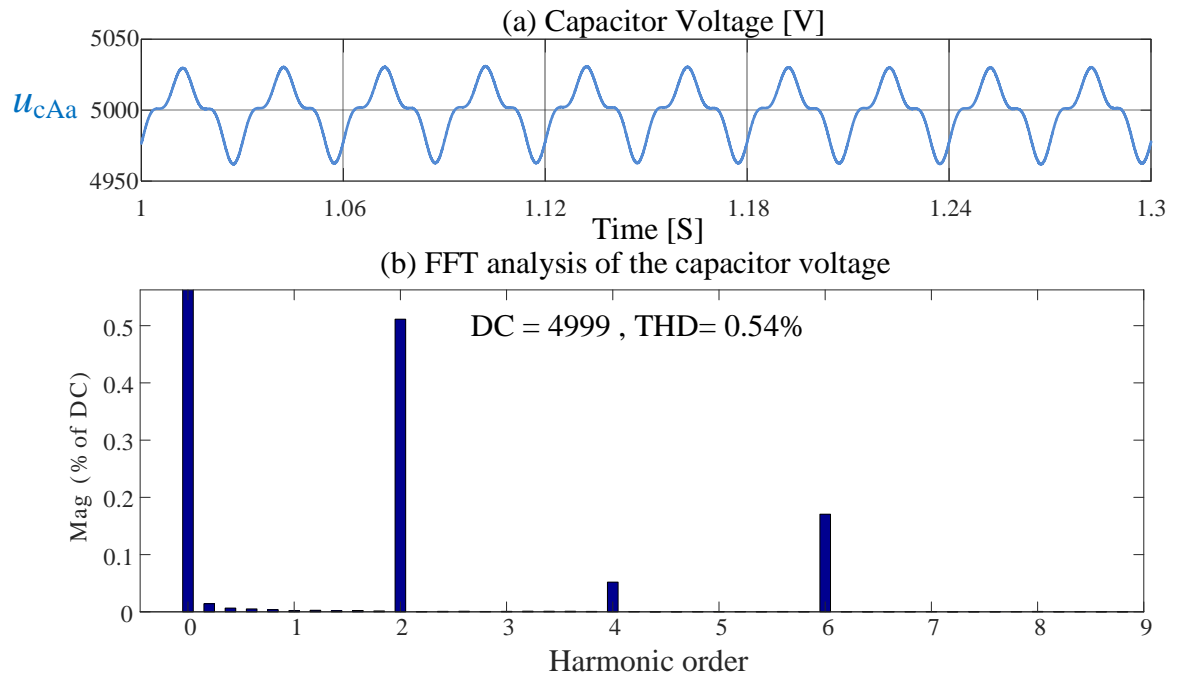


Figure 3.10 (a) Capacitor voltage (b) FFT analysis of the capacitor voltage

According to (3.1), the arm current contains two frequency components: the input frequency component and the output frequency component. This is proved by the FFT analysis of the arm current as shown in Figure 3.11.

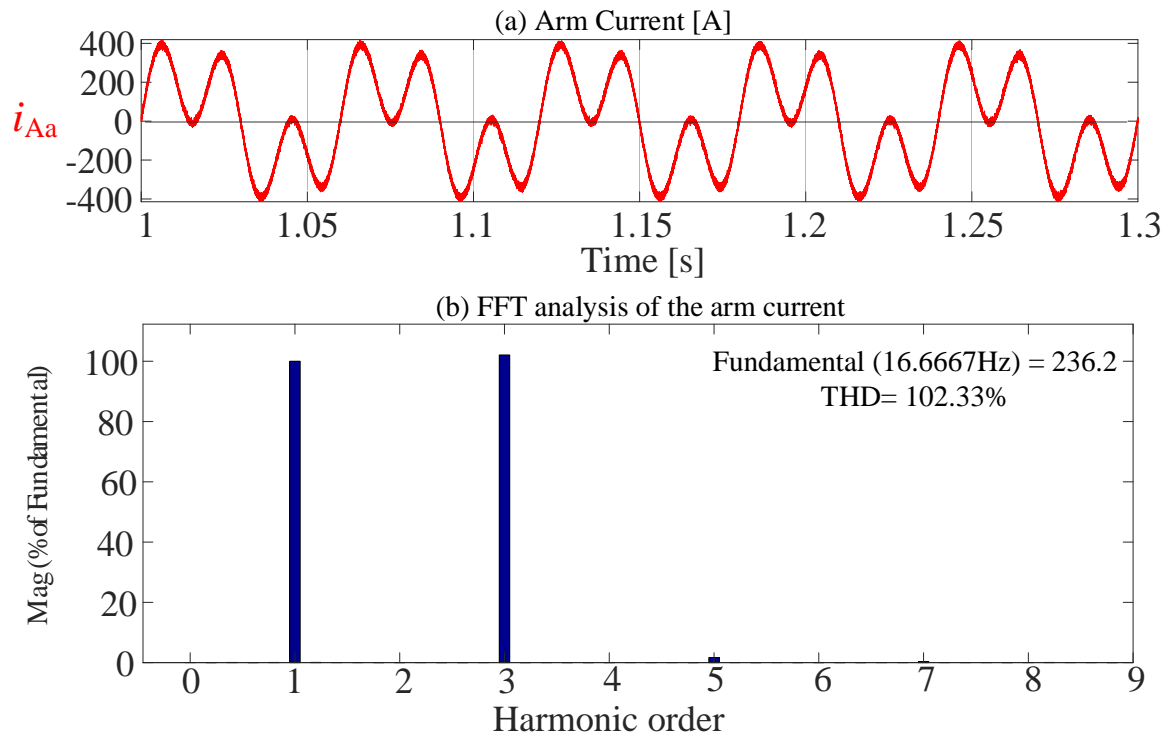


Figure 3.11 (a) Arm current (b) FFT analysis of the arm current

The arm current contains both input and output frequency components, which makes the control of M³C challenging. The main focus of scholars in terms of the control M³C is how to decouple the input and output current, how to balance the capacitor voltage. The following chapters will discuss control methods of M³C in details.

3.6 Summary

This chapter analyzed the relationship between the arm power and the capacitor voltage based on the mathematical model of M³C. The effect of different input/output frequency ratio on the capacitor voltage ripple has been discussed in detail. As the background of this thesis is M³C functioning as the frequency changer for the LFAC transmission system, the input frequency/output frequency ratio is fixed at 1/3. It means that the research of this thesis is not the special frequency ratio cases, and the target of this thesis is to propose a simplified control method as compared to the “double $\alpha\beta 0$ transformation” control method as described as follows.

Chapter 4 The ‘double $\alpha\beta 0$ transformation’ control method of M^3C

The principle of the ‘double $\alpha\beta 0$ transformation’ control method is proposed by references [5] and [52]. As a reference to the proposed simplified control strategy, this control method has been re-derived in detail in this chapter.

4.1 The mathematical model of M^3C based on $\alpha\beta 0$ frame

According to Kirchoff’s law, the arm voltage in M^3C is calculated from:

$$\begin{bmatrix} e_A & e_B & e_C \\ e_A & e_B & e_C \\ e_A & e_B & e_C \end{bmatrix} - L_1 \frac{d}{dt} \begin{bmatrix} i_A & i_B & i_C \\ i_A & i_B & i_C \\ i_A & i_B & i_C \end{bmatrix} = \begin{bmatrix} u_{Aa} & u_{Ba} & u_{Ca} \\ u_{Ab} & u_{Bb} & u_{Cb} \\ u_{Ac} & u_{Bc} & u_{Cc} \end{bmatrix} + L \frac{d}{dt} \begin{bmatrix} i_{Aa} & i_{Ba} & i_{Ca} \\ i_{Ab} & i_{Bb} & i_{Cb} \\ i_{Ac} & i_{Bc} & i_{Cc} \end{bmatrix} + L_o \frac{d}{dt} \begin{bmatrix} i_a & i_a & i_a \\ i_b & i_b & i_b \\ i_c & i_c & i_c \end{bmatrix} \quad (4.1)$$

$$+ \begin{bmatrix} e_a & e_a & e_a \\ e_b & e_b & e_b \\ e_c & e_c & e_c \end{bmatrix}$$

The transformation matrix is defined as:

$$T_{abc/\alpha\beta 0} = \sqrt{\frac{2}{3}} \begin{bmatrix} 1 & -\frac{1}{2} & -\frac{1}{2} \\ 0 & \frac{\sqrt{3}}{2} & -\frac{\sqrt{3}}{2} \\ \frac{1}{\sqrt{2}} & \frac{1}{\sqrt{2}} & \frac{1}{\sqrt{2}} \end{bmatrix} \quad (4.2)$$

In order to transform from an abc frame to an $\alpha\beta 0$ frame, Equation (4.1) should pre-times the $T_{abc/\alpha\beta 0}$ in Equation (4.2). Hence, Equation (4.1) is further calculated as:

$$\sqrt{3} \begin{bmatrix} 0 & 0 & 0 \\ 0 & 0 & 0 \\ e_A & e_B & e_C \end{bmatrix} - \sqrt{3} L_1 \frac{d}{dt} \begin{bmatrix} 0 & 0 & 0 \\ 0 & 0 & 0 \\ i_A & i_B & i_C \end{bmatrix} = \begin{bmatrix} u_{A\alpha} & u_{B\alpha} & u_{C\alpha} \\ u_{A\beta} & u_{B\beta} & u_{C\beta} \\ u_{A0} & u_{B0} & u_{C0} \end{bmatrix} + L \frac{d}{dt} \begin{bmatrix} i_{A\alpha} & i_{B\alpha} & i_{C\alpha} \\ i_{A\beta} & i_{B\beta} & i_{C\beta} \\ i_{A0} & i_{B0} & i_{C0} \end{bmatrix} + L_o \frac{d}{dt} \begin{bmatrix} i_{\alpha_0} & i_{\alpha_0} & i_{\alpha_0} \\ i_{\beta_0} & i_{\beta_0} & i_{\beta_0} \\ i_{0_0} & i_{0_0} & i_{0_0} \end{bmatrix} \quad (4.3)$$

$$+ \begin{bmatrix} e_{\alpha_0} & e_{\alpha_0} & e_{\alpha_0} \\ e_{\beta_0} & e_{\beta_0} & e_{\beta_0} \\ 0 & 0 & 0 \end{bmatrix}$$

Then the Equation (4.3) post-multiplies $[T_{abc/\alpha\beta 0}]^T$. This leads to:

$$\sqrt{3} \begin{bmatrix} 0 & 0 & 0 \\ 0 & 0 & 0 \\ e_{\alpha_i} & e_{\beta_i} & 0 \end{bmatrix} - \sqrt{3}L_i \frac{d}{dt} \begin{bmatrix} 0 & 0 & 0 \\ 0 & 0 & 0 \\ i_{\alpha_i} & i_{\beta_i} & 0 \end{bmatrix} = \begin{bmatrix} u_{\alpha\alpha} & u_{\beta\alpha} & u_{0\alpha} \\ u_{\alpha\beta} & u_{\beta\beta} & u_{0\beta} \\ u_{\alpha 0} & u_{\beta 0} & 0 \end{bmatrix} + L \frac{d}{dt} \begin{bmatrix} i_{\alpha\alpha} & i_{\beta\alpha} & i_{0\alpha} \\ i_{\alpha\beta} & i_{\beta\beta} & i_{0\beta} \\ i_{\alpha 0} & i_{\beta 0} & i_{00} \end{bmatrix} + \sqrt{3}L_o \frac{d}{dt} \begin{bmatrix} 0 & 0 & i_{\alpha_o} \\ 0 & 0 & i_{\beta_o} \\ 0 & 0 & 0 \end{bmatrix} \quad (4.4)$$

$$+ \sqrt{3} \begin{bmatrix} 0 & 0 & e_{\alpha_o} \\ 0 & 0 & e_{\beta_o} \\ 0 & 0 & 0 \end{bmatrix}$$

where, e_{α_i} and e_{β_i} are the input voltage in the $\alpha\beta 0$ frame. i_{α_i} and i_{β_i} are the input current in the $\alpha\beta 0$ frame. e_{α_o} and e_{β_o} are the output voltage in the $\alpha\beta 0$ frame. i_{α_o} and i_{β_o} are the output current in the $\alpha\beta 0$ frame. $u_{\alpha\alpha}$, $u_{\beta\alpha}$, ..., u_{00} are the nine arm voltages in the $\alpha\beta 0$ frame while $i_{\alpha\alpha}$, $i_{\beta\alpha}$, ..., i_{00} are the corresponding nine arm currents in the $\alpha\beta 0$ frame. Note that i_{00} is set as zero since there is no current flow between the neutral points N and O.

Using Equations (4.3) and (4.4), the input current in the $\alpha\beta 0$ frame is calculated as:

$$\begin{cases} i_{\alpha 0} = \frac{1}{\sqrt{3}}(i_{\alpha\alpha} + i_{\alpha\beta} + i_{\alpha 0}) = \frac{i_{\alpha_i}}{\sqrt{3}} \\ i_{\beta 0} = \frac{1}{\sqrt{3}}(i_{\beta\alpha} + i_{\beta\beta} + i_{\beta 0}) = \frac{i_{\beta_i}}{\sqrt{3}} \end{cases} \quad (4.5)$$

Similarly using Equations (4.3) and (4.4), the output current in $\alpha\beta 0$ frame is calculated from:

$$\begin{cases} i_{0\alpha} = \frac{1}{\sqrt{3}}(i_{A\alpha} + i_{B\alpha} + i_{C\alpha}) = \frac{i_{\alpha_o}}{\sqrt{3}} \\ i_{0\beta} = \frac{1}{\sqrt{3}}(i_{A\beta} + i_{B\beta} + i_{C\beta}) = \frac{i_{\beta_o}}{\sqrt{3}} \end{cases} \quad (4.6)$$

In Equation (4.5), $i_{\alpha 0}$ and $i_{\beta 0}$ are proportional to the $\alpha\beta$ components of the input currents i_{α_i} and i_{β_i} . $i_{0\alpha}$ and $i_{0\beta}$ are proportional to the $\alpha\beta$ components of the output currents i_{α_o} and i_{β_o} in Equation (4.6). The decomposition of Equation (4.4) then leads to the following three equations for the currents:

The input current is calculated from:

$$\sqrt{3} \begin{bmatrix} e_{\alpha_i} \\ e_{\beta_i} \end{bmatrix} = L_e \frac{d}{dt} \begin{bmatrix} i_{\alpha 0} \\ i_{\beta 0} \end{bmatrix} + \begin{bmatrix} u_{\alpha 0} \\ u_{\beta 0} \end{bmatrix} \quad (4.7)$$

where the equivalent inductance: $L_e = 3L_i + L$.

While the output current is calculated using:

$$-\sqrt{3} \begin{bmatrix} e_{\alpha_o} \\ e_{\beta_o} \end{bmatrix} = L_c \frac{d}{dt} \begin{bmatrix} i_{0\alpha} \\ i_{0\beta} \end{bmatrix} + \begin{bmatrix} u_{0\alpha} \\ u_{0\beta} \end{bmatrix} \quad (4.8)$$

And the circulating current is calculated from:

$$\begin{bmatrix} u_{\alpha\alpha} & u_{\beta\alpha} \\ u_{\alpha\beta} & u_{\beta\beta} \end{bmatrix} = -L \frac{d}{dt} \begin{bmatrix} i_{\alpha\alpha} & i_{\beta\alpha} \\ i_{\alpha\beta} & i_{\beta\beta} \end{bmatrix} \quad (4.9)$$

These three Equations (4.7), (4.8) and (4.9). show that the input, output and circulating currents have been decoupled.

4.2 Power analysis based on $\alpha\beta 0$ frame

The relationship between the arm's active power and the u_{Cxy} is given according to Equation (3.11):

$$\begin{bmatrix} u_{CAa} & u_{CBa} & u_{CCa} \\ u_{CAb} & u_{CBb} & u_{CCb} \\ u_{CAc} & u_{CBc} & u_{CCc} \end{bmatrix} = \frac{n}{CU_{Cxy}^*} \int \begin{bmatrix} p_{Aa} & p_{Ba} & p_{Ca} \\ p_{Ab} & p_{Bb} & p_{Cb} \\ p_{Ac} & p_{Bc} & p_{Cc} \end{bmatrix} dt + U_{Cxy}^* \begin{bmatrix} 1 & 1 & 1 \\ 1 & 1 & 1 \\ 1 & 1 & 1 \end{bmatrix} \quad (4.10)$$

The same 'double $\alpha\beta 0$ transformation' is then applied to Equation (4.10) to give:

$$\begin{bmatrix} u_{C\alpha\alpha} & u_{C\beta\alpha} & u_{C0\alpha} \\ u_{C\alpha\beta} & u_{C\beta\beta} & u_{C0\beta} \\ u_{C\alpha 0} & u_{C\beta 0} & u_{C00} \end{bmatrix} = \frac{n}{CU_{Cxyz}^*} \int \begin{bmatrix} p_{\alpha\alpha} & p_{\beta\alpha} & p_{0\alpha} \\ p_{\alpha\beta} & p_{\beta\beta} & p_{0\beta} \\ p_{\alpha 0} & p_{\beta 0} & p_{00} \end{bmatrix} dt + \begin{bmatrix} 0 & 0 & 0 \\ 0 & 0 & 0 \\ 0 & 0 & 3U_{Cxyz}^* \end{bmatrix} \quad (4.11)$$

where $u_{C\alpha\alpha}$, $u_{C\beta\alpha}$, ..., u_{C00} are the corresponding $\alpha\beta 0$ components of the u_{CAa} , u_{CBa} , ..., u_{CCc} .
 $p_{\alpha\alpha}$, $p_{\beta\alpha}$, ..., p_{00} are the corresponding $\alpha\beta 0$ components of the p_{Aa} , p_{Ba} , ..., p_{Cc} .

The mathematical relationship between the arm power, arm voltage and arm current are calculated by using the Mathcad software:

$$p_{\alpha\alpha} = \frac{1}{3} (e_{\alpha_i} i_{\alpha_o} - i_{\alpha_i} e_{\alpha_o}) + \frac{1}{\sqrt{6}} (e_{\alpha_i} i_{\beta\alpha} - e_{\beta_i} i_{\beta\alpha}) - \frac{1}{\sqrt{6}} (e_{\alpha_o} i_{\beta\alpha} - e_{\beta_o} i_{\beta\alpha}) \quad (4.12)$$

$$p_{\beta\alpha} = \frac{1}{3} (e_{\beta_i} i_{\alpha_o} - i_{\beta_i} e_{\alpha_o}) - \frac{1}{\sqrt{6}} (e_{\alpha_i} i_{\beta\alpha} + e_{\beta_i} i_{\alpha\alpha}) - \frac{1}{\sqrt{6}} (e_{\alpha_o} i_{\beta\alpha} - e_{\beta_o} i_{\beta\beta}) \quad (4.13)$$

$$p_{0\alpha} = \frac{1}{\sqrt{3}} (e_{\alpha_i} i_{\beta\alpha} + e_{\beta_i} i_{\alpha\alpha}) - \frac{\sqrt{2}}{\sqrt{6}} (e_{\alpha_o} i_{\alpha_o} - e_{\beta_o} i_{\beta_o}) \quad (4.14)$$

$$p_{\alpha\beta} = \frac{1}{3}(e_{\alpha_i}i_{\beta_o} - i_{\alpha_i}e_{\beta_o}) + \frac{1}{\sqrt{6}}(e_{\alpha_i}i_{\alpha\beta} + e_{\beta_i}i_{\beta\beta}) + \frac{1}{\sqrt{6}}(e_{\alpha_o}i_{\alpha\beta} + e_{\beta_o}i_{\alpha\alpha}) \quad (4.15)$$

$$p_{\beta\beta} = \frac{1}{3}(e_{\beta_i}i_{\beta_o} - i_{\beta_i}e_{\beta_o}) - \frac{1}{\sqrt{6}}(e_{\alpha_i}i_{\beta\beta} + e_{\beta_i}i_{\alpha\beta}) + \frac{1}{\sqrt{6}}(e_{\alpha_i}i_{\beta\beta} + e_{\beta_o}i_{\beta\alpha}) \quad (4.16)$$

$$p_{0\beta} = \frac{1}{\sqrt{3}}(e_{\alpha_i}i_{\alpha\beta} + e_{\beta_i}i_{\beta\beta}) + \frac{\sqrt{2}}{\sqrt{6}}(e_{\alpha_o}i_{\beta_o} + e_{\beta_o}i_{\alpha_o}) \quad (4.17)$$

$$p_{\alpha 0} = \frac{\sqrt{2}}{6}(e_{\alpha_i}i_{\alpha_i} - e_{\beta_i}i_{\beta_i}) - \frac{1}{\sqrt{3}}(e_{\alpha_o}i_{\alpha\alpha} + e_{\beta_o}i_{\alpha\beta}) \quad (4.18)$$

$$p_{\beta 0} = -\frac{\sqrt{2}}{6}(e_{\alpha_i}i_{\beta_i} + e_{\beta_i}i_{\alpha_i}) - \frac{1}{\sqrt{3}}(e_{\alpha_o}i_{\beta\alpha} + e_{\beta_o}i_{\beta\alpha}) \quad (4.19)$$

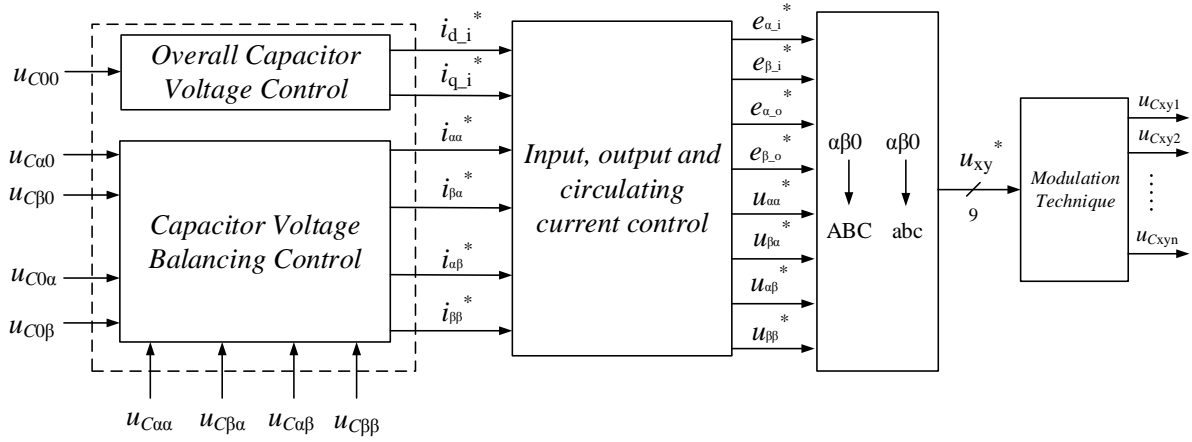
$$p_{00} = \frac{1}{3}(e_{\alpha_i}i_{\beta_i} + e_{\beta_i}i_{\beta_i} - e_{\alpha_o}i_{\alpha_o} - e_{\beta_o}i_{\beta_o}) \quad (4.20)$$

Therefore, Equations (4.12) - (4.20) show how the active power of the nine arms has been calculated in the $\alpha\beta 0$ frame.

The conclusion is that $p_{\alpha 0}$, $p_{\beta 0}$, $p_{0\alpha}$, $p_{0\beta}$ are responsible for energy balance between sub-converters; $p_{\alpha\alpha}$, $p_{\beta\alpha}$, $p_{\beta\alpha}$, $p_{\beta\beta}$ are responsible for the energy balance between arms in each sub-converter; p_{00} is responsible for the overall energy balance control of M^3C .

4.2 The ‘double $\alpha\beta 0$ transformation’ control method

The control block diagram of the ‘double $\alpha\beta 0$ transformation’ control method is shown in Figure 4.1. After the input, output and circulating current control loop, the reference value of the nine arm voltages in the $\alpha\beta 0$ frame is calculated and after applying inverse $\alpha\beta 0$ transformation twice, the reference value u_{xy}^* of the nine arms is calculated. Finally, the PWM signals are generated by the modulation technique.

Figure 4.1 The block diagram for the 'double $\alpha\beta 0$ transformation' control

4.2.1 Capacitor voltage control

The capacitor voltage control is divided into two parts: overall capacitor voltage control and the capacitor voltage balancing control. The overall capacitor voltage control is determined according to Equations (4.20) and (4.11) which calculate the reference value of the input current. The capacitor voltage balancing control is realized according to Equations (4.19) and (4.11) which calculate the reference value for the four circulating currents. The details of the control strategy are discussed in the following sub-sections.

A. Overall capacitor voltage control

As the reference DC value of $u_{C\alpha\alpha}$, $u_{C\beta\alpha}$, ..., u_{C00} should be controlled from:

$$\begin{bmatrix} U_{C\alpha\alpha} & U_{C\beta\alpha} & U_{C0\alpha} \\ U_{C\alpha\beta} & U_{C\beta\beta} & U_{C0\beta} \\ U_{C\alpha 0} & U_{C\beta 0} & U_{C00} \end{bmatrix} = \begin{bmatrix} 0 & 0 & 0 \\ 0 & 0 & 0 \\ 0 & 0 & 3U_{Cxyz}^* \end{bmatrix} \quad (4.21)$$

where $U_{C\alpha\alpha}$, $U_{C\beta\alpha}$, ..., U_{C00} are the corresponding DC value of $u_{C\alpha\alpha}$, $u_{C\beta\alpha}$, ..., u_{C00} .

The overall capacitor voltage control means controlling the $U_{C00}=3U_C^*$. Therefore, P_{00} is controlled using the P controller as:

$$p_{00}^* = 3K_1 \left(U_{Cxy}^* - \frac{U_{C00}}{3} \right) \quad (4.22)$$

where p_{00}^* is the reference value of p_{00} . K_1 is the gain of the P controller.

The input current is calculated from Equation (4.7) which is then transformed to a dq frame:

$$\sqrt{3} \begin{bmatrix} e_{d_i} \\ e_{q_i} \end{bmatrix} = \frac{1}{\sqrt{3}} \begin{bmatrix} L \frac{d}{dt} & -\omega_1 L \\ \omega_1 L & L \frac{d}{dt} \end{bmatrix} \begin{bmatrix} i_{d_i} \\ i_{q_i} \end{bmatrix} + \begin{bmatrix} e_{d_o} \\ e_{q_o} \end{bmatrix} \quad (4.23)$$

Hence, P_{00} is calculated from:

$$p_{00} = \frac{1}{3} e_{d_i} i_{d_i} - \frac{1}{3} (e_{\alpha_o} i_{\alpha_o} + e_{\beta_o} i_{\beta_o}) \quad (4.24)$$

where, the input power of M³C is defined as p_i : $p_i = e_{d_i} i_{d_i}$, and the output power of M³C is defined by: p_o : $p_o = e_{\alpha_o} i_{\alpha_o} + e_{\beta_o} i_{\beta_o}$.

Therefore, the reference value of the input current $i_{d_i}^*$ is calculated from:

$$i_{d_i}^* = \frac{p_o^*}{e_{d_i}} + K_2 \left(1 + \frac{1}{ST_2}\right) \left(U_{cxy}^* - \frac{U_{c00}}{3}\right) \quad (4.25)$$

where, p_o^* is the reference value of the output power while K_2 is the proportional gain and T_2 is the sampling time.

Then $i_{q_i}^*$ is equal to zero for the unity power factor.

$$i_{q_i}^* = 0 \quad (4.26)$$

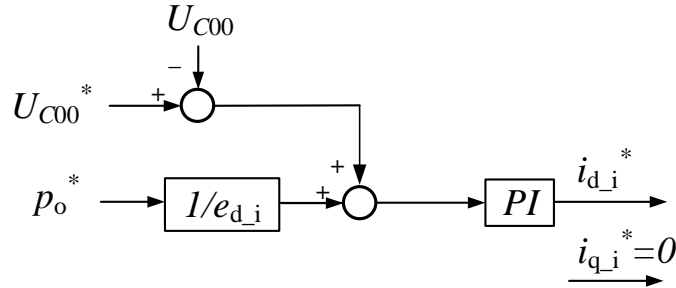


Figure 4.2 The overall capacitor voltage control block diagram

B. Capacitor voltage balancing control

● Capacitor voltage balancing control between arms

According to Equations (4.12) and (4.13), the mathematical relationship between $p_{\alpha\alpha}$ and $i_{\alpha\alpha}$, $i_{\beta\alpha}$; $p_{\beta\alpha}$ and $i_{\alpha\alpha}$, $i_{\beta\alpha}$ are determined by:

$$\begin{cases} p_{\alpha\alpha} \propto (e_{\alpha_i} i_{\alpha\alpha} - e_{\beta_i} i_{\beta\alpha}) \propto (\sin \theta_i \cdot i_{\alpha\alpha} + \cos \theta_i \cdot i_{\beta\alpha}) \\ p_{\beta\alpha} \propto (-e_{\alpha_i} i_{\beta\alpha} - e_{\beta_i} i_{\alpha\alpha}) \propto (-\sin \theta_i \cdot i_{\beta\alpha} + \cos \theta_i \cdot i_{\alpha\alpha}) \end{cases} \quad (4.27)$$

Equation (4.27) can then be further developed as:

$$\begin{bmatrix} p_{\alpha\alpha} & p_{\beta\alpha} \end{bmatrix} \propto \begin{bmatrix} i_{\alpha\alpha} & i_{\beta\alpha} \end{bmatrix} \begin{bmatrix} \sin \theta_i & \cos \theta_i \\ \cos \theta_i & -\sin \theta_i \end{bmatrix} \quad (4.28)$$

Therefore, the mathematical relationship between $p_{\alpha\alpha}$, $p_{\beta\alpha}$ and $i_{\alpha\alpha}$, $i_{\beta\alpha}$ can be written as:

$$\begin{bmatrix} i_{\alpha\alpha} & i_{\beta\alpha} \end{bmatrix} = \begin{bmatrix} p_{\alpha\alpha} & p_{\beta\alpha} \end{bmatrix} \begin{bmatrix} \sin \theta_i & \cos \theta_i \\ \cos \theta_i & -\sin \theta_i \end{bmatrix} \quad (4.29)$$

Following a similar approach, the mathematical relationship between $p_{\alpha\beta}$, $p_{\beta\beta}$ and $i_{\alpha\alpha}$, $i_{\beta\alpha}$ is defined by:

$$\begin{bmatrix} i_{\alpha\beta} & i_{\beta\beta} \end{bmatrix} = \begin{bmatrix} p_{\alpha\beta} & p_{\beta\beta} \end{bmatrix} \begin{bmatrix} \sin \theta_i & \cos \theta_i \\ \cos \theta_i & -\sin \theta_i \end{bmatrix} \quad (4.30)$$

Combining Equation (4.29) and Equation (4.30) gives:

$$\begin{bmatrix} i_{\alpha\alpha} & i_{\beta\alpha} \\ i_{\alpha\beta} & i_{\beta\beta} \end{bmatrix} = \begin{bmatrix} p_{\alpha\alpha} & p_{\beta\alpha} \\ p_{\alpha\beta} & p_{\beta\beta} \end{bmatrix} \begin{bmatrix} \sin \theta_i & \cos \theta_i \\ \cos \theta_i & -\sin \theta_i \end{bmatrix} \quad (4.31)$$

● *Capacitor voltage balancing control between sub-converters*

Applying the same theory to developing the mathematical relationship between $p_{0\alpha}$, $p_{0\beta}$ and $i_{\alpha\alpha}$, $i_{\beta\alpha}$ leads to:

$$\begin{cases} p_{0\alpha} \propto (e_{\alpha i} i_{\alpha\alpha} - e_{\alpha i} i_{\beta\alpha}) \propto (\sin \theta_i \cdot i_{\alpha\alpha} - \cos \theta_i \cdot i_{\beta\alpha}) \\ p_{0\beta} \propto (e_{\alpha i} i_{\alpha\beta} + e_{\alpha i} i_{\beta\beta}) \propto (\sin \theta_i \cdot i_{\alpha\beta} - \cos \theta_i \cdot i_{\beta\beta}) \end{cases} \quad (4.32)$$

These two relationships can be written as:

$$\begin{cases} p_{0\alpha} \propto \begin{bmatrix} i_{\alpha\alpha} & i_{\beta\alpha} \end{bmatrix} \begin{bmatrix} \sin \theta_i \\ -\cos \theta_i \end{bmatrix} \\ p_{0\beta} \propto \begin{bmatrix} i_{\alpha\beta} & i_{\beta\beta} \end{bmatrix} \begin{bmatrix} \sin \theta_i \\ -\cos \theta_i \end{bmatrix} \end{cases} \quad (4.33)$$

Post-multiplying both side of Equation (4.33) by $[\sin \theta_i \ -\cos \theta_i]$ gives:

$$\begin{cases} p_{0\alpha} [\sin \theta_i \ -\cos \theta_i] = \begin{bmatrix} i_{\alpha\alpha} & i_{\beta\alpha} \end{bmatrix} \begin{bmatrix} \sin^2 \theta_i & -\sin \theta_i \cos \theta_i \\ -\sin \theta_i \cos \theta_i & \cos^2 \theta_i \end{bmatrix} \\ p_{0\beta} [\sin \theta_i \ -\cos \theta_i] \propto \begin{bmatrix} i_{\alpha\beta} & i_{\beta\beta} \end{bmatrix} \begin{bmatrix} \sin^2 \theta_i & -\sin \theta_i \cos \theta_i \\ -\sin \theta_i \cos \theta_i & \cos^2 \theta_i \end{bmatrix} \end{cases} \quad (4.34)$$

Hence, the mathematical relationship between $P_{0\alpha}$, $P_{0\beta}$ and $i_{\alpha\alpha}$, $i_{\beta\alpha}$ is given by:

$$\begin{bmatrix} i_{\alpha\alpha} & i_{\beta\alpha} \\ i_{\alpha\beta} & i_{\beta\beta} \end{bmatrix} = \begin{bmatrix} P_{0\alpha} \\ P_{0\beta} \end{bmatrix} \begin{bmatrix} \sin \theta_i & -\cos \theta_i \end{bmatrix} \quad (4.35)$$

Similarly, the mathematical relationship between $P_{\alpha 0}$, $P_{\beta 0}$ and $i_{\alpha\alpha}$, $i_{\beta\alpha}$ is defined by:

$$\begin{bmatrix} i_{\alpha\alpha} & i_{\beta\alpha} \\ i_{\alpha\beta} & i_{\beta\beta} \end{bmatrix} = \begin{bmatrix} -p_{\alpha 0} \sin \theta_o & -p_{\beta 0} \sin \theta_o \\ p_{\alpha 0} \cos \theta_o & p_{\beta 0} \cos \theta_o \end{bmatrix} \quad (4.36)$$

In this way the mathematical relationship between the circulating current and eight arm power has been determined. The reference values of the four circulating currents: $i_{\alpha\alpha}^*$, $i_{\beta\alpha}^*$, $i_{\alpha\beta}^*$, $i_{\beta\beta}^*$ are then adjusted using P controller according to:

$$\begin{cases} i_{\alpha\alpha}^* = K_3(p_{\alpha\alpha}^* \sin \theta_i + p_{\beta\alpha}^* \cos \theta_i) + K_4(p_{0\alpha}^* \sin \theta_i) - K_5(p_{\alpha 0}^* \sin \theta_o) \\ i_{\beta\alpha}^* = K_3(p_{\alpha\alpha}^* \cos \theta_i - p_{\beta\alpha}^* \sin \theta_i) - K_4(p_{0\alpha}^* \cos \theta_i) - K_5(p_{\beta 0}^* \sin \theta_o) \\ i_{\alpha\beta}^* = K_3(p_{\alpha\beta}^* \sin \theta_i + p_{\beta\beta}^* \cos \theta_i) + K_4(p_{0\beta}^* \sin \theta_i) + K_5(p_{\alpha 0}^* \cos \theta_o) \\ i_{\beta\beta}^* = K_3(p_{\alpha\beta}^* \cos \theta_i - p_{\beta\beta}^* \sin \theta_i) - K_4(p_{0\beta}^* \cos \theta_i) + K_5(p_{\beta 0}^* \cos \theta_o) \end{cases} \quad (4.37)$$

where, K_3 , K_4 and K_5 are the proportional gains.

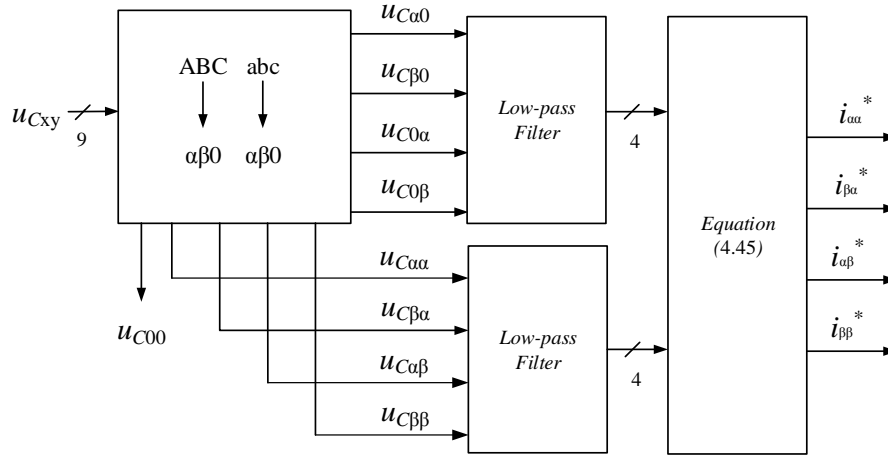


Figure 4.3 The capacitor voltage balancing control block diagram

4.2.2 Input, output and circulating current control

The double $\alpha\beta 0$ transformation has been applied to the nine arm currents, i_{xy} , and these are then used to calculate the eight $\alpha\beta$ components of the arm current as discussed in Equation (4.4). Therefore the input, output and circulating currents have been fully decoupled and using the reference values of these three currents, the eight voltage components in the $\alpha\beta 0$ frame are then calculated. Finally, the modulation technique generates the PWM singles. The details of the input, output and circulating current control are discussed in the following sub-sections.

A. Input current control

The input currents in the $\alpha\beta 0$ frame $i_{\alpha_i}^*$ and $i_{\beta_i}^*$ are calculated according to Equation (4.5). These currents are then transformed to the dq frame to give: i_{d_i} and i_{q_i} according to Equation (4.38).

$$T_{\alpha\beta/dq} = \begin{bmatrix} \sin \omega_1 t & -\cos \omega_1 t \\ \cos \omega_1 t & \sin \omega_1 t \end{bmatrix} \quad (4.38)$$

The reference value of the input currents: $i_{d_i}^*$ and $i_{q_i}^*$ have been calculated using Equations (4.25) and (4.26). According to Equation (4.23), the input current control is realized by using the PI controller as calculated in Equation (4.39):

$$\begin{bmatrix} e_{d_i}^* \\ e_{q_i}^* \end{bmatrix} = \sqrt{3} \begin{bmatrix} e_{d_i} \\ e_{q_i} \end{bmatrix} - \frac{\omega_1 L}{\sqrt{3}} \begin{bmatrix} 0 & -1 \\ 1 & 0 \end{bmatrix} \begin{bmatrix} i_{d_i} \\ i_{q_i} \end{bmatrix} - K_6 \left(1 + \frac{1}{ST_6} \right) \left(\begin{bmatrix} i_{d_i}^* \\ i_{q_i}^* \end{bmatrix} - \begin{bmatrix} i_{d_i} \\ i_{q_i} \end{bmatrix} \right) \quad (4.39)$$

where K_6 is the proportional gain. T_6 is the sampling time.

The input current control calculates $e_{d_i}^*$ and $e_{q_i}^*$ which are the reference values of the input voltages in the dq frame. Then, $e_{d_i}^*$ and $e_{q_i}^*$ are then transformed to the $\alpha\beta 0$ frame $e_{\alpha_i}^*$ and $e_{\beta_i}^*$ as illustrated in Figure 4.4.

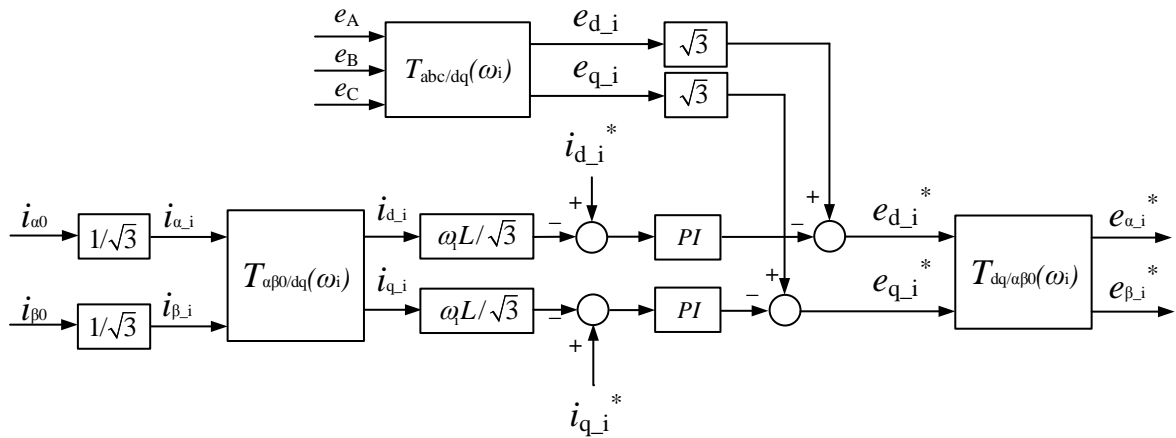


Figure 4.4 The block diagram of the input current control

B. Output current control

The output is connected with the grid which means the control theory is very similar to the input current control. Therefore, the output current control is only briefly described here. The output currents in the $\alpha\beta 0$ frame $i_{\alpha_o}^*$ and $i_{\beta_o}^*$ are calculated according to Equation (4.6). They are

then transformed to the dq frame giving: i_{d_o} and i_{q_o} . Next the reference values of the output currents: $i_{d_o}^*$ and $i_{q_o}^*$ can be calculated and then using Equation (4.8), the reference value of the output voltage in the dq frame: $e_{d_o}^*$ and $e_{q_o}^*$ are determined. Finally $e_{d_i}^*$ and $e_{q_i}^*$ are transformed to the $\alpha\beta 0$ frame $e_{\alpha_o}^*$ and $e_{\beta_o}^*$ as illustrated in Figure 4.5.

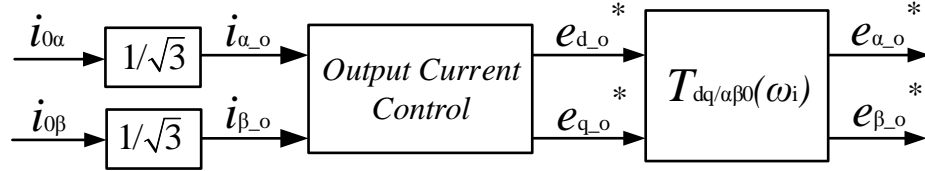


Figure 4.5 The block diagram of the output current control

C. Circulating current control

The calculation for the circulating current is specified in Equation (4.5). The reference value of the circulating current is then calculated by using the P controller as given in Equation (4.40):

$$\begin{bmatrix} u_{\alpha\alpha}^* & u_{\beta\alpha}^* \\ u_{\alpha\beta}^* & u_{\beta\beta}^* \end{bmatrix} = -K_6 \left(\begin{bmatrix} i_{\alpha\alpha}^* & i_{\beta\alpha}^* \\ i_{\alpha\beta}^* & i_{\beta\beta}^* \end{bmatrix} - \begin{bmatrix} i_{\alpha\alpha} & i_{\beta\alpha} \\ i_{\alpha\beta} & i_{\beta\beta} \end{bmatrix} \right) \quad (4.40)$$

The reference value of four circulating currents: $i_{\alpha\alpha}^*$, $i_{\beta\alpha}^*$, $i_{\alpha\beta}^*$, $i_{\beta\beta}^*$ are determined from Equation (4.37). As shown in Figure 4.6, the four corresponding reference values of the voltage components: $u_{\alpha\alpha}^*$, $u_{\beta\alpha}^*$, $u_{\alpha\beta}^*$, $u_{\beta\beta}^*$ in terms of $i_{\alpha\alpha}^*$, $i_{\beta\alpha}^*$, $i_{\alpha\beta}^*$, $i_{\beta\beta}^*$ are subsequently calculated using Equation (4.40). The eight reference values of the voltage components in the $\alpha\beta 0$ frame: $e_{\alpha_i}^*$, $e_{\beta_i}^*$; $e_{\alpha_o}^*$, $e_{\beta_o}^*$; $u_{\alpha\alpha}^*$, $u_{\beta\alpha}^*$, $u_{\alpha\beta}^*$, $u_{\beta\beta}^*$ are then calculated and transformed to the abc frame as shown in Figure 4.1. Then, the reference values of the nine arm voltages: u_{xy}^* are calculated and by using the modulation technique, PWM signals are generated and send to each SM. The modulation technique is not discussed in this thesis for the ‘double $\alpha\beta 0$ transformation method’.

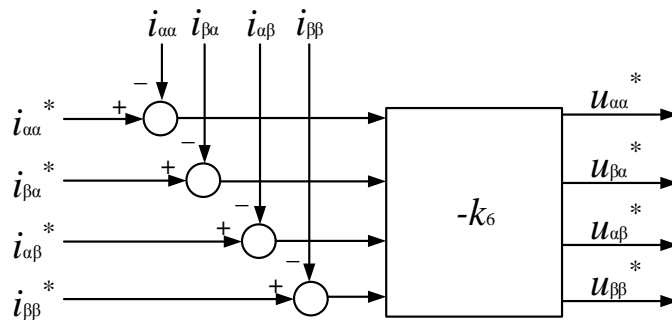


Figure 4.6 The block diagram of the circulating current control

4.3 Illustrative simulation results under output voltage step change operation

The simulation model of M^3C using the ‘double $\alpha\beta 0$ transformation method’ is developed using the MATLAB/SIMULINK software. The input side of M^3C is connected to the offshore wind farm (16.7 Hz) while the output side is connected with the Grid (50 Hz). The simulation parameters is shown in Table 4.1.

Table 4.1 Simulation parameters of the proposed control method

Description	Parameters	Value
Rated active power	P	20 kW
Input RMS line voltage	E_i	380 V
Input frequency	f_i	16.7 Hz
Output RMS line voltage	E_o	380 V
Output frequency	f_o	50 Hz
Arm inductance	L	4 mH
Switching frequency	f_s	4 kHz
Grid-connected filter inductance	L_g	1 mH
Grid-connected filter capacitance	C_g	10 μ F
Capacitance of SM’s capacitor	C_{xyz}	1 mF
Rated dc capacitor voltage	$U_{C_{xyz}}^*$	250 V
Number of SMs per arm	n	3

4.3.1 Case I: Steady state operation

Figure 4.7 shows the simulation results of M^3C under the steady state operation. The input voltage and input current is in phase which shows the unity power operation. The arm current as shown in Figure 4.7(c) contains two frequency components: 50 Hz and 16.7 Hz. The three capacitor voltages of arm_{Aa} are illustrated in Figure 4.7(e) which equalled with each other and controlled around 250 V with $\pm 8\%$ voltage ripple. The sum of all capacitor voltages in arm_{Aa} , arm_{Ba} and arm_{Ca} in sub-converter a is illustrated in Figure 4.7(f) which proves that the energy

difference between these three arms is well balanced.

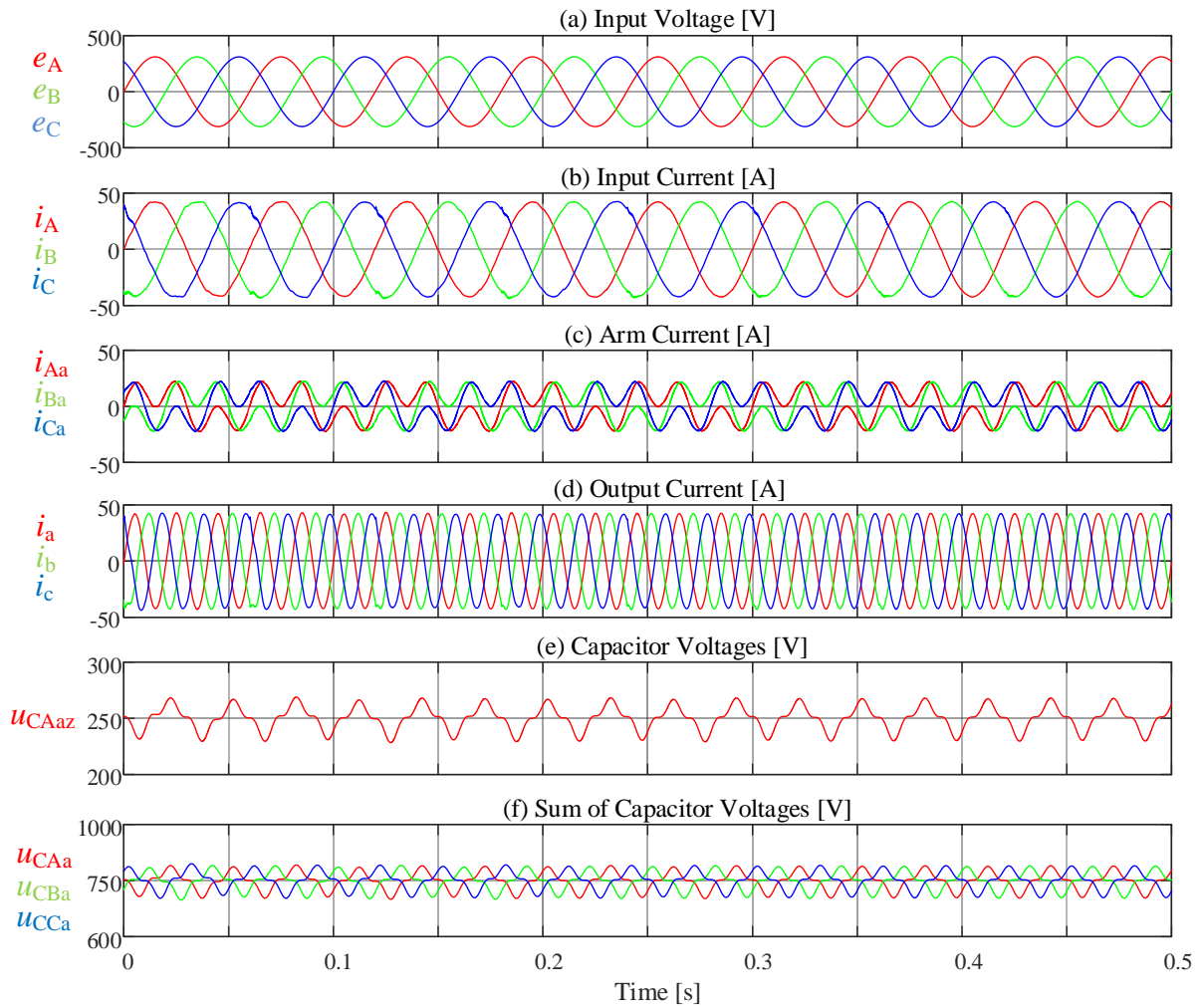


Figure 4.7 Simulation results under the steady-state operation

4.3.2 Case II: Dynamic output power operation

In order to verify the control effect of the ‘double $\alpha\beta 0$ transformation’ control method, M^3C is tested under dynamic output power (from 20 kW to 24 kW) operation. As shown in Figure 4.8, the three capacitor voltages of arm_{Aa} are illustrated in Figure 4.8(d) drops at first and then are all tightly balanced around 750 V with $\pm 6.7\%$ voltage ripple. This is because the output power rises instantaneously and the energy within the capacitors are absorbed. However, the capacitors need to be re-supplied by the energy balancing control so the input current will increase immediately. When the input power and output power are equalled with each other, the system has reached a new steady-state operation point. It can be seen that the transition is smooth, the overshoot is small, and the dynamic performance is good.

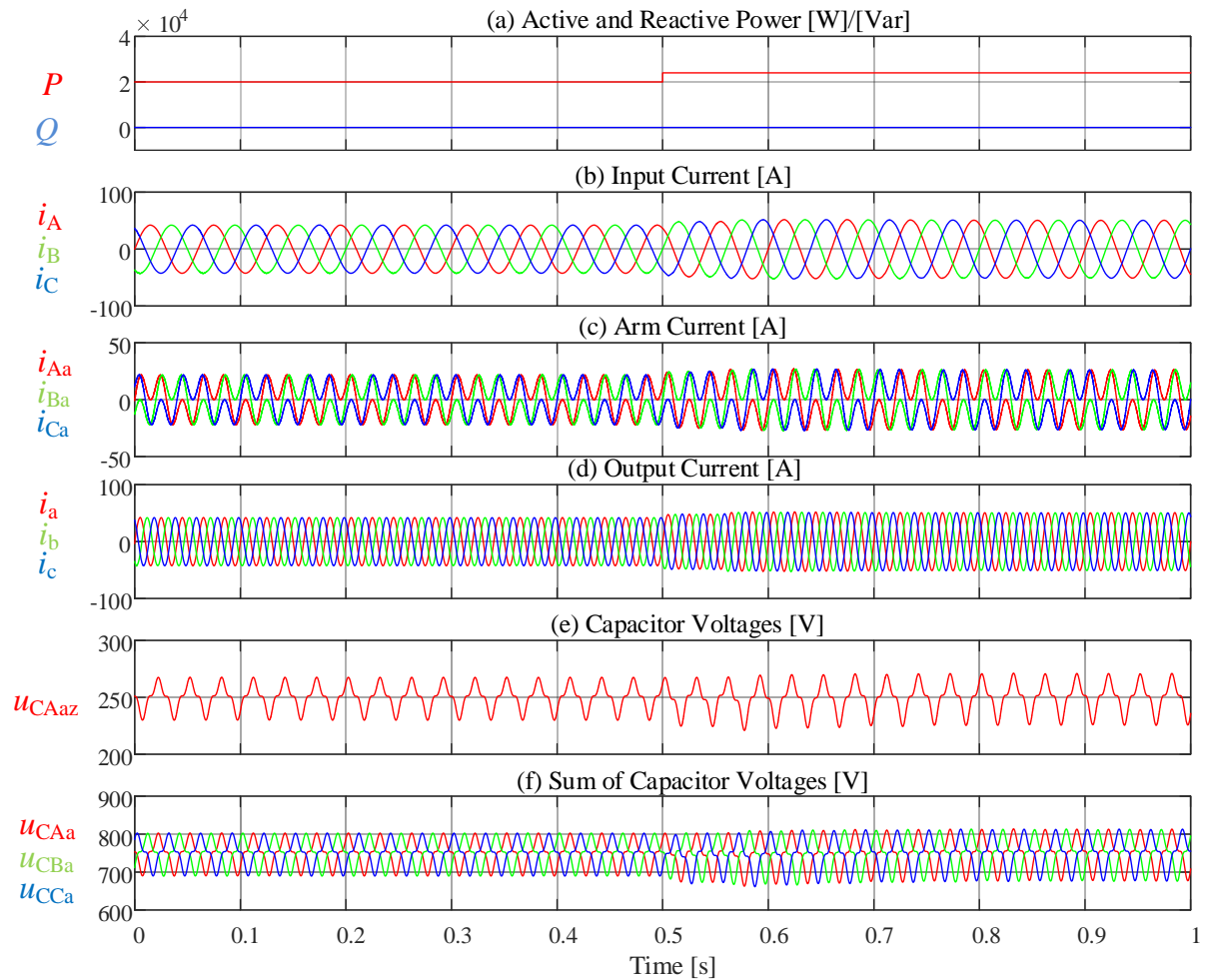


Figure 4.8 Simulation results under a dynamic output power operation

4.4 Summary

The most commonly used control method of M^3C is studied and presented in this chapter. The analysis and control algorithm needs multiple $\alpha\beta 0$ transformations. It decoupled the input, output and circulating current and calculate the mathematical relationship between the arm power and capacitor voltage on the $\alpha\beta 0$ frame. Determined by the mathematical relationship, four circulating current components with either input or output frequency are designed to balance the capacitor voltage. However, the control logic of using the circulating current components on the $\alpha\beta 0$ frame to balance the capacitor voltage is too complex and not clear. Therefore, it is essential to design a simplified control method for M^3C which is discussed in following chapters.

Chapter 5 Hierarchical Energy Balance Control Method for M³C based on Injecting Output Frequency Circulating Currents

The target of this thesis is to develop a simplified control method of M³C for the LFAC transmission system. Two different control methods have been developed in this thesis and they are presented in chapter 5 and chapter 6 respectively. In this chapter, the simplified energy balance control method of M³C with injecting single frequency is discussed in details.

5.1 The mathematical model of sub-converter a

As illustrated in Figure 5.1, M³C is divided into three identical sub-converters. For simplicity and owing to the symmetry properties, only sub-converter a is considered for deriving the mathematical model in this section. However, this can be equally applied to the other sub-converters of M³C.

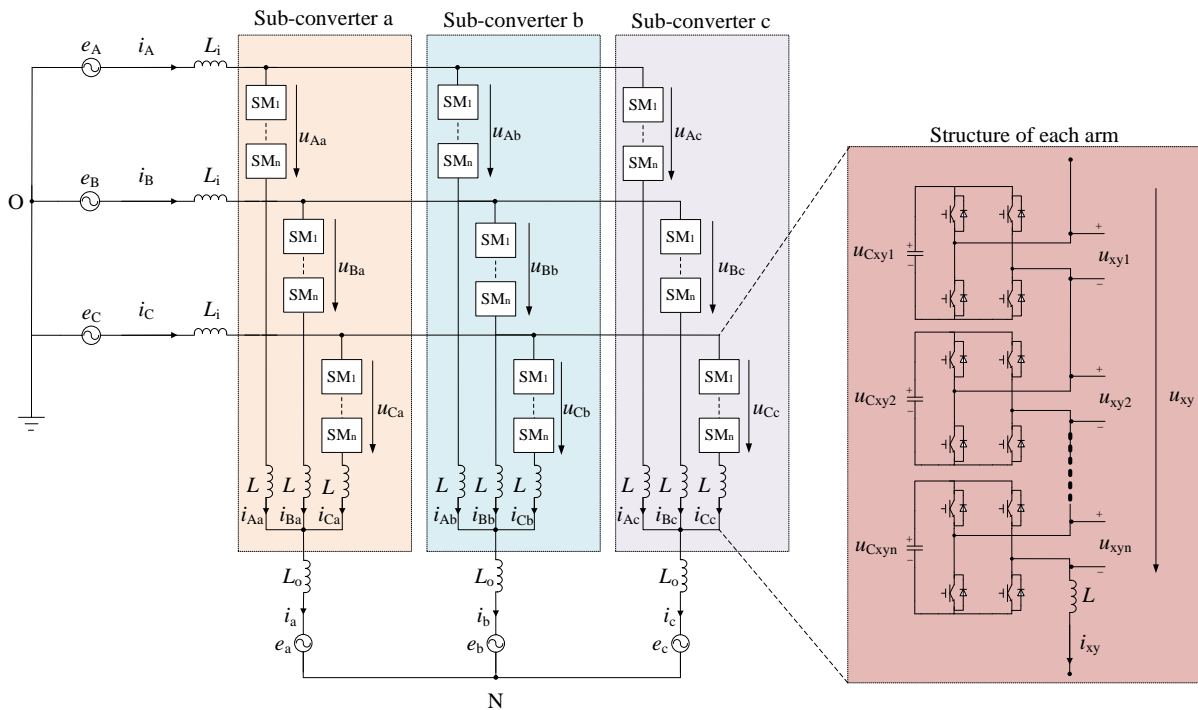


Figure 5.1 The circuit diagram of Modular Multilevel Matrix Converter

As injecting the output frequency circulating current, each arm current contains three current components: input current component, output current component and circulating current component. For better presentation and discussion in the following sections, the input is

represented by abbreviated letter: i and the output is represented by abbreviated letter: o, while the circulating current is represented by: cir. Therefore, the arm current in sub-converter a is given by (1) as follows:

$$\begin{cases} i_{Aa} = i_{Aa_i} + i_{Aa_o} + i_{Aa_cir} \\ i_{Ba} = i_{Ba_i} + i_{Ba_o} + i_{Ca_cir} \\ i_{Ca} = i_{Ca_i} + i_{Ca_o} + i_{Ca_cir} \end{cases} \quad (5.1)$$

where, i_{Aa_i} , i_{Ba_i} and i_{Ca_i} are the input current components and i_{Aa_o} , i_{Ba_o} and i_{Ca_o} are the output current components while i_{Aa_cir} , i_{Ba_cir} and i_{Ca_cir} are circulating currents.

It is worth noting that the circulating current flows within the sub-converter and does not contribute to the input and output currents and the sum of the three circulating currents equals to zero.

$$i_{Aa_cir} + i_{Ba_cir} + i_{Ca_cir} = 0 \quad (5.2)$$

Due to the symmetry property of the proposed M³C, the input current components and the output current components are one third of the input and output currents, respectively. Therefore, (5.1) can be further represented by (5.4) as follows:

$$\begin{cases} i_{Aa} = \frac{i_A}{3} + \frac{i_a}{3} + i_{Aa_cir} \\ i_{Ba} = \frac{i_B}{3} + \frac{i_a}{3} + i_{Ba_cir} \\ i_{Ca} = \frac{i_C}{3} + \frac{i_a}{3} + i_{Ca_cir} \end{cases} \quad (5.3)$$

Hence, the arm voltage of sub-converter a can be calculated as:

$$\begin{cases} u_{Aa} = e_A - (3L_1 + L) \frac{di_{Aa_i}}{dt} - (3L_o + L) \frac{di_{Aa_o}}{dt} - L \frac{di_{Aa_cir}}{dt} - e_a \\ u_{Ba} = e_B - (3L_1 + L) \frac{di_{Ba_i}}{dt} - (3L_o + L) \frac{di_{Aa_o}}{dt} - L \frac{di_{Ba_cir}}{dt} - e_a \\ u_{Ca} = e_C - (3L_1 + L) \frac{di_{Ca_i}}{dt} - (3L_o + L) \frac{di_{Aa_o}}{dt} - L \frac{di_{Ca_cir}}{dt} - e_a \end{cases} \quad (5.4)$$

5.2 The proposed control strategy

This section utilizes the developed mathematical model as presented in the last section and discusses in detail the proposed control method for M³C. The control block diagram of the proposed control method is illustrated in Figure 5.2, where it is divided into three control levels as discussed in following sub-sections. It is worth noting that again sub-converter a is considered here for the analysis while similar analysis can be applied for the other two sub-converters.

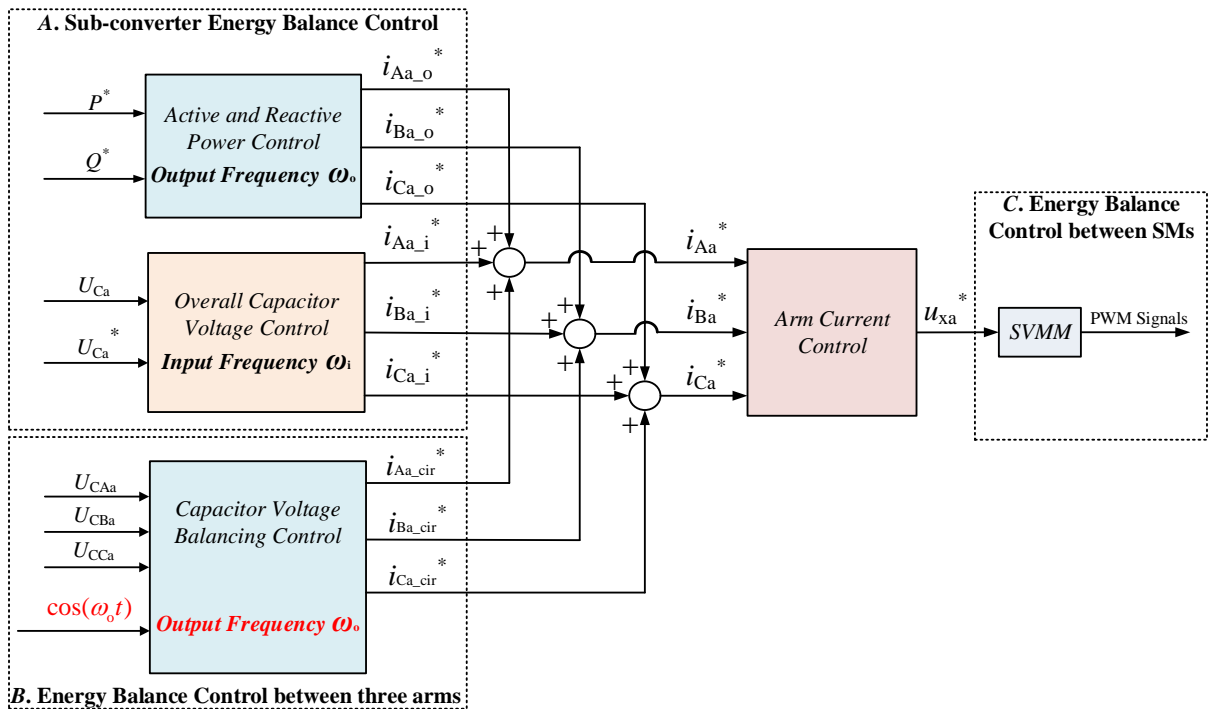


Figure 5.2 The block diagram of the proposed control method in sub-converter a

5.2.1 Sub-converter Energy Balance Control

The energy balance control of M³C requires that the sum of all capacitor voltages within a sub-converter, which is defined as u_{Cy} , to be maintained constant.

Taking sub-converter a as an example, the sum of all capacitor voltages is u_{Ca} . Furthermore, as the sum of capacitor voltages of n SMs of each of the three arms in each sub-converter is defined as u_{Cxy} ($x \in \{A, B, C\}$, $y \in \{a, b, c\}$). Hence, the sum of all capacitor voltages in arm_{Aa} , arm_{Ba} and arm_{Ca} are u_{CAa} , u_{CBa} and u_{CCa} , respectively:

$$u_{Ca} = u_{CAa} + u_{CBa} + u_{CCa} \quad (5.5)$$

where, u_{CAa} , u_{CBa} and u_{CCa} are calculated by (5.6):

$$\begin{cases} u_{CAa} = u_{CAa1} + u_{CAa2} + \dots + u_{CAan} \\ u_{CBa} = u_{CBa1} + u_{CBa2} + \dots + u_{CBan} \\ u_{CCa} = u_{CCa1} + u_{CCa2} + \dots + u_{CCan} \end{cases} \quad (5.6)$$

The arm current consists of input and output current components as given by (5.3), where any changes in these currents will influence the u_{Ca} and vice versa. Hence controlling u_{Ca} is the key to achieve the required energy balance.

a. Active and Reactive Power Control

In Figure 5.3, P^* and Q^* are reference values of the required active and reactive power, respectively, which are dependent on the demand from the output side.

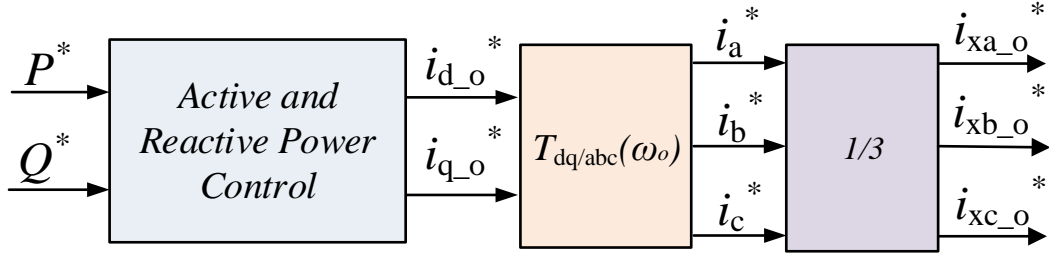


Figure 5.3 Active and reactive power control block diagram

The output voltages are transferred to dq frame (i.e. e_d and e_q) using (5.7):

$$T_{abc/dq} = \sqrt{\frac{2}{3}} \begin{bmatrix} \cos \theta & \cos\left(\theta - \frac{2}{3}\pi\right) & \cos\left(\theta + \frac{2}{3}\pi\right) \\ -\sin \theta & -\sin\left(\theta - \frac{2}{3}\pi\right) & -\sin\left(\theta + \frac{2}{3}\pi\right) \end{bmatrix} \quad (5.7)$$

Then the reference values, $i_{d_o}^*$ and $i_{q_o}^*$ of the output currents, can be obtained from (5.8):

$$\begin{cases} P^* = e_d \cdot i_{d_o}^* \\ Q^* = -i_{q_o}^* \cdot e_d \end{cases} \quad (5.8)$$

Therefore, the reference values of the output currents i_a^* , i_b^* and i_c^* can then be calculated by transforming $i_{d_o}^*$ and $i_{q_o}^*$ back to abc frame using (5.9).

$$T_{dq/abc} = \sqrt{\frac{2}{3}} \begin{bmatrix} \cos \theta & \sin \theta \\ \cos(\theta - \frac{2}{3}\pi) & -\sin(\theta - \frac{2}{3}\pi) \\ \cos(\theta + \frac{2}{3}\pi) & -\sin(\theta + \frac{2}{3}\pi) \end{bmatrix} \quad (5.9)$$

With reference to (5.3), in each sub-converter the output current components within the arm current is equal to one third of the output current. Therefore, the reference value of output current components $i_{xa_o}^*$, $i_{xb_o}^*$ and $i_{xc_o}^*$ of the nine arms currents of three sub-converters in M³C have been calculated as shown in Figure 5.3.

where:

$$i_{xy_o}^* = \frac{i_y^*}{3} \quad (5.10)$$

b. Overall capacitor voltage control

In Figure 5.4, the low pass filter functions as filtering out the ac fluctuation of u_{Ca} . After passing through the filter, the DC capacitor voltage of u_{Ca} is defined as U_{Ca} . U_{Ca}^* is the reference value of U_{Ca} . When U_{Ca} is bigger than U_{Ca}^* it means there is an extra energy that is stored within the sub-converter a. Conversely, when U_{Ca} is smaller than U_{Ca}^* , it means the energy provided to the sub-converter a is insufficient. Therefore, the input side must increase the energy provided to sub-converter a. The ultimate goal of this control block is to keep U_{Ca} equal to U_{Ca}^* which means the input side meets the required energy demand.

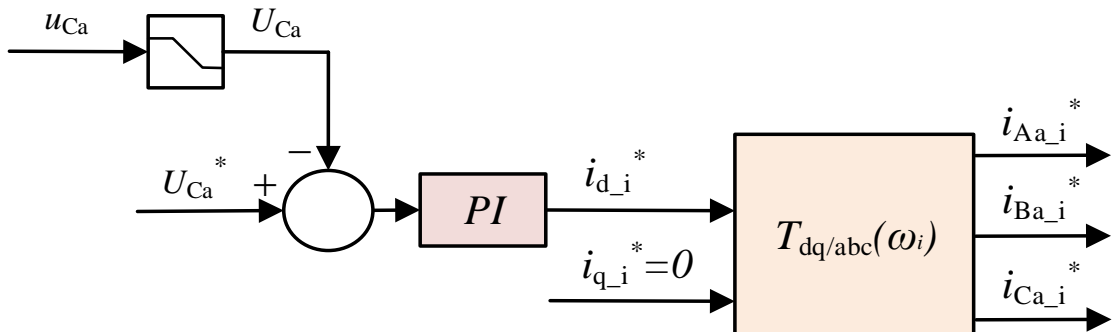


Figure 5.4 The block diagram of the overall capacitor voltage control

In Figure 5.4, $i_{d_i}^*$ and $i_{q_i}^*$ are reference values of the direct and quadrature axis components of the input current components i_{Aa_i} , i_{Ba_i} and i_{Ca_i} , respectively. Furthermore, $i_{q_i}^*$ is set to zero

to achieve a unity power factor. Therefore, the reference values of the input current components: $i_{Aa_i}^*$, $i_{Ba_i}^*$ and $i_{Ca_i}^*$ in Figure 5.4 have been calculated according to transformation matrix (5.9).

It is important to mention that the amplitude of three arm currents i_{Aa_i} , i_{Ab_i} , i_{Ac_i} in sub-converters a, b, c, respectively are not necessary equalled with each other. When there is an unbalanced condition at the grid, the proposed control method is able to self-balance the energy between sub-converters.

5.2.2 Energy Balance Control between the three arms of the sub-converter (Capacitor voltage balancing control)

Although the overall energy of the sub-converter is controlled, however it is not necessarily means that the energy between the three arms of the sub-converter is balanced. Therefore, another control level is required, which utilizes the circulating current. With the circulating current control, the arm with bigger energy compensates the arm with smaller energy, to realize the dynamic energy balance within each sub-converter.

Figure 5.5 illustrates the proposed circulating current control, which equally balances the energy across the three arms of the sub-converter. The sum of all capacitor voltages in arm_{Aa} , arm_{Ba} and arm_{Ca} are u_{CAa} , u_{CBa} and u_{CCa} , respectively. The low pass filter functions as filtering out the ac fluctuation of u_{CAa} , u_{CBa} and u_{CCa} . After passing through the filter, these three DC capacitor voltages are defined as U_{CAa} , U_{CBa} and U_{CCa} . Then, these three values are averaged as in (5.11):

$$\overline{U_{Ca}} = (U_{CAa} + U_{CBa} + U_{CCa}) / 3 \quad (5.11)$$

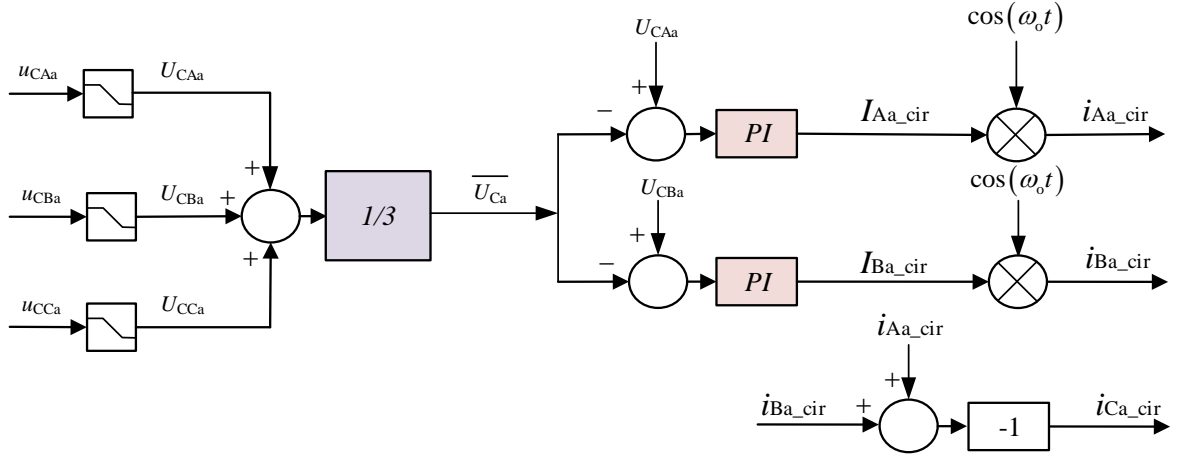


Figure 5.5 The block diagram of the capacitor voltage balancing control in sub-converter a

After U_{CAa} and U_{CBa} are compared with the mean value and the error is processed the PI controller, the RMS value of the circulating currents: $I_{Aa_cir}^*$, $I_{Ba_cir}^*$ are then calculated as portrayed in Figure 5.5.

In order to realize the independent control of each sub-converter, the phase angle: $\omega_0 t$ of output voltage e_a is set as the reference phase angle for these three circulating currents since these three arms of sub-converter is connected with output phase a. Therefore, the calculation of the circulating currents is shown in (5.12):

$$\begin{cases} i_{Aa_cir}^* = I_{Aa_cir}^* \cos(\omega_0 t) \\ i_{Ba_cir}^* = I_{Ba_cir}^* \cos(\omega_0 t) \\ i_{Ca_cir}^* = -i_{Aa_cir}^* - i_{Ba_cir}^* \end{cases} \quad (5.12)$$

The energy difference between three arms of sub-converter a is caused by the active power that are generated by circulating currents, these three active power's value are defined by: P_{Aa_cir} , P_{Ba_cir} and P_{Ca_cir} which can be calculated as follows:

$$\begin{cases} P_{Aa_cir} = \frac{I_{Aa_cir}^* \cdot E_a}{2} \\ P_{Ba_cir} = \frac{I_{Ba_cir}^* \cdot E_a}{2} \\ P_{Ca_cir} = \frac{I_{Ca_cir}^* \cdot E_a}{2} \end{cases} \quad (5.13)$$

Figure 5.6 shows one possible power exchange path between the three arms in sub-converter a, which is further discussed in details in the remaining of this section.

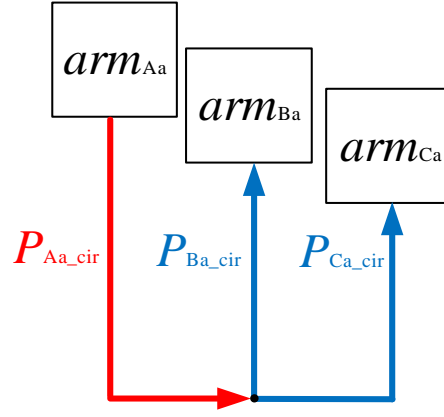


Figure 5.6 One possible power exchange path

When:

$$\begin{cases} U_{CAa} - \overline{U_{Ca}} > 0 \\ U_{CBa} - \overline{U_{Ca}} < 0 \\ U_{CCa} - \overline{U_{Ca}} < 0 \end{cases} \quad (5.14)$$

After PI controller, the direction of the three circulating currents are determined as given:

$$\begin{cases} I_{Aa_cir}^* > 0 \\ I_{Ba_cir}^* < 0 \\ I_{Ca_cir}^* < 0 \end{cases} \quad (5.15)$$

According to (5.13), therefore:

$$\begin{cases} P_{Aa_cir} > 0 \\ P_{Ba_cir} < 0 \\ P_{Ca_cir} < 0 \end{cases} \quad (5.16)$$

For this condition, the arm_{Aa} should supply P_{Aa_cir} to the output phase a while arm_{Ba} and arm_{Ca} should absorb P_{Ba_cir} and P_{Ca_cir} from the output phase a. Meanwhile, since the sum of the circulating currents is equal to zero as given by (5.2), therefore:

$$P_{Aa_cir} + P_{Ba_cir} + P_{Ca_cir} = 0 \quad (5.17)$$

Therefore, P_{Aa_cir} , P_{Ba_cir} and P_{Ca_cir} only exchange between the three arms to compensate with each other in sub-converter a.

5.2.3 The arm current Control

Figure 5.7 shows the arm current control according to (5.3) in sub-converter a. The reference value of the arm current i_{xa}^* consists of three current components: $i_{xa_i}^*$, $i_{xa_o}^*$ and i_{xa_cir} that have been calculated in the previous sections.

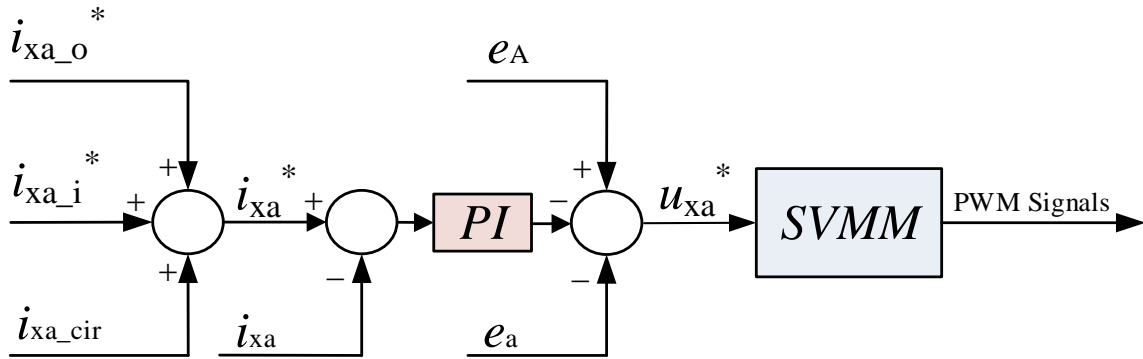


Figure 5.7 Arm current control block diagram

The difference between the i_{xa} and i_{xa}^* are calculated at first, after which the PI controller along with a feedforward term as per (5.4) is used to calculate the reference value of three arm voltages (noted by u_{xa}^*). Then, the selective voltage mapping modulation technique (SVMM), as discussed in the following section, is designed to generate the PWM signals of each SM.

5.2.4 Energy balance control between n SMs of each arm (Selective Voltage Mapping Modulation)

In each arm, each SM's energy should be balanced which indicates the balance of the capacitor voltage. Therefore, a third control level is required to control the SM's capacitors voltage. The selective voltage mapping modulation (SVMM) is designed based on the phase disposition modulation method (PDPWM) but the sorting algorithm is specifically designed for M³C. The voltages of all SM's capacitors are being measured and sorted according to their values. Then based on the arm current's direction these capacitors are mapped according to the sorting algorithm to realize the goal of balancing energy between the n SMs. The details of the control strategy is further explained below.

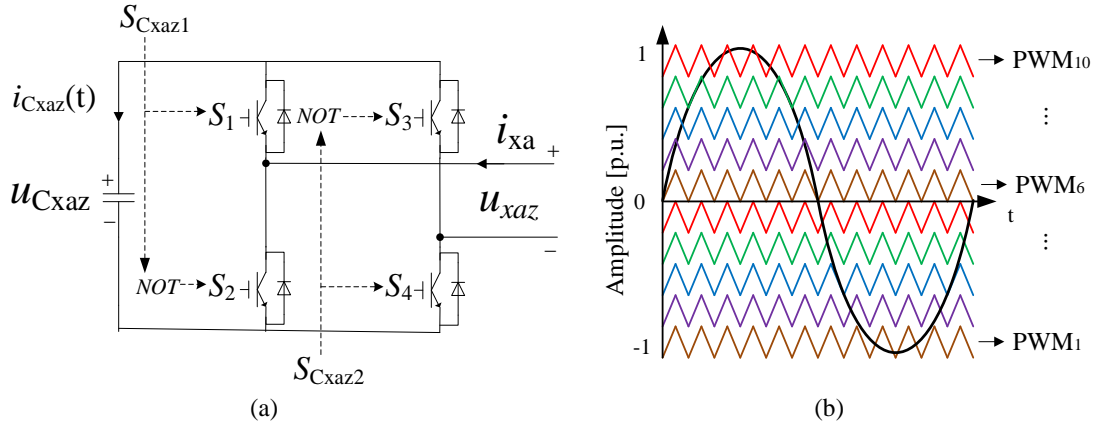


Figure 5.8 (a) Full bridge SM (b) PWM signals of five SMs

The instantaneous power of each SM is defined as: p_{Cxyz} . The dc capacitor voltage of the SM is defined as: U_{Cxyz} as discussed in the previous section. The reference value of the dc capacitor voltage is defined as: U_{Cxyz}^* . Each SM needs two switching signals which can be presented as S_{Cxaz1} , S_{Cxaz2} in sub-converter a as shown in Figure 5.8(a). Assuming there are five SMs in arm_{Aa} of sub-converter a, then two switching signals are S_{CAaz1} , S_{CAaz2} . Therefore, the output voltage of the SM in arm_{Aa} is determined from:

$$u_{Aaz} = S_{CAaz1} \cdot u_{CAaz} - (1 - S_{CAaz2}) \cdot u_{CAaz} \quad (5.18)$$

Whereas, the instantaneous power of each SM is calculated as:

$$p_{Aaz} = u_{Aaz} \cdot i_{Aa} = (S_{CAaz1} + S_{CAaz2} - 1) \cdot u_{CAaz} \cdot i_{Aa} \quad (5.19)$$

Hence:

$$\begin{cases} p_{CAa1} = u_{Aa1} \cdot i_{Aa} = (S_{CAa11} + S_{CAa12} - 1) \cdot u_{CAa1} \cdot i_{Aa} \\ p_{CAa2} = u_{Aa2} \cdot i_{Aa} = (S_{CAa21} + S_{CAa22} - 1) \cdot u_{CAa2} \cdot i_{Aa} \\ \vdots \\ p_{CAa5} = u_{Aa5} \cdot i_{Aa} = (S_{CAa51} + S_{CAa52} - 1) \cdot u_{CAa5} \cdot i_{Aa} \end{cases} \quad (5.20)$$

In Figure 5.8(b), the reference value of arm voltage: u_{Aa}^* is the reference signal and there are ten carrier signals in terms of five SMs. It generates ten PWM signals that defined as: PWM_1 , $PWM_2 \dots PWM_{10}$. For example, when $i_{Aa} > 0$, each SM's instantaneous power could be sorted descending in (5.21):

$$\begin{cases} (PWM_5 + PWM_{10} - 1) \cdot u_{C_{xyz}}^* \cdot i_{Aa} > (PWM_4 + PWM_9 - 1) \cdot u_{C_{xyz}}^* \cdot i_{Aa} \\ (PWM_4 + PWM_9 - 1) \cdot u_{C_{xyz}}^* \cdot i_{Aa} > (PWM_3 + PWM_8 - 1) \cdot u_{C_{xyz}}^* \cdot i_{Aa} \\ (PWM_3 + PWM_8 - 1) \cdot u_{C_{xyz}}^* \cdot i_{Aa} > (PWM_2 + PWM_7 - 1) \cdot u_{C_{xyz}}^* \cdot i_{Aa} \\ (PWM_2 + PWM_7 - 1) \cdot u_{C_{xyz}}^* \cdot i_{Aa} > (PWM_1 + PWM_6 - 1) \cdot u_{C_{xyz}}^* \cdot i_{Aa} \end{cases} \quad (5.21)$$

Then the capacitor voltages should be sorted ascending in order to balance the energy between five SMs in arm_{Aa} . Assuming $u_{CAa1} < u_{CAa2} < u_{CAa3} < u_{CAa4} < u_{CAa5}$, then PWM signals should be mapped to the certain switching signals of each SM as shown in Figure 5.9, which enables the balancing of the capacitors voltage within each arm.

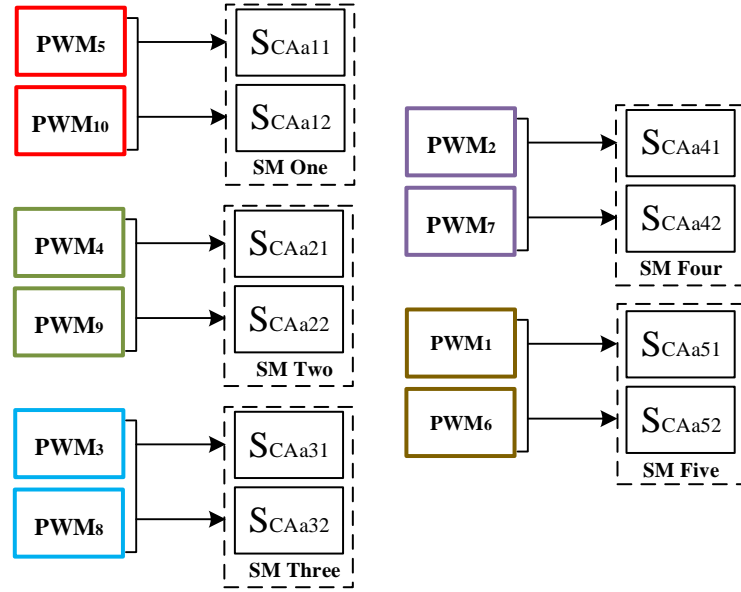


Figure 5.9 PWM signals mapping of SVMM

5.3 Illustrative Simulation Results

The simulation model of M³C for LFAC is developed using MATLAB/SIMULINK software. The input side of M³C is connected to the offshore wind farm (16.7 Hz) while the output side is connected with the on-shore power grid (50 Hz). The simulation parameters are shown in Table II. The offshore wind farm can be up to 630 MW (i.e. The London Array Offshore wind farm). However, on the other hand, 10 MW windfarms are also available in some other areas, such as: offshore wind farm in Taiwan (8 MW), Spain (5 MW), Norway (2 MW) and France (2 MW) [97]. Nevertheless, the simulation model is aimed at verifying the effectiveness of the developed voltage balance control method proposed in this paper and it can easily extend to

higher rated systems with different simulation parameters. There are five capacitors in each arm. The standard 6.6 kV 1.5 kA IGBT module such as the product from Infineon is considered as the power switch to build the SM. The proposed system is tested under different operating conditions to validate the performance of the proposed control strategy.

Table II
Simulation parameters

Description	Parameters	Value
Rated Active Power	P	10 MW
Input RMS line voltage	E_i	11 kV
Input frequency	f_i	16.7 Hz
Input inductance	L_i	4 mH (3.4%)
Output RMS line voltage	E_o	11 kV
Output frequency	f_o	50 Hz
Output inductance	L_o	4 mH (3.4%)
Arm inductance	L	5 mH (4.3%)
Capacitance of SM's capacitor	C_{xyz}	5.1 mF
Rated dc capacitor voltage	$U_{C_{xyz}}$ *	5 kV
Number of SMs per arm	n	5
Switching frequency	f_s	5 kHz

5.3.1 Case I: Steady-state operation

Figure 5.10 shows the simulation results under steady-state operation, where Figure 5.10 (a) and (b) are the input voltage and input current with no phase shift, demonstrating the unity power operation. The arm current contains two frequency components as illustrated in Figure 5.10 (c). According to [95], the tolerance of the capacitor voltage ripple should be $\pm 10\%$. In Figure 5.10 (e), the capacitor voltages of arm_{Aa} in sub-converter a is illustrated, where all five capacitor voltages are tightly balanced around 5 KV with $\pm 2.5\%$ voltage ripple. Furthermore, Figure 5.10 (f) shows the sum of capacitor voltages of all SMs in sub-converter a, which are

perfectly controlled around 25kV.

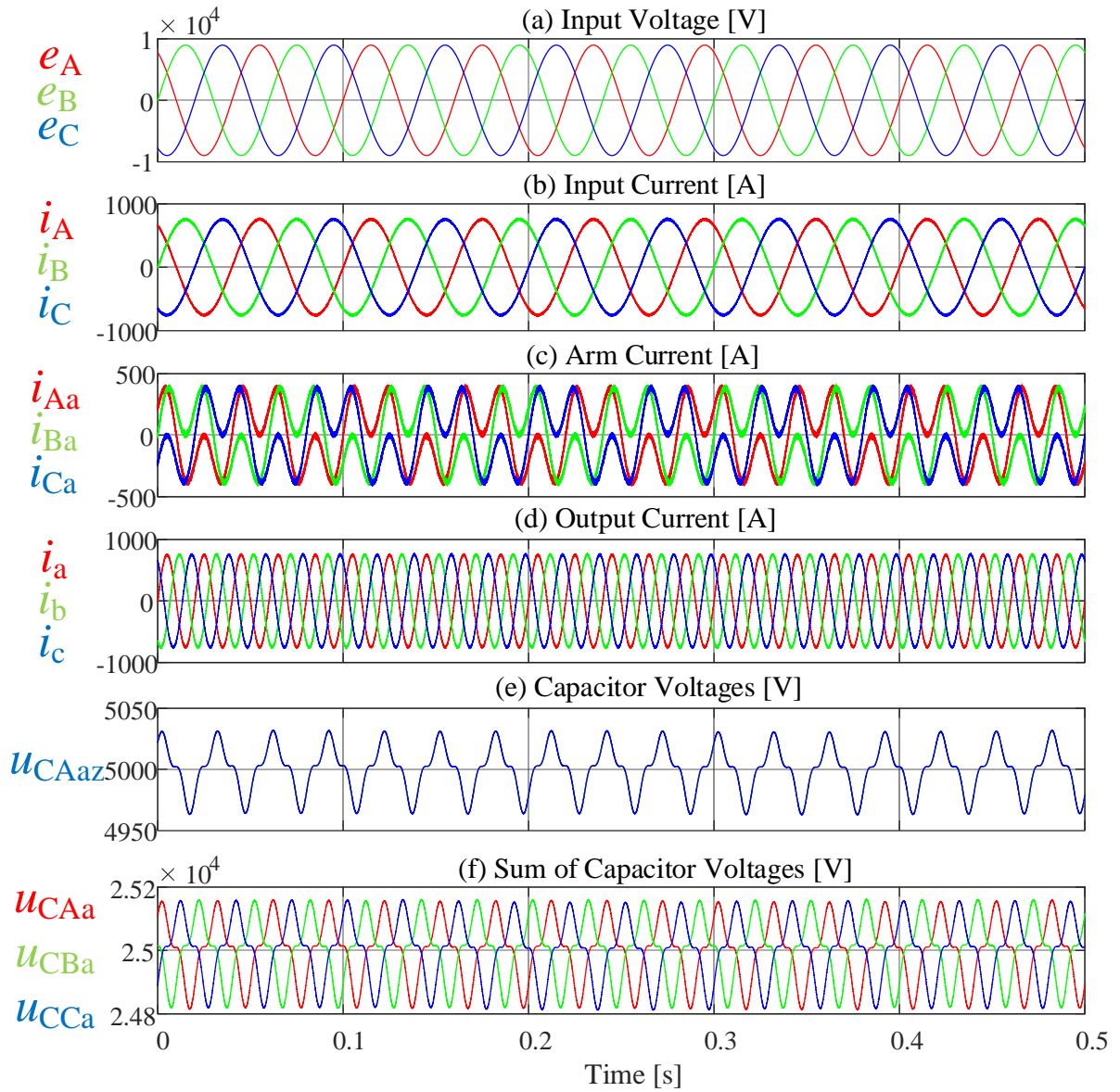


Figure 5.10 Simulation results under steady-state operation

5.3.2 Case II: Dynamic output power operation

Figure 5.11 shows the simulation results under dynamic output power operation. Specifically, Figure 5.11(a) demonstrates the case when the active power supplied by the input side increases from 10 MW to 11 MW at 0.5 s, where the reactive power maintain as zero for the unity power operation. It is worth noting that the capacitor voltages in Figure 5.11(e) and (f) slightly decreased to compensate the active power to the grid from 0.5 s and the proposed control strategy successfully managed to maintain the voltage balance at 0.8 s.

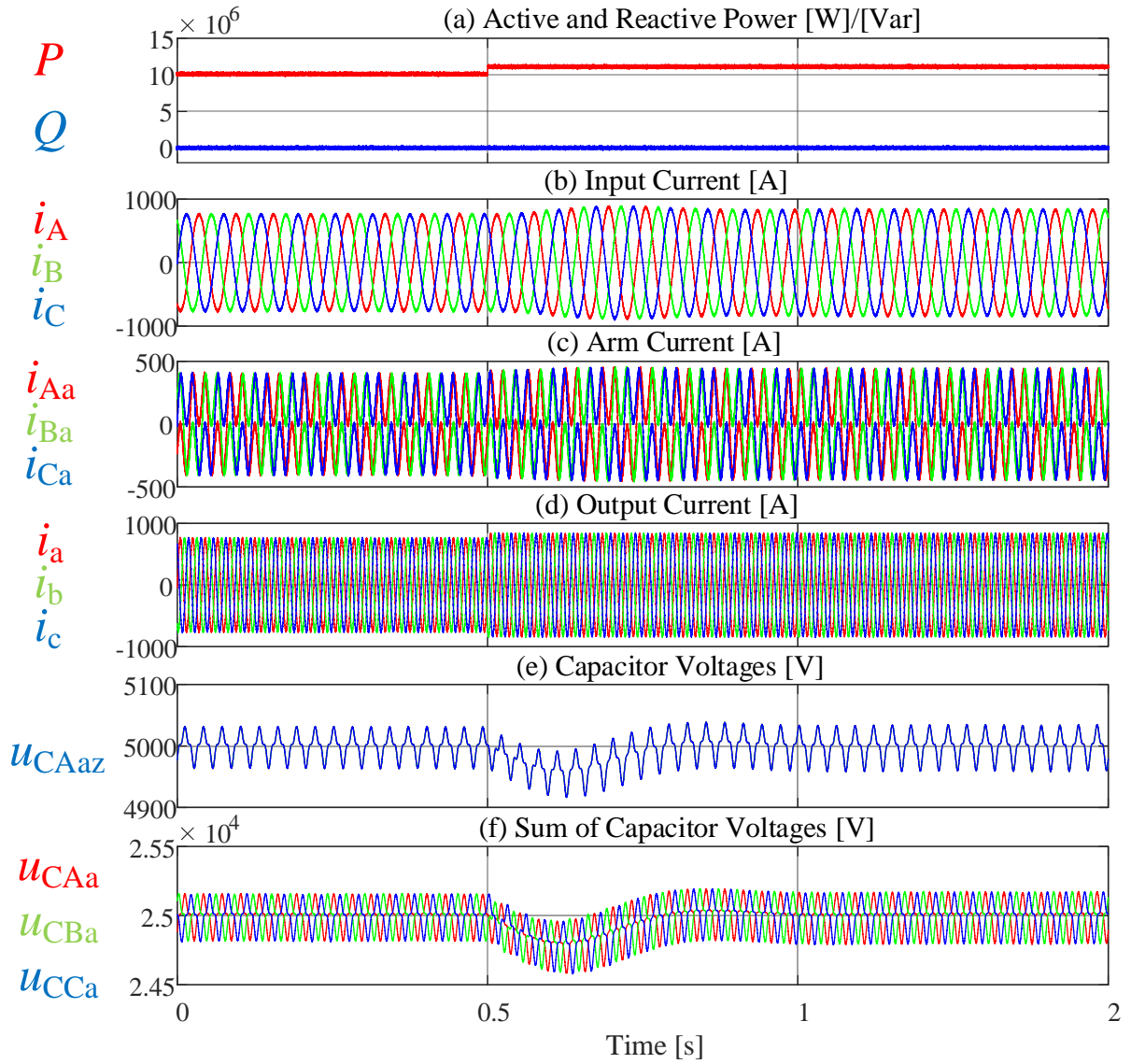


Figure 5.11 Simulation results under a dynamic output power operation

5.3.3 Case III: Unbalanced grid voltage condition

The 5% negative sequence component has been added in the input side of M³C which cause the unbalanced grid voltage condition as shown in Figure 5.12(a), the proposed control strategy illustrated the good performance under this condition. From 0.5 s to 0.8 s, the capacitor voltage balancing control has been deactivated to illustrate the effect of the circulating current. As it can be noticed, from 0 s to 0.5 s, the circulating current control is deactivated, which causing the five capacitors voltages in arm_{Aa} in sub-converter a deviating (i.e. gradually increasing) from the reference voltage. This has also influenced the sum of capacitor voltages of arm_{Aa} (increasing) and arm_{Ba} , arm_{Ca} (decreasing) as shown in Figure 5.12. On the other hand, the

effect of the circulating current can be obviously observed when it is activated at 0.8 s, where the capacitor voltages are quickly re-balanced around 5 kV.

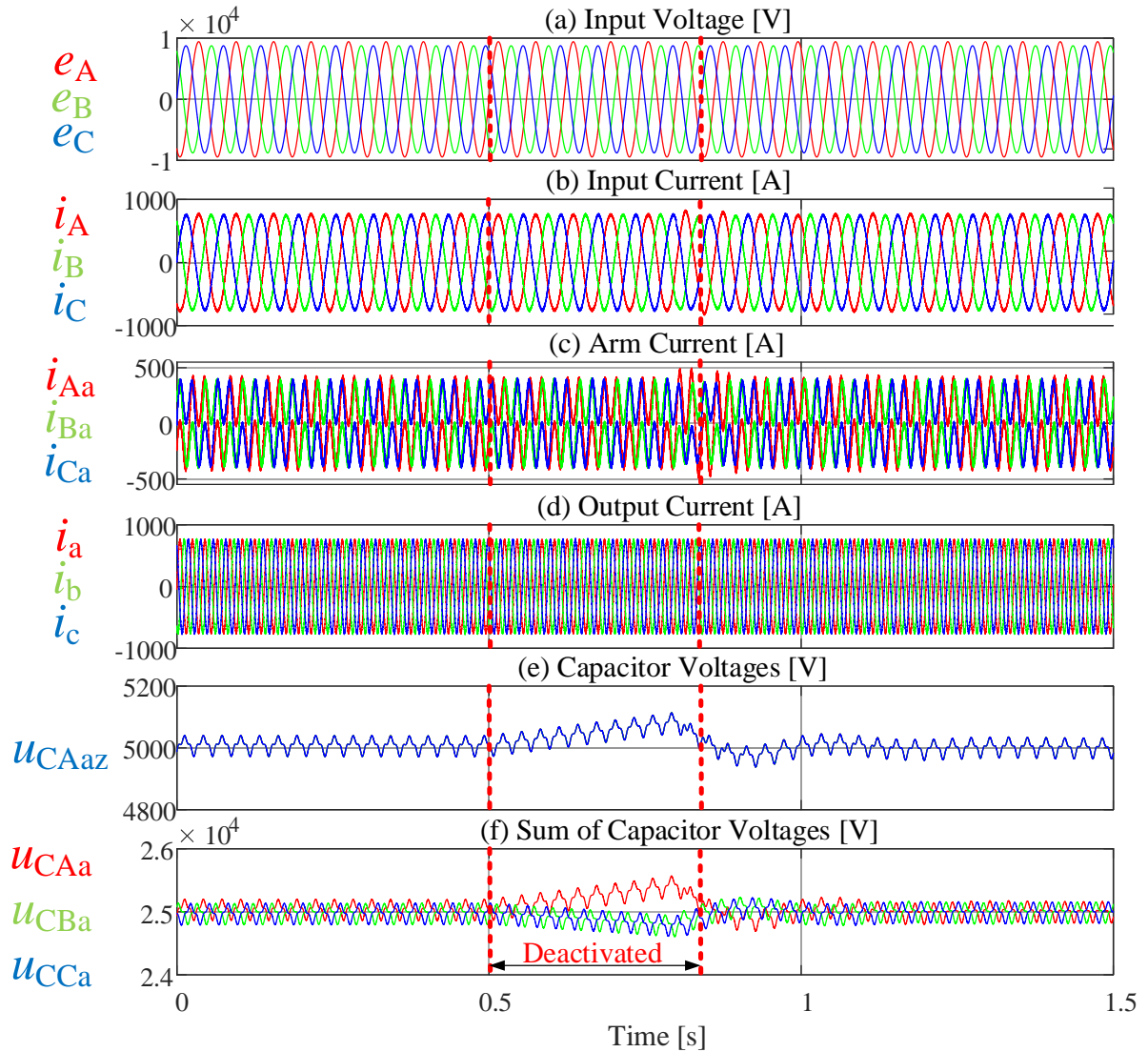


Figure 5.12 Simulation results under unbalanced grid voltage condition

5.4 Summary

Obviously, the proposed control method does not need multiple $\alpha\beta 0$ transformations to decouple the input, output and circulating current. Furthermore, in the ‘double $\alpha\beta 0$ transformation’ control method, four circulating currents on the $\alpha\beta 0$ frame are designed to balance the capacitor voltage between nine arms. Both characteristics of the ‘double $\alpha\beta 0$ transformation’ control method brings the disadvantages of increasing the complexity of the control algorithm. However, the proposed control method achieved the fully independent

control of each sub-converter. The injection of output frequency circulating current has been designed easily and accurately for the purpose of compensating the energy difference between the three arms of each sub-converter, which dramatically decrease the mathematical calculation and control complexity. Furthermore, the selective voltage mapping modulation technique is designed that balances the energy between n sub-modules within each arm. The experimental results from a scaled down laboratory prototype proved the performance of the proposed control method under steady-state and different dynamic operating conditions. The experimental results from a scaled down laboratory prototype which is presented in chapter 7, is in a perfect match with the simulation ones.

Chapter 6 Hierarchical Energy Balance Control Method for M³C based on Injecting Two Frequency Circulating Currents

This chapter presented an improved control method for the energy balance of M³C. It is achieved by incorporating both input and output frequency circulating current on the basis of two set of sub-converters.

6.1 Circuit topology of M³C

Figure 6.1 shows the circuit diagram for M³C which is discussed in the previous chapter where three sub-converters are defined as sub-converter a, sub-converter b and sub-converter c as illustrated in Figure 6.1. In this chapter, the proposed control method for M³C is based on dividing the converter into six sub-converters instead of three as in the previous chapter. Apart from sub-converters a, b and c, the other three sub-converters of M³C are shown in Figure 6.2 which are named as sub-converter A, sub-converter B and sub-converter C.

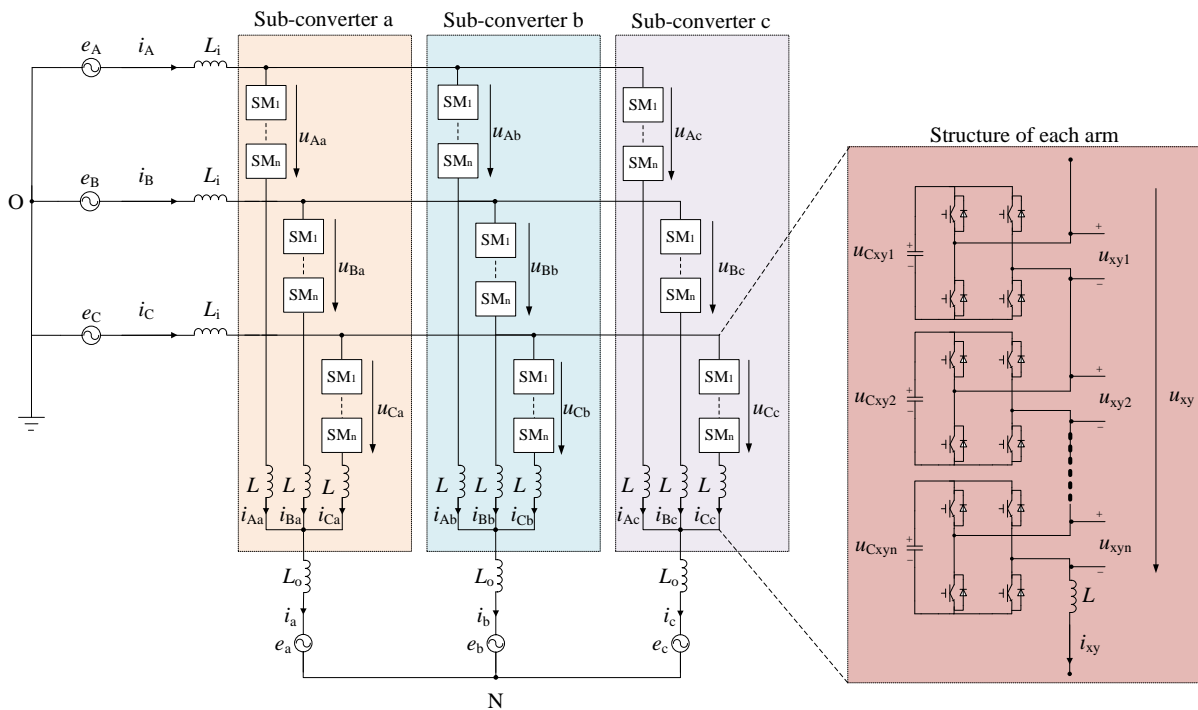


Figure 6.1 Circuit diagram for M³C divided into sub-converters a, b and c

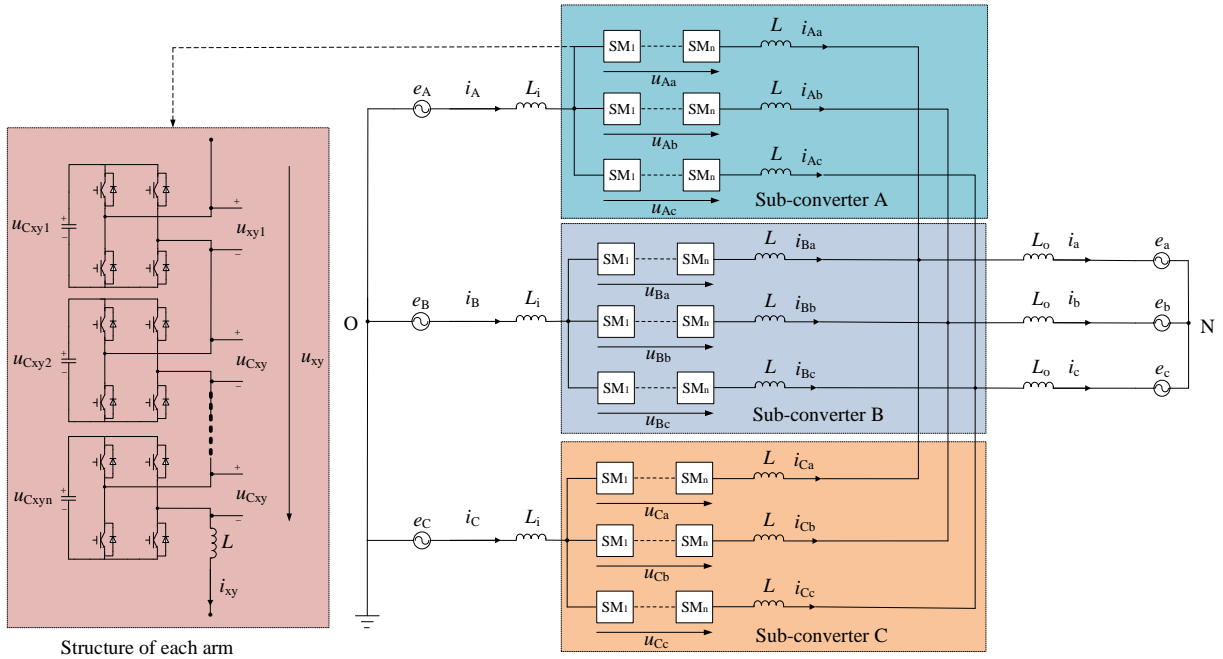


Figure 6.2 Circuit diagram for M³C divided into sub-converters A, B and C

Meanwhile, there are nine arms within these six sub-converters. Therefore, each arm shared by two sub-converters simultaneously. For example, *arm_{Aa}* is shared by sub-converter a and sub-converter A, simultaneously. For clarity, the relationship between the nine arms and six sub-converters is illustrated in details in Table 6.1.

Table 6.1 The relationship between nine arms and six sub-converters

Input side / Output side	Sub-converter A	Sub-converter B	Sub-converter C
Sub-converter a	<i>arm_{Aa}</i>	<i>arm_{Ba}</i>	<i>arm_{Ca}</i>
Sub-converter b	<i>arm_{Ab}</i>	<i>arm_{Bb}</i>	<i>arm_{Cb}</i>
Sub-converter c	<i>arm_{Ac}</i>	<i>arm_{Bc}</i>	<i>arm_{Cc}</i>

6.2 The mathematical model of M³C

In this chapter, the mathematical model is not just developed based on a single sub-converter but rather considers the whole M³C system. First of all, the nine arm currents of M³C are defined in Equation (6.1). There are four current components within the arm current, which are the input current component, output current component and two circulating current components. These two circulating current components are running at input frequency and output frequency,

respectively. The details of the circulating current control will be discussed in this chapter.

Nine arm currents of M³C are given by:

$$\begin{cases} i_{xy} = i_{xy_i} + i_{xy_o} + i_{xy_cir} \\ i_{xy_cir} = i_{xy_cir_i} + i_{xy_cir_o} \end{cases} \quad (6.1)$$

where i_{xy_o} is the output current component. $i_{xy_cir_i}$ is the circulating current running at input frequency of the corresponding arm while $i_{xy_cir_o}$ is the circulating current running at output frequency of the corresponding arm.

Since the three sub-converters a, b and c are connected to the corresponding output phase a, b and c as shown in Figure 6.1, therefore it is easy to deduce that the sum of the three arm currents in each sub-converter is equal to the corresponding output phase current. Meanwhile, the sum of three circulating currents within each sub-converter is equal to zero as discussed in the previous chapter. Hence, the required calculations of arm currents for sub-converters a, b and c are given in Equations (6.2)-(6.4).

For sub-converter a:

$$\begin{cases} i_{Aa} + i_{Ba} + i_{Ca} = i_a \\ i_{Aa_cir_o} + i_{Ba_cir_o} + i_{Ca_cir_o} = 0 \end{cases} \quad (6.2)$$

For sub-converter b:

$$\begin{cases} i_{Ab} + i_{Bb} + i_{Cb} = i_b \\ i_{Ab_cir_o} + i_{Bb_cir_o} + i_{Cb_cir_o} = 0 \end{cases} \quad (6.3)$$

For sub-converter c:

$$\begin{cases} i_{Ac} + i_{Bc} + i_{Cc} = i_c \\ i_{Ac_cir_o} + i_{Bc_cir_o} + i_{Cc_cir_o} = 0 \end{cases} \quad (6.4)$$

Similarly, the sub-converters A, B and C are connected to the corresponding input phase A, B and C as illustrated in Figure 6.2. Therefore, the sum of the three arm currents is equal to the corresponding input phase current while the sum of the three circulating currents within each sub-converter is equal to zero. The required calculations of arm currents for sub-converters A, B and C are given in Equations (6.5)-(6.7).

For sub-converter A:

$$\begin{cases} i_{Aa} + i_{Ab} + i_{Ac} = i_A \\ i_{Aa_cir_i} + i_{Ab_cir_i} + i_{Ac_cir_i} = 0 \end{cases} \quad (6.5)$$

For sub-converter B:

$$\begin{cases} i_{Ba} + i_{Bb} + i_{Bc} = i_B \\ i_{Ba_cir_i} + i_{Bb_cir_i} + i_{Bc_cir_i} = 0 \end{cases} \quad (6.6)$$

For sub-converter C:

$$\begin{cases} i_{Ca} + i_{Cb} + i_{Cc} = i_C \\ i_{Ca_cir_i} + i_{Cb_cir_i} + i_{Cc_cir_i} = 0 \end{cases} \quad (6.7)$$

Then, the output voltages for each arm are defined by Equation (6.8) as:

$$\begin{cases} u_{xa} = e_x - (L_1 + L) \frac{di_{xa_i}}{dt} - (L_o + L) \frac{di_{xa_o}}{dt} - L \frac{di_{xa_cir}}{dt} - e_a \\ u_{xb} = e_x - (L_1 + L) \frac{di_{xb_i}}{dt} - (L_o + L) \frac{di_{xb_o}}{dt} - L \frac{di_{xb_cir}}{dt} - e_b \\ u_{xc} = e_x - (L_1 + L) \frac{di_{xc_i}}{dt} - (L_o + L) \frac{di_{xc_o}}{dt} - L \frac{di_{xc_cir}}{dt} - e_c \end{cases} \quad (6.8)$$

6.3 The Proposed control strategy

The block diagram for the overall energy balance control strategy is shown in Figure 6.3. There are two main differences in terms of the design of the control strategy. Firstly, the energy balance control of the whole M³C has been added in Control Level One. Secondly, the energy balance control between the six sub-converters has been considered in this control strategy. This is achieved by using the circulating current control (two different frequencies) in Control Level Two. This control method enables the energy to be balanced between the nine arms of M³C. The details of the proposed control method are discussed in the following sub-sections.

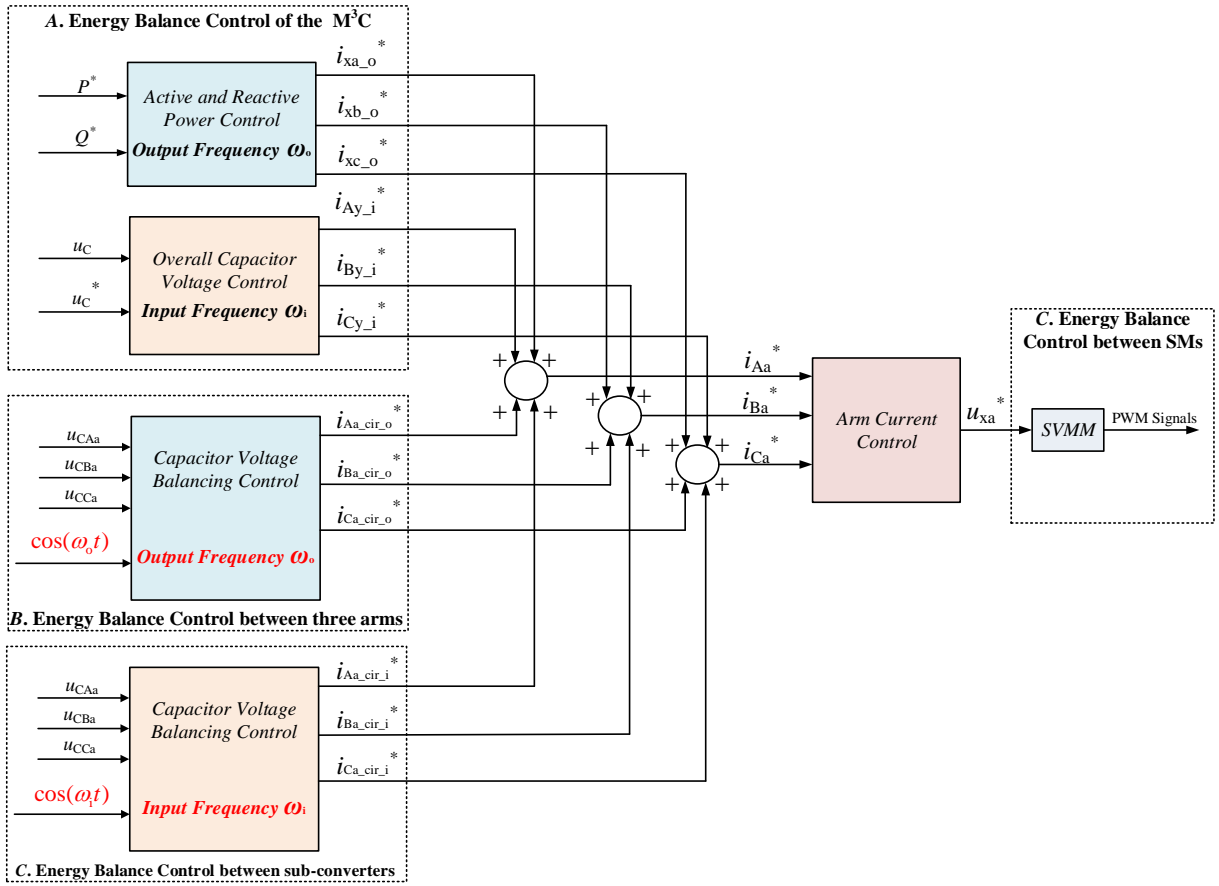


Figure 6.3 The block diagram of the proposed control method in sub-converter a and sub-converter A

6.3.1 Energy balance control of M³C

The first control level of the overall energy balance control strategy to balance the energy of the whole M³C. Therefore, the sum of all the capacitor voltages in M³C should be maintained constant. The input and output currents have an effect on the sum of capacitor voltages. Therefore, the key aim is to keep capacitor voltage sum balanced so that the energy is balanced.

The sum of all capacitor voltages in M³C: u_C is calculated as:

$$u_C = u_{Ca} + u_{Cb} + u_{Cc} \quad (6.9)$$

where u_{Cb} , u_{Cc} are the sum of all capacitor voltages in sub-converter b and c, respectively.

a. Output current control

The output current control block diagram is shown in Figure 6.4 which is same as the output current control discussed in chapter 6. Analysing M³C according to Figure 6.1 where the

converter is divided into sub-converters a, b and c. Therefore, the output current components within the arm current are equal to one third of the output current in each sub-converter. Thereby, the reference value of output current components $i_{xa_o}^*$, $i_{xb_o}^*$ and $i_{xc_o}^*$ of the nine arm currents in M³C have been calculated as:

$$i_{xy_o}^* = \frac{i_y^*}{3} \tag{6.10}$$

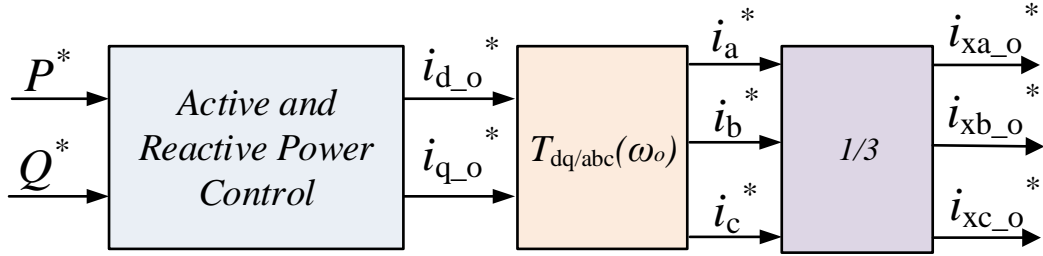


Figure 6.4 Active and reactive power control block diagram

b. Input current control

The control theory of the input current control is similar to that described in the chapter 5. However, the control target of the input current control in this chapter is the energy balance of M³C, where u_c^* in Figure 6.5 is the reference value for u_c . When u_c is bigger than u_c^* , it means there is an extra energy stored within M³C, therefore the input side must decrease the energy that is provided to the converter. Conversely, when u_c is smaller than u_c^* , it means the energy provided to the converter is insufficient, therefore the input side must increase the energy provided to M³C. The ultimate goal of this control block is to keep u_c equal to u_c^* which means the input side meets the required energy demand.

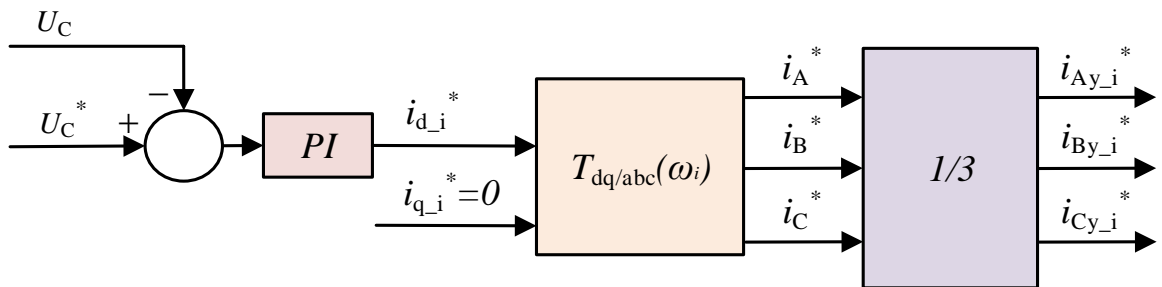


Figure 6.5 The overall capacitor voltage control block diagram

The reference values of the input current: i_A^* , i_B^* and i_C^* are shown in Figure 6.5. Analysing M³C according to Figure 6.2 where the converter is divided into sub-converters A, B and C. Therefore, the input current components within the arm current are equal to one third of the input current in each sub-converter. Hence, the reference value of input current components i_{Ay-i}^* , i_{By-i}^* and i_{Cy-i}^* of the nine arm currents in M³C are calculated from:

$$i_{xy-i}^* = \frac{i_x^*}{3} \quad (6.11)$$

6.3.2 Energy balance control between the three arms in the sub-converter A (circulating current control)

As M³C is divided into sub-converters A, B and C according to Figure 6.2, therefore the next control level is the energy balance between the three arms in sub-converters A, B and C. In this sub-section, only sub-converter A is discussed in details as an example. The energy balance control between the three arms arm_{Aa} , arm_{Ab} and arm_{Ac} in sub-converter A is realized by injecting the circulating current with input frequency. Meanwhile, it is important to be noticed that arm_{Aa} in sub-converter A which also belongs to sub-converter a as presented in Table 6.1. Similarly, the other two arms in sub-converter A: arm_{Ab} belongs to sub-converter b while arm_{Ac} belongs to sub-converter c. Therefore, this control level is also the energy balance control between the sub-converter a, sub-converter b and sub-converter c.

Figure 6.6 shows the energy balance control between the three arms in sub-converter A. The sum of the capacitor voltages in the three arms: arm_{Aa} , arm_{Ab} and arm_{Ac} are defined as: u_{CAa} , u_{CAb} and u_{CAc} , respectively. After passing through the low-pass filter, these three values are denoted by: U_{CAa} , U_{CAb} and U_{CAc} . Then the mean value of these three values can be calculated from:

$$\overline{U_{CA}} = (U_{CAa} + U_{CAb} + U_{CAc})/3 \quad (6.12)$$

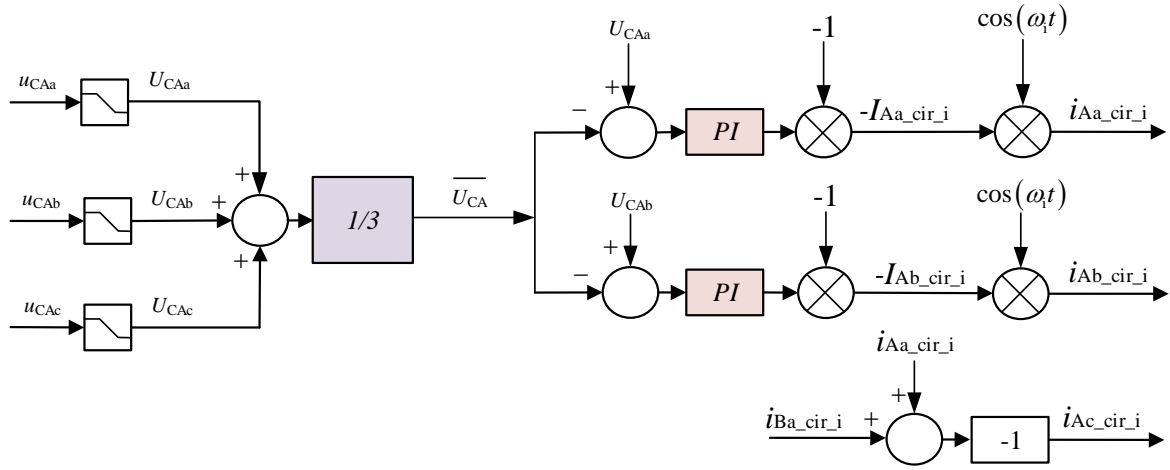


Figure 6.6 The block diagram of the capacitor voltage balancing control in sub-converter A

After U_{CAa} , U_{CAb} and U_{CAc} are compared with the mean value and the error is processed in the PI controller, the peak value of the circulating currents: $I_{Aa_cir_i}$, $I_{Ab_cir_i}$ and $I_{Ac_cir_i}$ are then calculated as illustrated in Figure 6.6. Then, these three values times the constant: -1 because of the opposite direction compared with e_A . The phase angle: $\omega_i t$ of the input voltage e_A is set as a reference phase angle for these three circulating currents. Thereby, the circulating current (input frequency) can be calculated as follows:

$$\begin{cases} i_{Aa_cir_i} = -I_{Aa_cir_i} \cos(\omega_i t) \\ i_{Ab_cir_i} = -I_{Ab_cir_i} \cos(\omega_i t) \\ i_{Ac_cir_i} = -i_{Aa_cir_i} - i_{Ab_cir_i} \end{cases} \quad (6.13)$$

The value of three active powers that are generated by these three circulating currents are defined as: P_{Aa_cir} , P_{Ab_cir} and P_{Ac_cir} which are calculated by:

$$\begin{cases} P_{Aa_cir_i} = -\frac{I_{Aa_cir_i} \cdot E_A}{2} \\ P_{Ab_cir_i} = -\frac{I_{Ab_cir_i} \cdot E_A}{2} \\ P_{Ac_cir_i} = -\frac{I_{Ac_cir_i} \cdot E_A}{2} \end{cases} \quad (6.14)$$

Figure 6.7(a) shows an example of power exchange path between the three arms in sub-converter A which is also the power exchange path between sub-converter a, b and c as illustrated in Figure 6.7(b). This example power exchange path is further discussed in details in the remainder of this section.

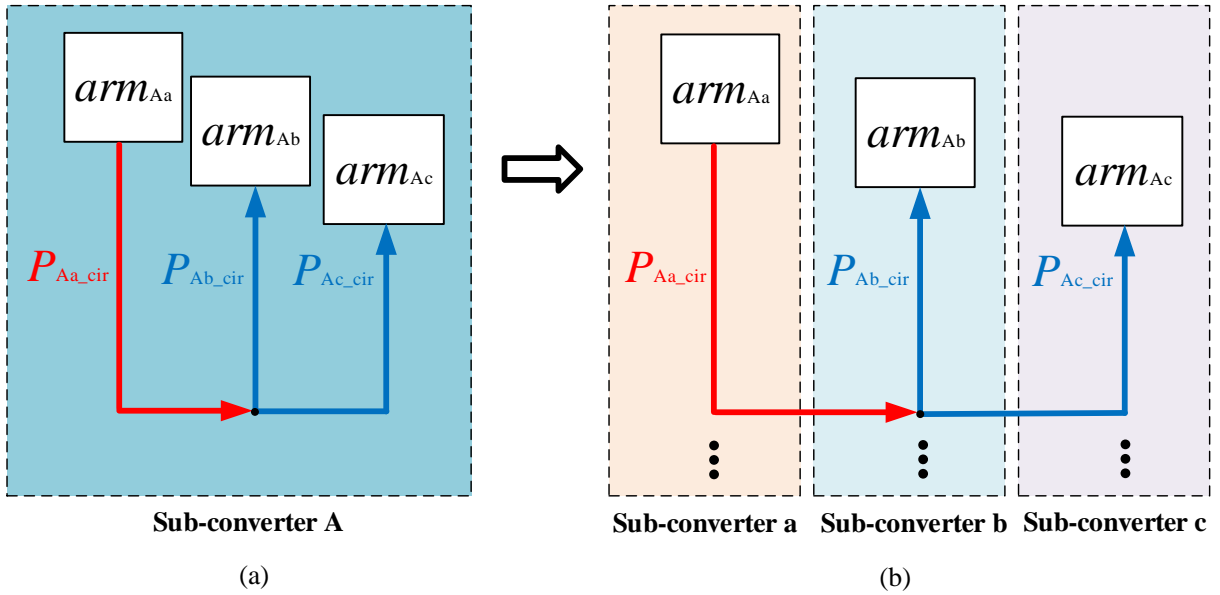


Figure 6.7 An example power exchange path (a) Sub-converter A (b) Sub-converter a, b and c

When:

$$\begin{cases} U_{CAa} - \overline{U_{CA}} > 0 \\ U_{CAb} - \overline{U_{CA}} > 0 \\ U_{CAc} - \overline{U_{CA}} > 0 \end{cases} \quad (6.15)$$

Then after the PI controller the direction of the three circulating currents are determined from:

$$\begin{cases} I_{Aa_cir_i} > 0 \\ I_{Ab_cir_i} < 0 \\ I_{Ac_cir_i} < 0 \end{cases} \quad (6.16)$$

And so according to Equation (6.14):

$$\begin{cases} P_{Aa_cir_i} < 0 \\ P_{Ab_cir_i} > 0 \\ P_{Ac_cir_i} > 0 \end{cases} \quad (6.17)$$

For this condition, the arm_{Aa} should absorb P_{Aa_cir} from the input phase A while arm_{Aa} and arm_{Ab} should supply P_{Ab_cir} and P_{Ac_cir} to the input phase A. Meanwhile, since the sum of the circulating currents is equal to zero as given by Equation (6.5), then:

$$P_{Aa_cir_i} + P_{Ab_cir_i} + P_{Ac_cir_i} = 0 \quad (6.18)$$

Therefore, the circulating current controller controls the $P_{Aa_cir_i}$, $P_{Ab_cir_i}$ and $P_{Ac_cir_i}$ exchange between the three arms to compensate each other in sub-converter A. Hence:

$$P_{Aa} = P_{Ab} = P_{Ac} \quad (6.19)$$

where the value of active powers of these three arms: arm_{Aa} , arm_{Ab} , arm_{Ac} are denoted by: P_{Aa} , P_{Ab} and P_{Ac} , respectively.

The same control theory is applied to sub-converter B and sub-converter C.

In sub-converter B:

$$P_{Ba} = P_{Bb} = P_{Bc} \quad (6.20)$$

where the value of active powers of these three arms: arm_{Ba} , arm_{Bb} , arm_{Bc} are denoted by: P_{Ba} , P_{Bb} and P_{Bc} , respectively.

Similarly, in sub-converter C:

$$P_{Ca} = P_{Cb} = P_{Cc} \quad (6.21)$$

where the value of active powers of these three arms: arm_{Ca} , arm_{Cb} , arm_{Cc} are denoted by: P_{Ca} , P_{Cb} and P_{Cc} , respectively.

On the other hand, the value of active powers of sub-converter a, b and c are denoted by: P_a , P_b and P_c , respectively. Therefore, according to Equations (6.19)-(6.21), it is easy to be deduced that:

$$P_a = P_b = P_c \quad (6.22)$$

where,

$$\begin{cases} P_a = P_{Aa} + P_{Ba} + P_{Ca} \\ P_b = P_{Ab} + P_{Bb} + P_{Cb} \\ P_c = P_{Ac} + P_{Bc} + P_{Cc} \end{cases} \quad (6.23)$$

In summary, the energy balance control between three arms in sub-converter A, B and C, respectively also ensure balanced the energy between sub-converters a, b and c.

6.3.3 Energy balance control between three arms of the sub-converter a (circulating current control)

Although the energy of the sub-converters a, b and c is controlled as discussed in the previous section, however, this does not necessarily mean that the energy between the sub-converters A, B and C is balanced. Similarly, analysing M³C according to Figure 6.1 where the converter is divided into sub-converters a, b and c. In this sub-section, only sub-converter a is discussed in

details for an example. Figure 6.8 illustrates the proposed capacitor voltage balancing control with injecting circulating current (output frequency), which balances the energy between the three arms of sub-converter a which is also the energy balance control between sub-converters A, B and C. The control theory is similar to that discussed in Chapter 5.

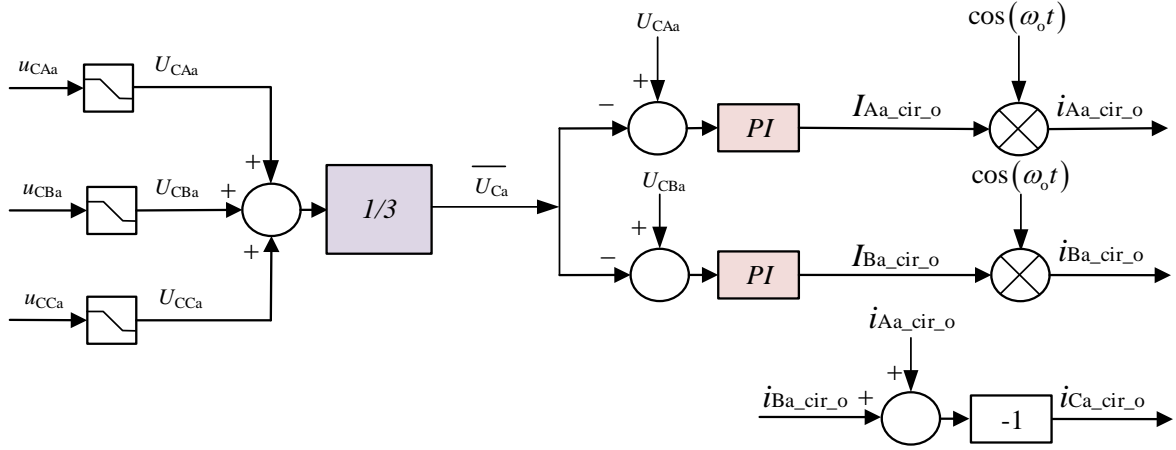


Figure 6.8 The block diagram of the capacitor voltage balancing control in sub-converter a

The phase angle, $\omega_0 t$ of the output voltage e_a is set as the reference phase angle for all three circulating currents since these three arms of sub-converter a are connected with output phase a. Therefore, the calculation of the circulating currents is given by:

$$\begin{cases} i_{Aa_cir_o} = I_{Aa_cir_o} \cos(\omega_0 t) \\ i_{Ba_cir_o} = I_{Ba_cir_o} \cos(\omega_0 t) \\ i_{Ca_cir_o} = -i_{Aa_cir_o} - i_{Ba_cir_o} \end{cases} \quad (6.24)$$

The value of active powers that are generated by the circulating currents are defined as: $P_{Aa_cir_o}$, $P_{Ba_cir_o}$ and $P_{Ca_cir_o}$ and are calculated as follows:

$$\begin{cases} P_{Aa_cir_o} = \frac{I_{Aa_cir_o} \cdot E_a}{2} \\ P_{Ba_cir_o} = \frac{I_{Ba_cir_o} \cdot E_a}{2} \\ P_{Ca_cir_o} = \frac{I_{Ca_cir_o} \cdot E_a}{2} \end{cases} \quad (6.25)$$

Figure 6.9 shows an example power exchange path between the three arms in sub-converter a, which is discussed further in details in the remainder of this section.

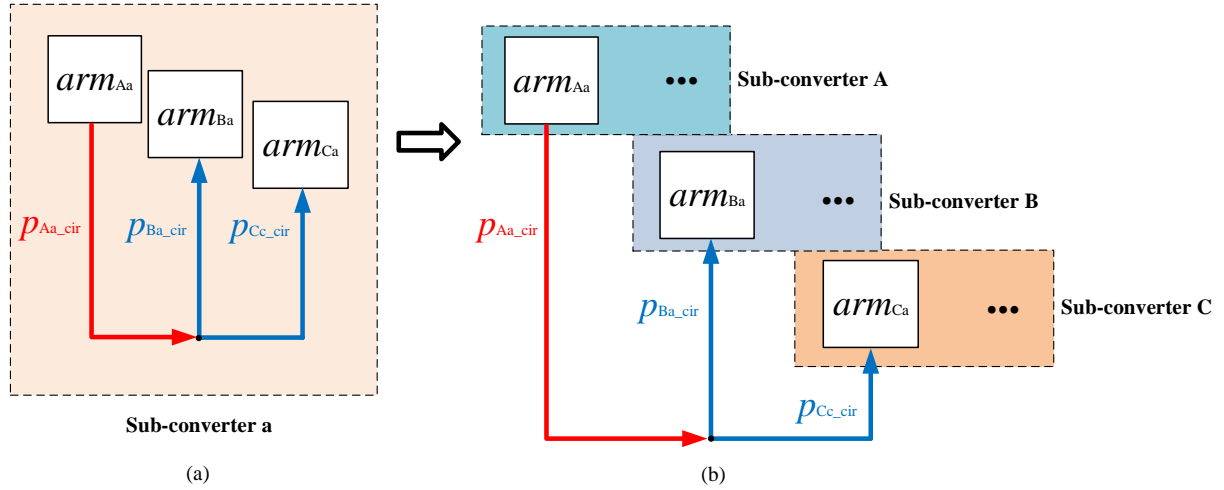


Figure 6.9 An example power exchange path (a) Sub-converter a (b) Sub-converter A, B and C

When:

$$\begin{cases} U_{CAa} - \overline{U_{Ca}} > 0 \\ U_{CBa} - \overline{U_{Ca}} > 0 \\ U_{CCa} - \overline{U_{Ca}} > 0 \end{cases} \quad (6.26)$$

Then after the PI controller, the direction of the three circulating currents are determined from:

$$\begin{cases} I_{Aa_cir_o} > 0 \\ I_{Ba_cir_o} < 0 \\ I_{Ca_cir_o} < 0 \end{cases} \quad (6.27)$$

And so according to Equation (6.25):

$$\begin{cases} P_{Aa_cir_o} > 0 \\ P_{Ba_cir_o} < 0 \\ P_{Ca_cir_o} < 0 \end{cases} \quad (6.28)$$

For this condition, the arm_{Aa} should supply $P_{Aa_cir_o}$ to the output phase a while arm_{Ba} and arm_{Ca} should absorb $P_{Ba_cir_o}$ and $P_{Ca_cir_o}$ from the output phase a. Meanwhile, since the sum of the circulating currents is equal to zero then:

$$P_{Aa_cir_o} + P_{Ba_cir_o} + P_{Ca_cir_o} = 0 \quad (6.29)$$

Therefore, the circulating current controller controls $P_{Aa_cir_o}$, $P_{Ba_cir_o}$ and $P_{Ca_cir_o}$ only exchange between the three arms to compensate with each other. Therefore, similar analysis as discussed in the previous section, it is concluded as:

$$\begin{cases} P_{Aa} = P_{Ba} = P_{Ca} \\ P_{Ab} = P_{Bb} = P_{Cb} \\ P_{Ac} = P_{Bc} = P_{Cc} \end{cases} \quad (6.30)$$

Hence:

$$P_A = P_B = P_C \quad (6.31)$$

where the value of active powers of sub-converter A, B and C are denoted by: P_A , P_B and P_C , respectively and these three powers are calculated as:

$$\begin{cases} P_A = P_{Aa} + P_{Ab} + P_{Ac} \\ P_B = P_{Ba} + P_{Bb} + P_{Bc} \\ P_C = P_{Ca} + P_{Cb} + P_{Cc} \end{cases} \quad (6.32)$$

In summary, the energy balance control between three arms in sub-converter A, B and C, respectively also balances the energy between sub-converters a, b and c in the meantime.

According to this sub-section and sub-section 6.3.2, it is important to conclude that:

$$P_{Aa} = P_{Ab} = P_{Ac} = P_{Ba} = P_{Bb} = P_{Bc} = P_{Ca} = P_{Cb} = P_{Cc} \quad (6.33)$$

Equation (6.33) means that the circulating current control balances the active power of nine arms in M³C.

6.3.4 The arm current control

Figure 6.10 shows the arm current control of sub-converter a which is developed by Equation (6.1) The reference value of the arm current i_{xa}^* consists of four current components: $i_{xa_i}^*$, $i_{xa_o}^*$, $i_{xa_cir_i}$ and $i_{xa_cir_o}$ as described in the previous sections.

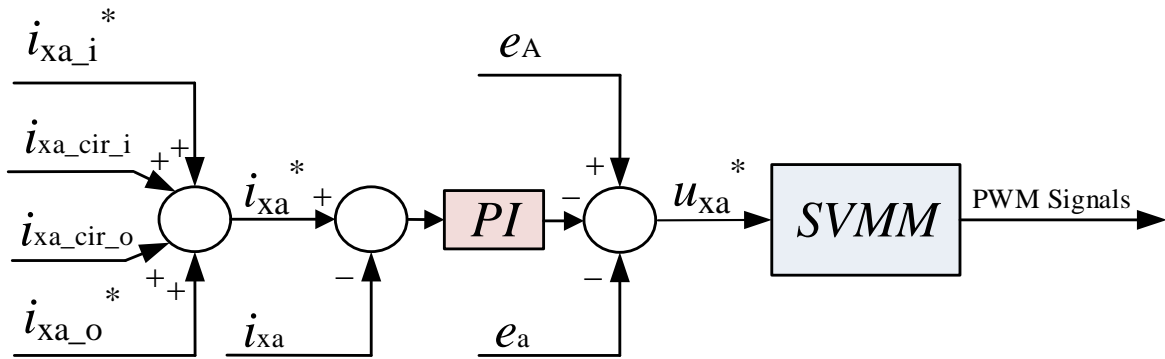


Figure 6.10 Arm current control block diagram

The difference between the i_{xa} and i_{xa}^* are calculated first, then the reference value of the three arm voltages u_{xa}^* can then be calculated by Equation (6.8). By using the selective voltage mapping modulation technique (SVMM) as discussed in the following section, the PWM signals can be generated for each SM.

6.3.5 Energy balance control between n SMs of each arm (SVMM)

In each arm, the SM's energy should be balanced which indicates the balance of the capacitor voltage. Therefore, a third control level is required to control the SM's capacitors voltage. The selective voltage mapping modulation (SVMM) discussed in chapter 6 is considered here again for this chapter.

6.4 Illustrative simulation results

The simulation model of M³C that function as the frequency converter in the LFAC transmission system is developed using MATLAB/SIMULINK software which is the same as discussed in chapter 5. The proposed control method is tested under different operating conditions to validate the effectiveness and the performance of the control strategy as presented in this chapter.

6.4.1 Case I: Steady-state operation

Figure 6.11 shows the simulation results under steady-state operation, where Figure 6.11(a) and (b) are the input voltage and input current respectively with no phase shift, hence demonstrating the unity power operation. The arm current contains two frequency components as illustrated in Figure 6.11(c). The capacitor voltages of arm_{Aa} are illustrated in Figure 6.11(e), where all five capacitor voltages are tightly balanced around 5 kV with voltage ripple $\pm 5\%$. Furthermore, Figure 6.11(f) shows the sum of the capacitor voltages of all SMs in sub-converter a, which are all perfectly controlled around 25 kV.

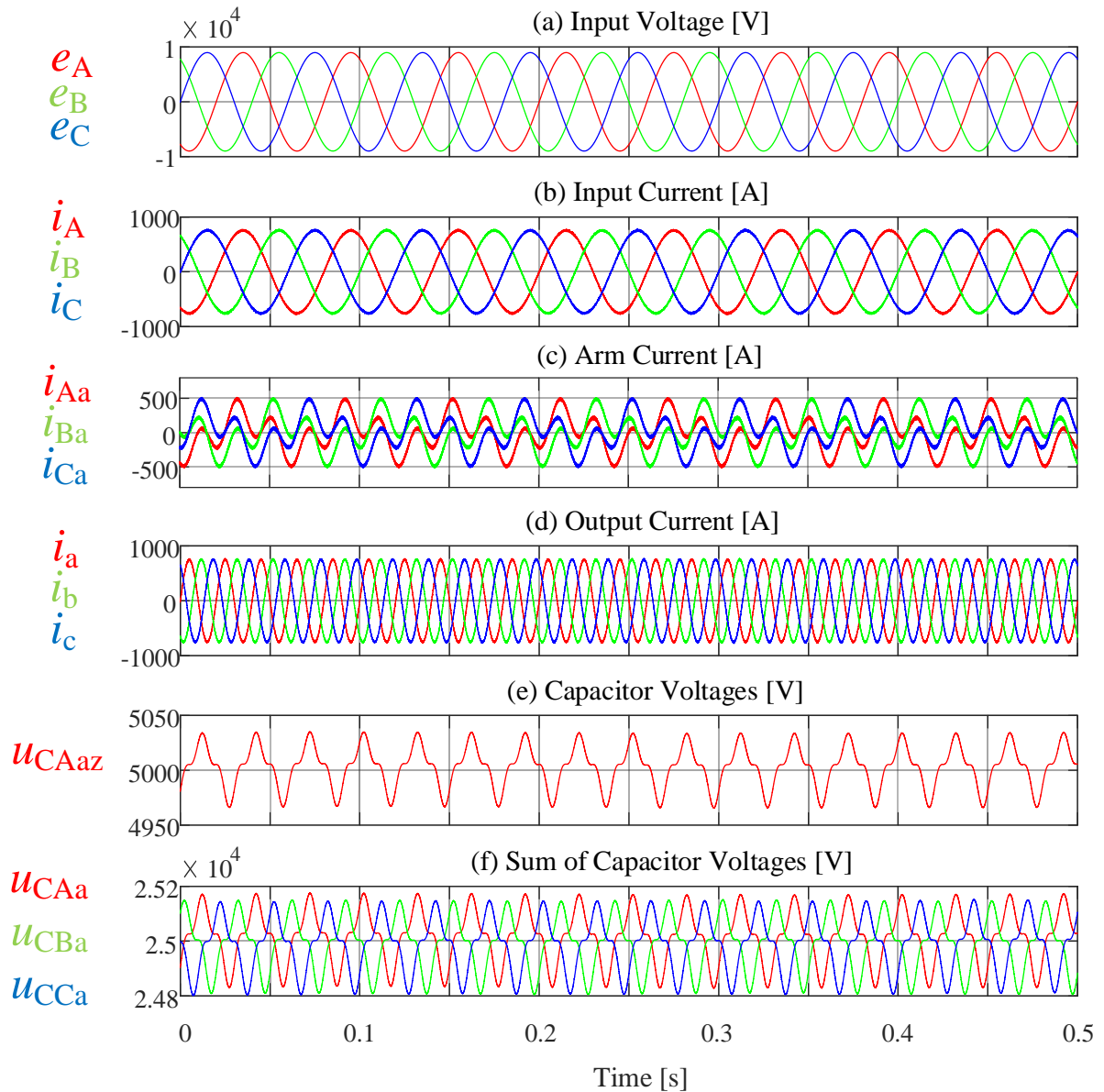


Figure 6.11 Simulation results under steady-state operation

6.4.2 Case II: Dynamic output power operation

Figure 6.12 shows the simulation results under dynamic output power operation. Specifically, Figure 6.12(a) demonstrates the case when the active power supplied by the input side increases from 10 MW to 11 MW at 0.5 s, where the reactive power maintain as zero for the unity power operation. It is worth noting that the proposed control strategy successfully managed to maintain the voltage balance of the five SMs' capacitors in Figure 6.12(e) and (f).

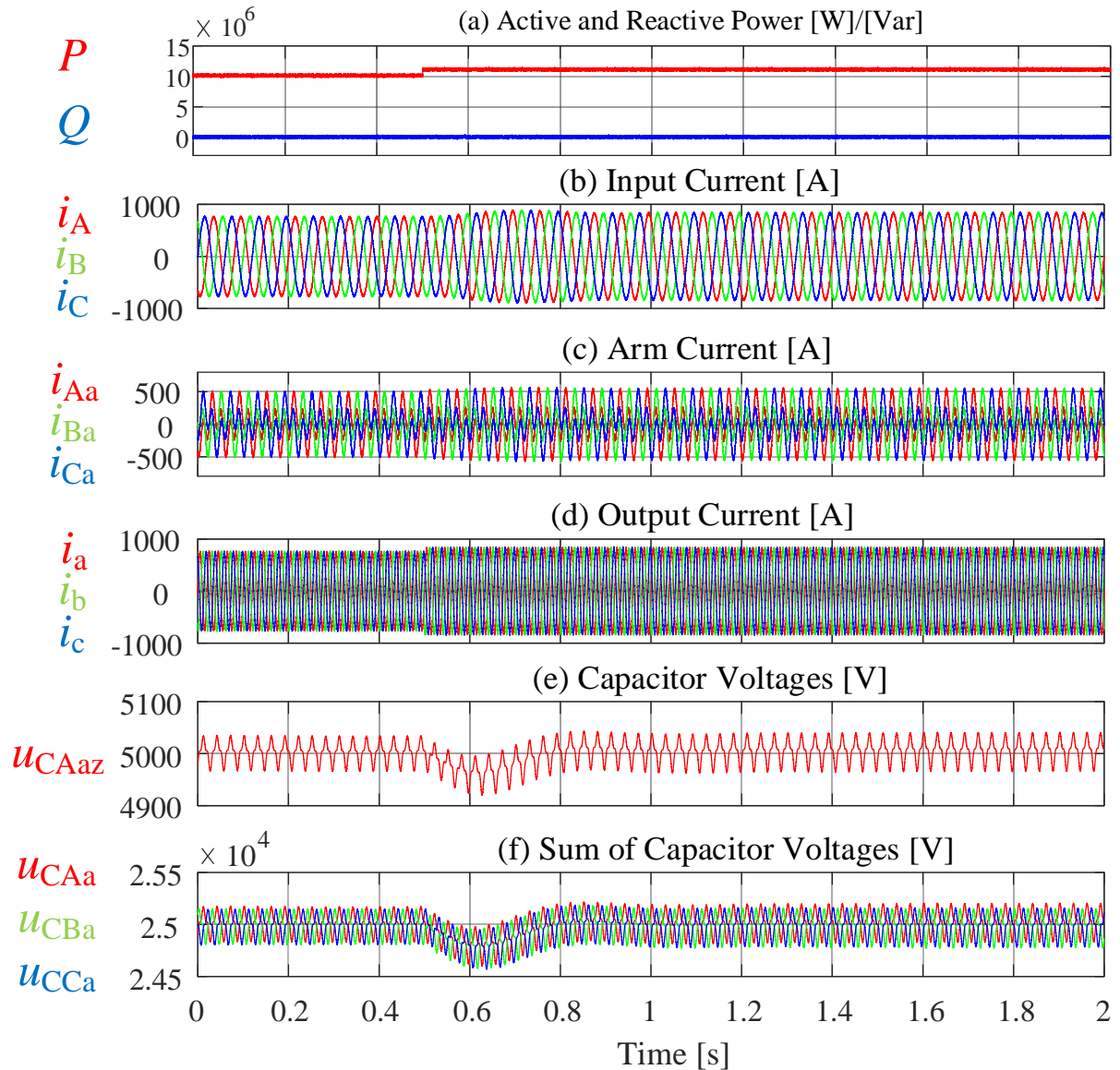


Figure 6.12 Simulation results under dynamic output power operation

6.5 Comparison between the ‘double $\alpha\beta 0$ transformation’ control method and proposed control methods

In terms of the complexity of the voltage balancing control, the comparison between three control methods has been given in Figure 6.13. The complexity of the mathematical calculation is determined by how many accumulator, multiplier, sin and cos in the coding of these three methods based on the CCS platform. Obviously, the amount of accumulator, multiplier, sin and cos of the ‘double $\alpha\beta 0$ transformation’ control method are much more than the proposed control methods.

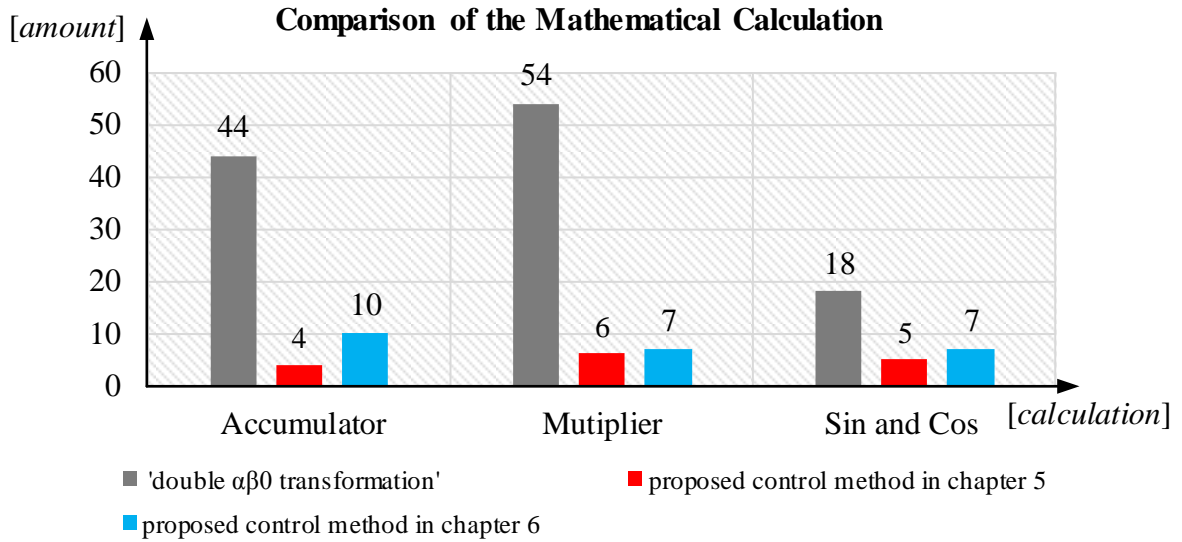


Figure 6.13 Comparison of the mathematical calculation between three control methods

As shown in Figure 6.14, the operation time of 'double $\alpha\beta 0$ transformation' control method is 4117 CPU period and the proposed control methods only take half of the time, 2553 CPU period (CPU frequency is 200 MHz). Therefore, the proposed control method effectively reduced the control complexity and the associated mathematical calculation with reduced operation time. It is important to mention that all the data are based on the coding of the author to achieve the fairest results.

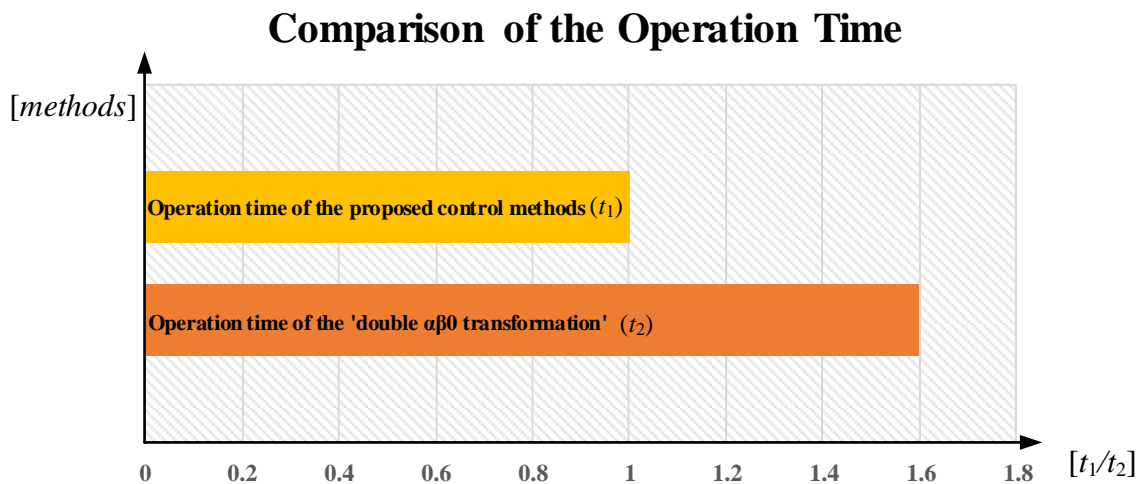


Figure 6.14 Comparison of the operation time between three control methods

According to Figure 6.14, the reduced operation time brings the following merits:

- A low-cost processor which saves the cost of the converter.
- Reduce the time delay of the controller which can increase the control bandwidth of the

system and improve the dynamic performance of the converter.

Meanwhile, the simplified control structure as proposed in chapter 5 and chapter 6 brings the following merits:

- The sub-converter is controlled independently so that M³C is decoupled to three independent converters, which simplifies the design procedure.
- The injection of the circulating current is also simple since they are in phase with the arm output voltage.

6.6 Summary

Different with the proposed control method in chapter 5, the M³C is divided into six sub-converters with each sub-converter controlled independently. The injection of input frequency circulating current is responsible for capacitor voltage balance between three arms in sub-converter A, B and C while the injection of output frequency circulating current is responsible for capacitor voltage balance between three arms in sub-converter a, b and c. As the six sub-converters shares nine arms, the input and output frequency circulating current balanced the capacitor voltage between nine arms. It is important to mention that, although there are more controllers added in the proposed control method in chapter 6, the control complexity is only slightly increased compared with chapter 5. Furthermore, it alleviates the negative impact of the injected circulating current on the external grid and allows the M³C systems work through larger grid unbalance situations. The comparison between three control methods clearly indicate that the proposed control methods are simplified than the most commonly used ‘double $\alpha\beta 0$ transformation’ control method.

Chapter 7 Experimental Validation

7.1 Experimental setup

The experimental platform for three-phase to three-phase M³C is demonstrated in Figure 7.1. The input side is connected with a three-phase programmable AC source (50 Hz). The output side is connected with a three-phase inductive load (16.7 Hz). There are nine arms in M³C as illustrated in Figure 7.1 and each group of three arms is defined as one sub-converter. For example, the sub-converter a comprises: arm_{Aa} , arm_{Ba} and arm_{Ca} .

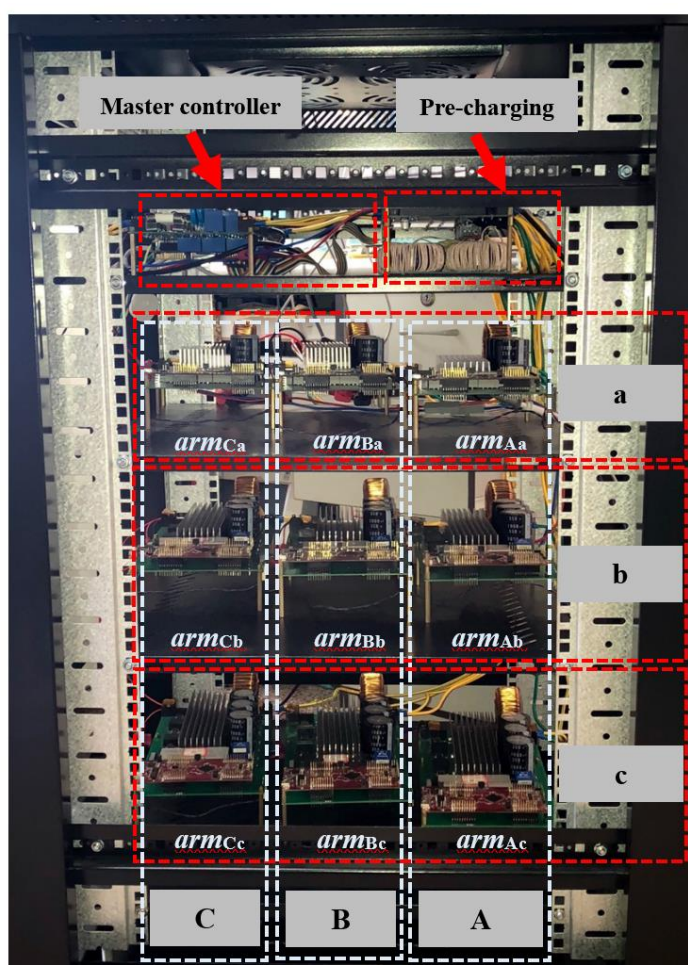


Figure 7.1 Experiment platform of the three phase to three phase M³C

The upper level of the prototype comprises the master controller and the pre-charging module. The function of the pre-charging module is to pre-charge all of capacitors before the experiment to avoid an overvoltage or overcurrent situations. The experimental setup is realized by using a distributed control network. It contains ten controllers (TMS320F2837xS) with one master

controller for M³C's system control and one arm controller for each arm. The communication is achieved by using CAN.

7.2 Design and function of M³C prototype

7.2.1 Distributed control network of M³C prototype

M³C has the advantages of flexibility and scalability which means that the number of SMs could be extended to satisfy any voltage rating. However, the resultant problem is that the number of PWM and measurement signals increase in the meantime. For example, this prototype has 108 PWM and 48 sampling signals in total. In terms of the conventional centralized control network, the limitation due to the number of PWM outputs of the DSP, means that the controller is usually chosen to be a combination of the DSP and FPGA. The DSP is responsible for the serial algorithm, while the FPGA calculates the parallel algorithm and extends the number of PWM outputs. The design idea of the centralized control network is instinctive and simple but the complicated wiring hinders the scalability of the system. Therefore, a distributed control network has been chosen to make full use of the advantages of M³C. The ideal design of the distributed control network is based on SM-level, but the cost of that is too high. Consequently, the distributed control network in this project is based at the arm-level which means all the SMs in one arm share the same arm controller. Figure 7.2 illustrates the structure of this scheme, which includes one master controller and nine arm controllers. These controllers exchange data through the communication network.

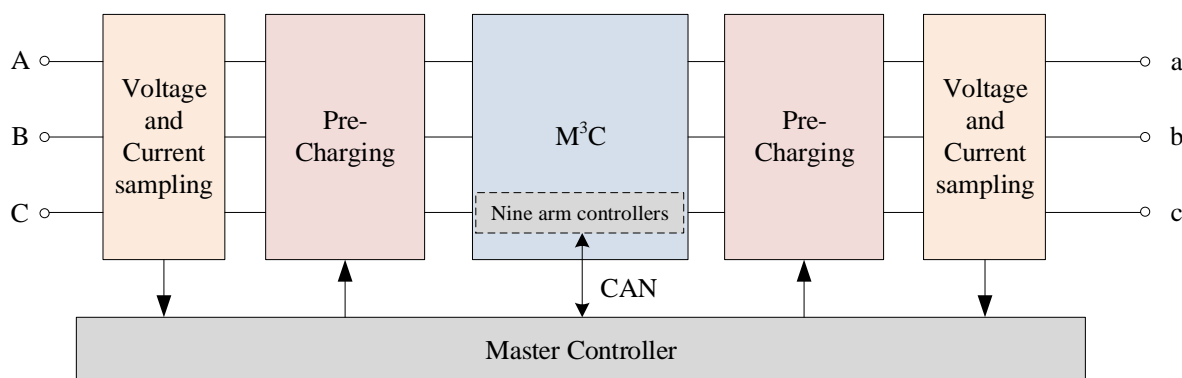


Figure 7.2 The distributed control network of M³C

The distributed control network of M³C is illustrated in detail in Figure 7.3, the master

controller is responsible for the overall control target. Specified control targets can be listed as follows:

- Measuring the input and output current and realizing the requirements from the system level.
- Calculating the reference value of the arm current according to the received value of capacitor voltage and then sending the reference value to the arm controller.
- Sending synchronization signals based on its own clock to ensure clock synchronization.
- Handling system-level faults and status information from the arm controller.

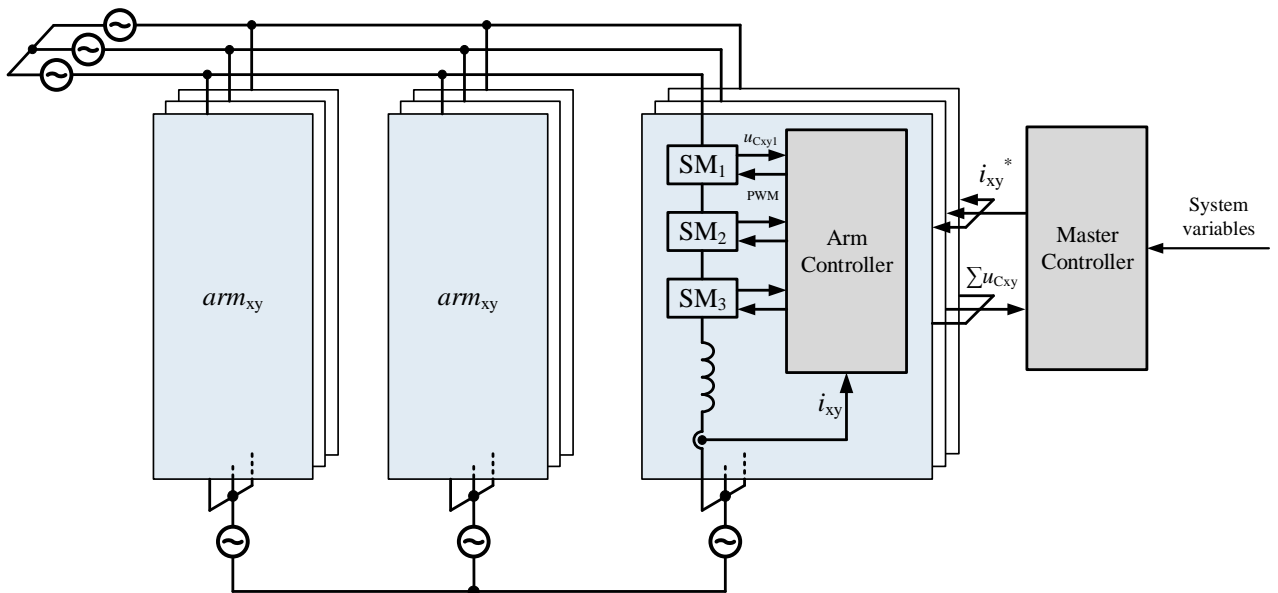


Figure 7.3 Function of the master controller

Figure 7.4 illustrates the function of the arm controller. The biggest difference compared with the centralized control network is the local controller which handles more complex real-time control tasks. Specific control targets are:

- Measuring the capacitor voltage and the arm current and send them to the system controller.
- Performing real-time current and voltage control loops to generate PWM signals.
- Handling the fault signals from the power switches and also sending the status signals to the master controller.

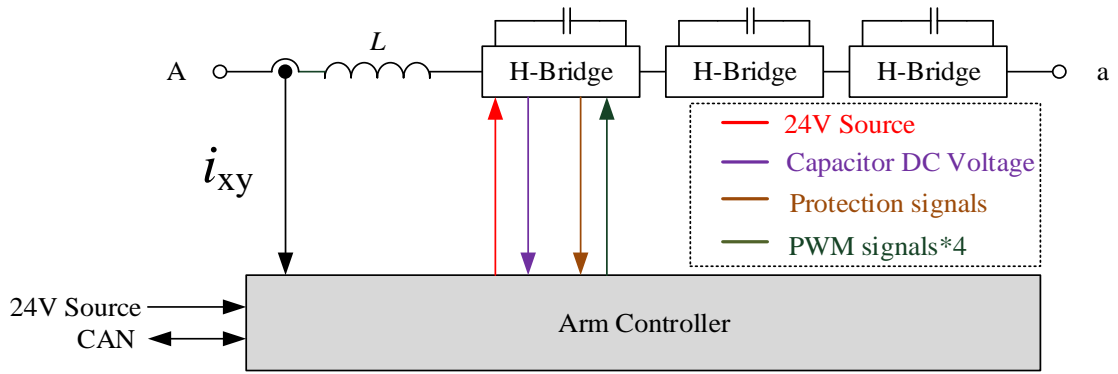


Figure 7.4 Function of the arm controller

Figure 7.5 shows the full structure of the distributed control network of M³C. Again, it clearly shows the layout of the ten controllers with one master controller and one arm controller for each of the nine arms.

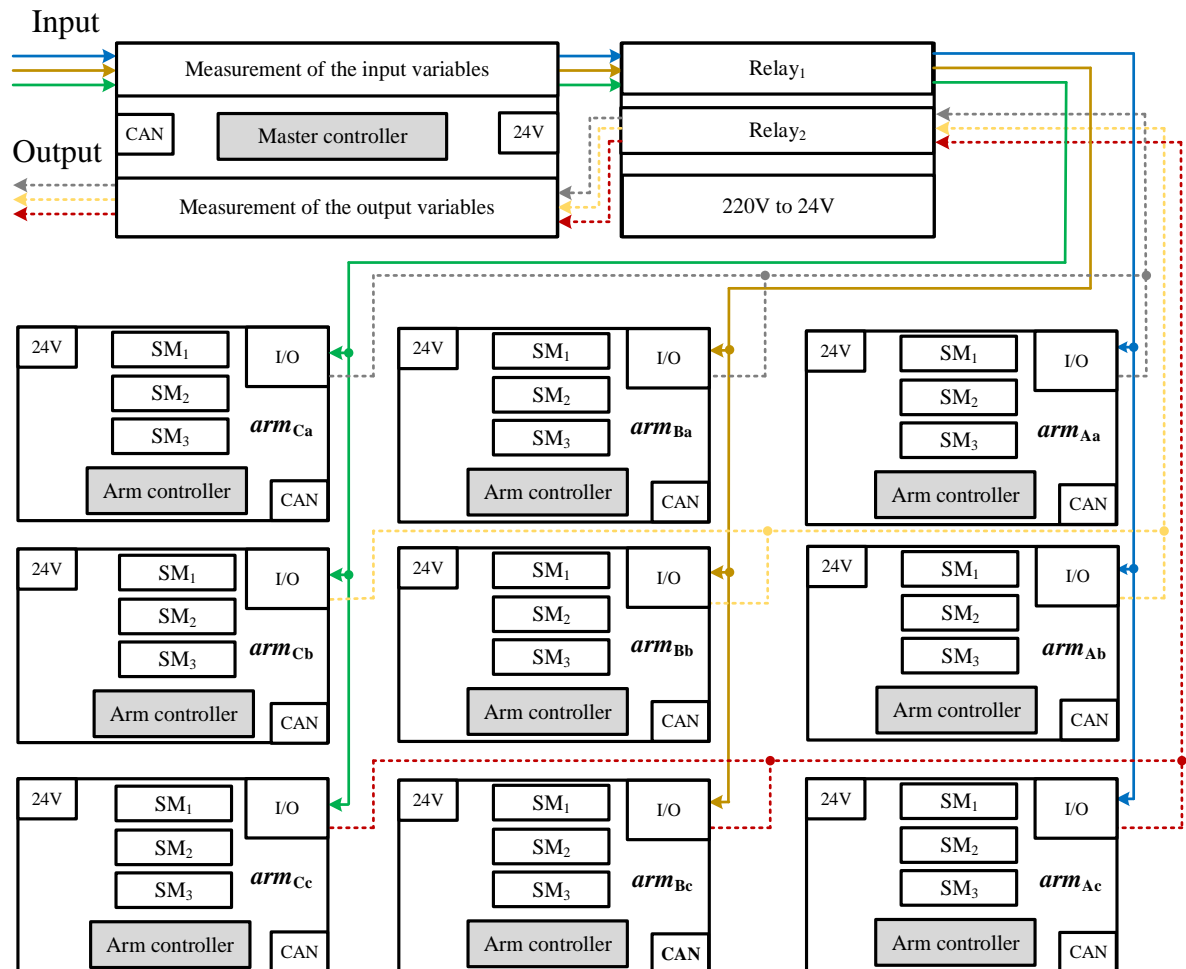


Figure 7.5 The distributed control network of M³C in details

7.2.2 Communication Network

The control algorithm should be used in every controller in the distributed control network. Therefore, an appropriate communication network is required. Figure 7.6 shows four possible types of typical structure of communication networks.

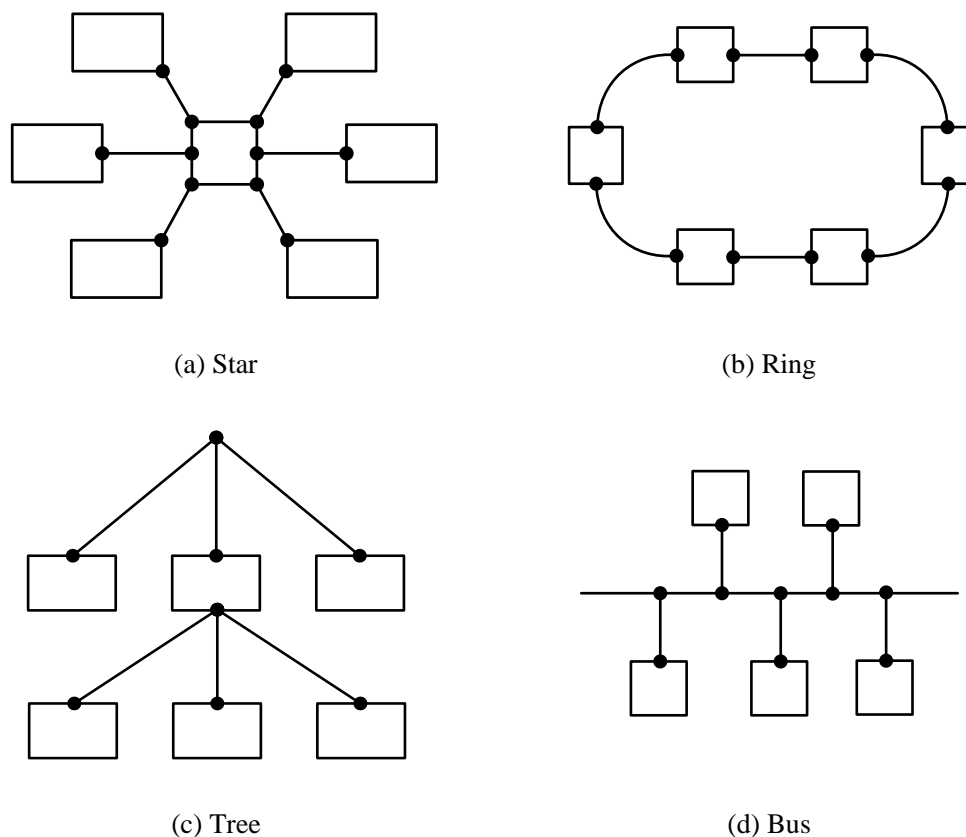


Figure 7.6 Four typical structures of the communication network

- 1) Figure 7.6(a) shows the star structure which means that each controller is connected into a network in the shape of a star. The advantages of the star structure are as follows: The structure is simple and easy to construct and maintain. There is only a small network delay and low transmission errors. However the cost of the star structure is high while the reliability is low. In addition its ability to share resources is poor. Hence, the star structure is not suitable to be applied in distributed power electronic systems.
- 2) The ring structure is formed by multiple nodes connected through the closed loop point-to-point links as shown in Figure 7.6(b). This structure is able to provide a large throughput with simple control software but when the number of nodes is high the information transmission rate is slowed down. However since the structure is a closed loop network it

is not conducive to be expanded. In addition the information flows in a fixed direction through in the network which means that one faulty node will cause the entire network to fail.

- 3) Figure 7.6 (c) shows the tree network which can be regarded as an extended form of the star network. The adaptability of the topology is very strong and there are few restrictions on the number of connectable devices and the transmission rate.
- 4) The bus structure is the most widely used communication network in terms of industrial data communication as illustrated in Figure 7.6(d). Any node on the bus can send the data and all the other nodes can receive it. The network for the bus structure is easy to install but as the transmission distance increases, the signal strength gradually decreases. Hence the number and distribution of connectable devices are limited by the cable length. However, the bus structure is still very suitable for the hierarchical distributed communication network.

The communication technology has been widely applied in the industry, and some schemes have been used in the distributed control of MMC. In order to solve the problems of the delayed communication and the processing of large amounts of data, a high speed network is usually required such as: PROFINET, MACRO and EtherCAT. The EtherCAT for example is an open fieldbus system and uses a master-slave architecture based on Ethernet. EtherCAT is capable of delivering high-precision in terms of the clock synchronization (error: $\pm 20\text{ns}$). For example, an EtherCAT-based distributed control communication network for MMC is shown in Figure 7.7.

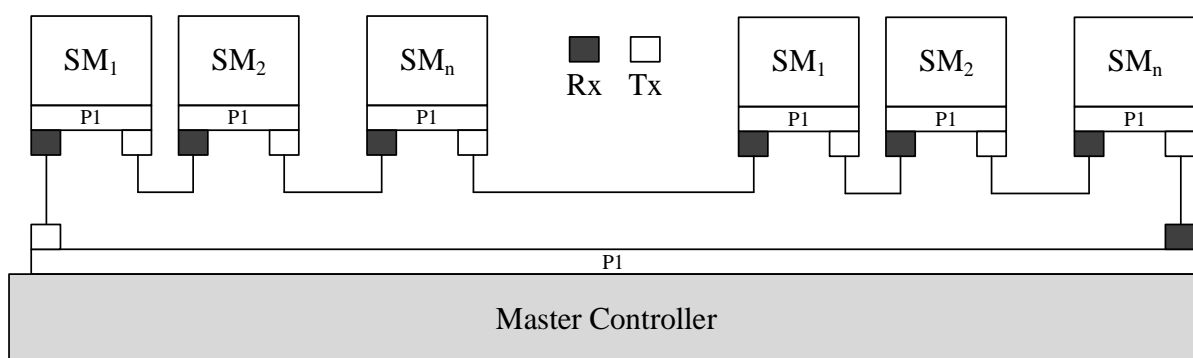


Figure 7.7 The distributed control network (ring structure) based on EtherCAT for MMC where, Rx and Tx means the receiver and transmitter, respectively. P1 is the communication port.

However a high speed communication network usually has weaker ability to resist noise and provides lower reliability with a higher cost. Considering the serious EMI environment in the power electronic converter, the CAN bus with low bandwidth and strong noise immunity is selected as the communication bus for this prototype as shown in Figure 7.8. The CAN bus has a transport distance of 40m at the speed of 1Mbps, which is enough for M³C in this project. Since the core of the CAN is integrated in the DSP, no extra communication chip is required. However the transceiver chip SN65HVD234 is added in the board to function as the isolation between the DSP and the wire.

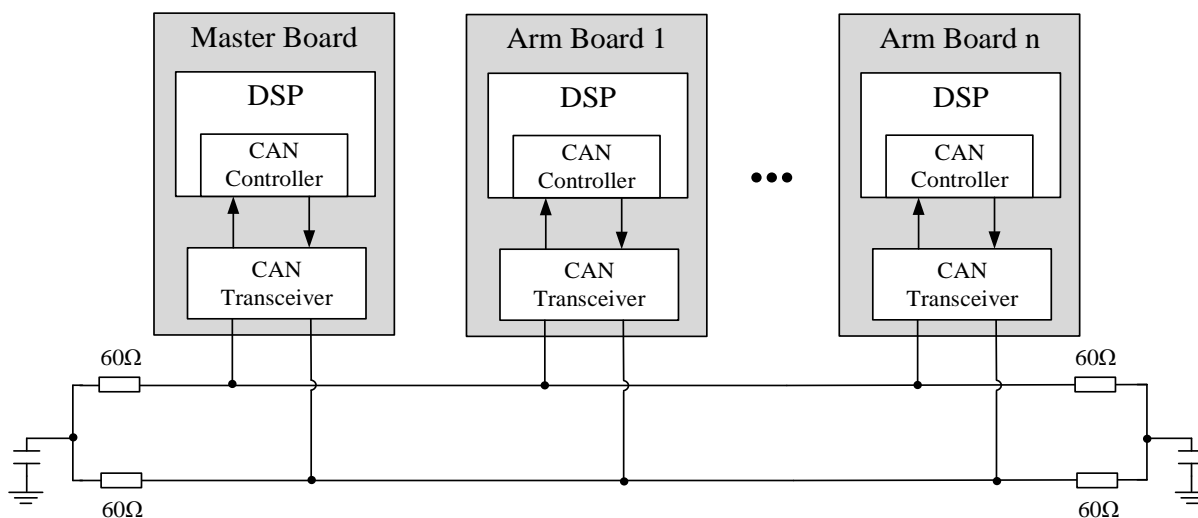


Figure 7.8 Structure of the CAN bus in the distributed control network of M³C

Figure 7.9 depicts the CAN interface which is designed from aspect of EMC. P_1 and P_2 are the communication ports while L_1 is the common mode inductor which is used to filter the common mode noise in the differential line. C_3 and C_4 are the filter capacitors, which provide a low-impedance path for the noise and usually is selected as 100pF. D_1 and D_2 is the 3.5V TVS diode which is used to suppress the surge voltage.

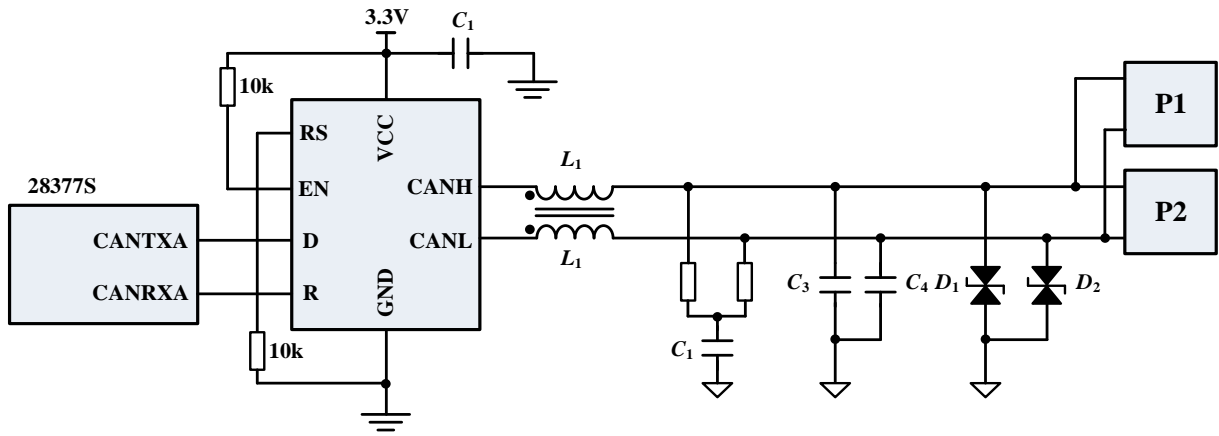


Figure 7.9 Schematic of the CAN interface

Figure 7.10 shows the communication of the distributed control network in M³C by using CAN bus. All ten controllers receive and transmit signals between each other so that each controller can receive and transmit the desired signals in terms of its function. Figure 7.10 also shows how the auxiliary power supply is connected between the nine arms in M³C.

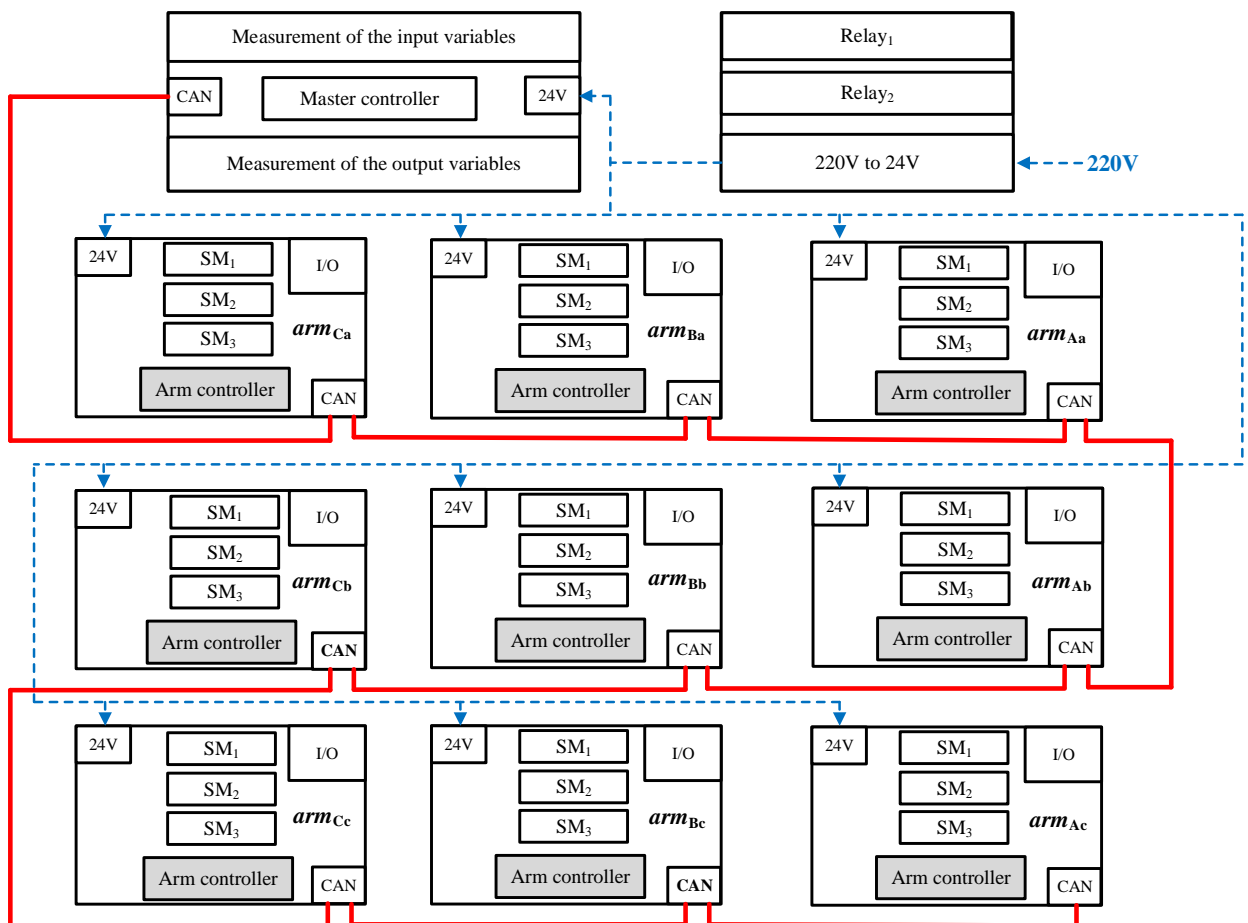


Figure 7.10 The communication of the distributed control network by using CAN

7.2.3 The design of the software for the distributed control network of M^3C

The coding of the control method and system command is based on the CCS platform using C language. As shown in Figure 7.11, the software design of the whole system is divided into three parts: (1) The arm-level: (shown in orange) represents the programming of the PWM generation and sampling (capacitor voltage balance control in each arm); (2) The system-level: (shown in blue) implements the energy balance control of each sub-converter or between sub-converters and also provides the energy balance control between the three arms in each sub-converter; (3) The user-level (shown in grey) is the top level in terms of the software control. Through the human-computer interaction interface, the user is able to monitor the operational status of the system, set the parameters, view real-time waveforms, debug control parameters, and even perform online upgrades to the arm-level and system-level.

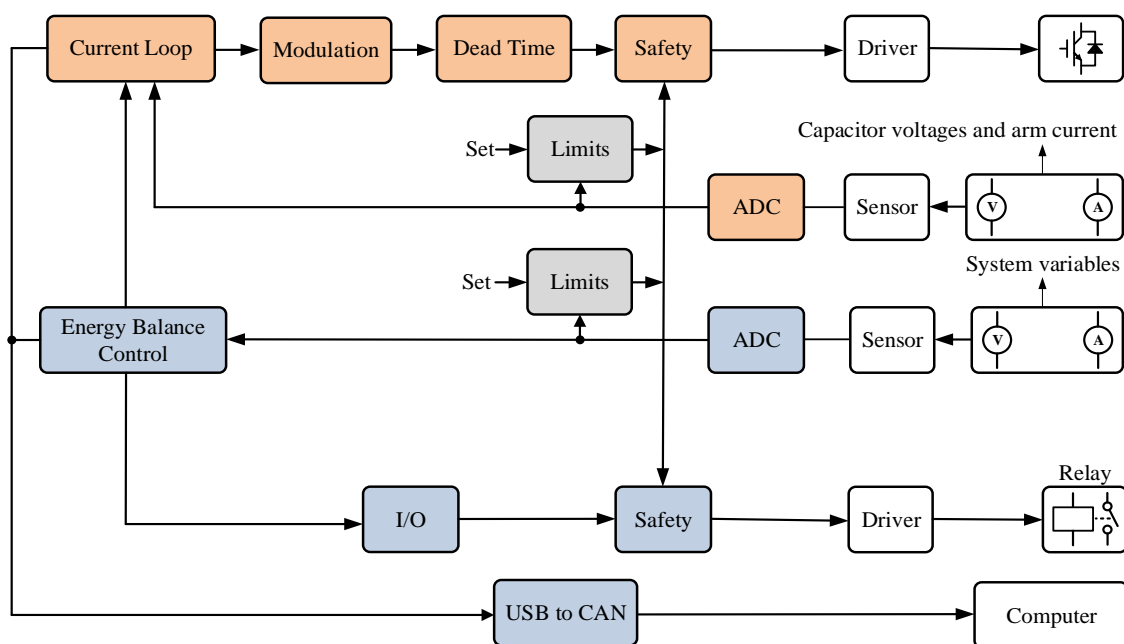


Figure 7.11 The design of the software for the distributed control network of M^3C

7.3 The design of the arm board of M^3C

The circuit diagram of the arm in M^3C is shown in Figure 7.12(a). There are three SMs within each arm and each SM contains a dc-link capacitor, one IGBT module, four optocouplers (HCPL4504), one voltage hall sensor and several isolated auxiliary power supplies as illustrated in Figure 7.12.

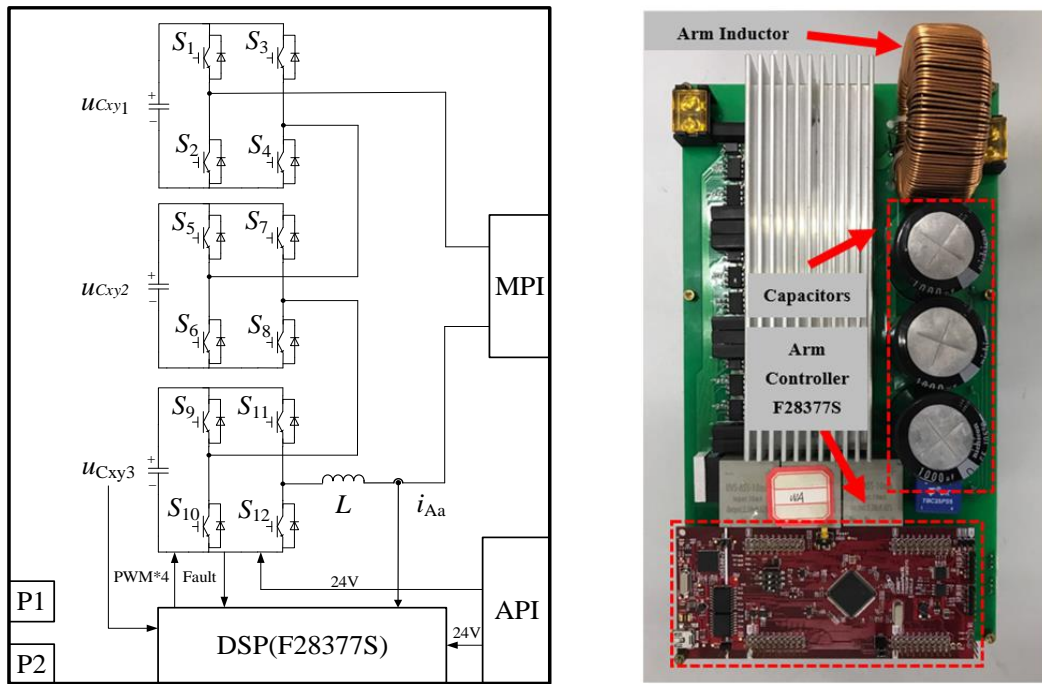


Figure 7.12 (a) Circuit diagram of the arm in M³C (b) The arm board

where MPI is the main power supply interface, API is the auxiliary power interface and P1 and P2 are the communication ports of CAN.

According to the datasheet, each controller (TMS320F28337xS) has a frequency of 200MHz which can generate 24 PMW output and support 12 ADC input. It also contains various communication buses including the CAN bus used in this prototype. As shown in Figure 7.13, the DSP is connected to the computer through the simulation chip (FT223H) and USB to provide the functions such as the debugging and loading of the program. The LED indicates the status of the system and the reset button is used to reset the system manually.

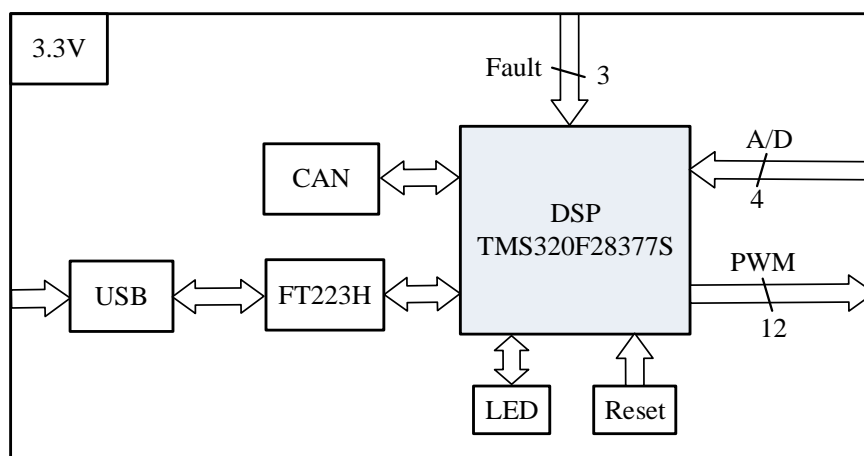


Figure 7.13 Schematic of the DSP controller

7.4 The design of the full-bridge sub-module

Figure 7.14 shows the design of the full-bridge SM board in M³C. Each full-bridge SM contains a dc-link capacitor, one IGBT module, four optocouplers (HCPL4504), one voltage hall sensor and several isolated auxiliary power supplies.

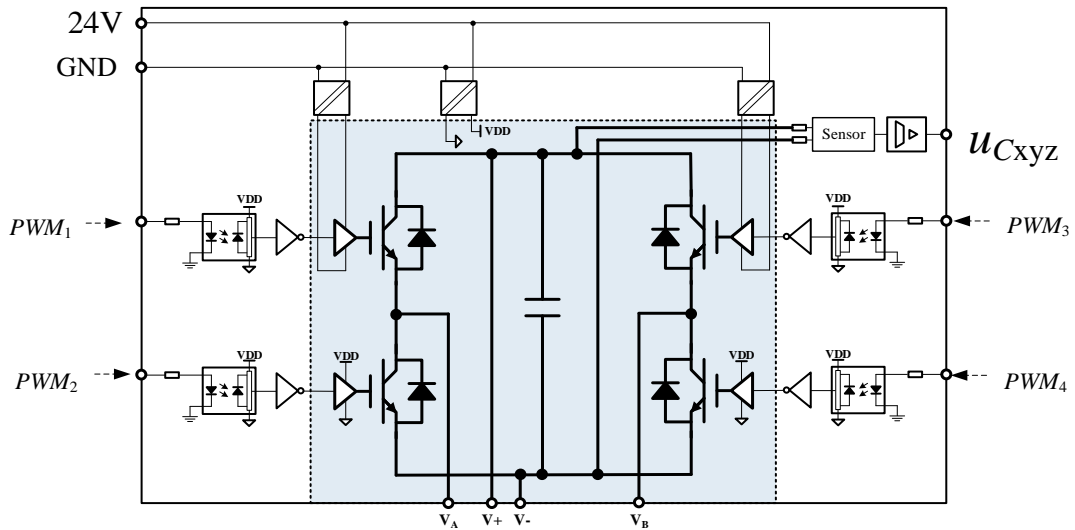


Figure 7.14 Schematic of the full-bridge SM in M³C

In order to avoid the complexity introduced by using a large number of power devices, the dual-in-line package intelligent power module (DIPIPM): Mitsubishi Electrical PSS15S92F6 is chosen in this platform as shown in Figure 7.15.

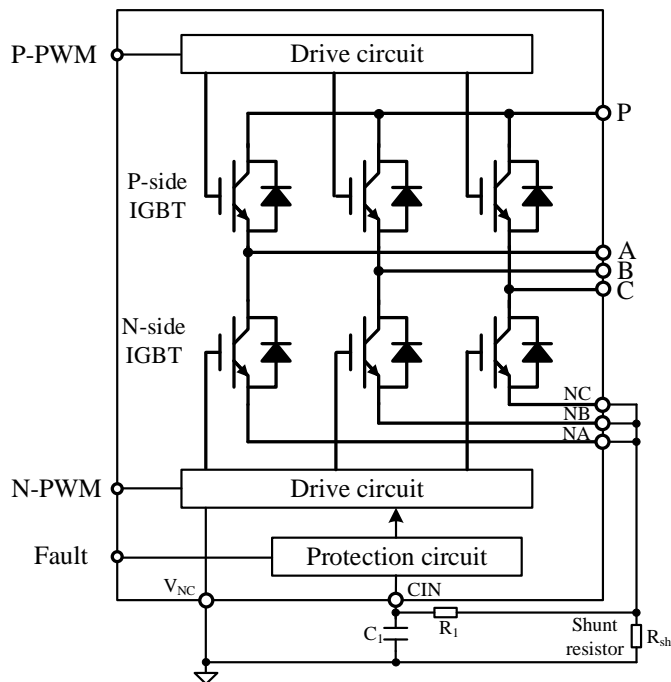


Figure 7.15 Inner schematic and peripheral circuit of DIPIPM

The DIIPM integrates the power chips, drive circuit, protection circuit and temperature output as illustrated in Figure 7.15. The voltage rating of this IGBT module is 600V and the maximum current is 15A which satisfies the requirements of the system. The 350V electrolytic capacitor is chosen for the desired 250V dc-link which then satisfies the desired input and output voltage rating. There are two advantages of using this power module. Firstly, it is a six-in-one module whose structure is depicted in Figure 7.15. Four out of the six IGBTs have been used and its circuit design is much simpler when compared with the isolated IGBT scheme. Another advantage of this power module is the short-circuit (SC) protection function through the shunt resistor. After comparing the feedback voltage from the shunt resistor and the SC protection voltage the integrated control circuit captures the maximum current and activates the protection mechanism automatically.

The appropriate shunt resistance is selected according to the typical SC action threshold voltage reference value $U_{sc}^*=0.48V$. The maximum value of the SC protection current should be the saturated current of the IGBT which is the 1.7 times the rated current. Therefore:

$$I_{SC(max)} = 15A \times 1.7 = 25.5A \quad (7.1)$$

where, $I_{SC(max)}$ is the maximum value of the SC protection current.

In terms of the design of the protection circuit, the value of the shunt resistance should be considered. According to the datasheet:

$$\begin{cases} U_{SC(min)} = 0.455V \\ U_{SC(typ)} = 0.48V \\ U_{SC(max)} = 0.505V \end{cases} \quad (7.2)$$

where, $U_{SC(max)}$, $U_{SC(typ)}$ and $U_{SC(min)}$ are the maximum, typical and minimum values respectively of the SC action threshold voltage.

Therefore, the minimum value of the shunt resistance $R_{sh(min)}$ is calculated as:

$$R_{sh(min)} = \frac{U_{SC(max)}}{I_{SC(max)}} = \frac{0.505V}{25.5A} = 19.8m\Omega \quad (7.3)$$

Usually the accuracy of a resistor is considered as $\pm 5\%$ to obtain the accurate value of the current. Hence:

$$\begin{cases} R_{sh(typ)} = \frac{R_{sh(min)}}{0.95} = \frac{19.8m\Omega}{0.95} = 20.8m\Omega \\ R_{sh(max)} = R_{sh(typ)} \cdot 1.05 = 20.84 \cdot 1.05 = 21.9m\Omega \end{cases} \quad (7.4)$$

Since there are no available resistors with these values, resistors of 40mΩ and 43mΩ are selected and connected in parallel to get the desired resistance 20.8mΩ.

When the SC protection acts the N-side IGBT will be blocked and the fault signal will be generated. In order to avoid a mistaken action caused by switching noise or reverse current, a RC filter is required at the CIN pin. The C_1 is chose as 1nF while R_1 is equal to 2kΩ. When the fault signal is generated by the DIPIM, the signal transfers to the DSP in order to identify the fault module. The optocoupler EL817 functions as isolation, and the PNP triode is utilized to amplify this signal. The feedback circuit is presented in Figure 7.16.

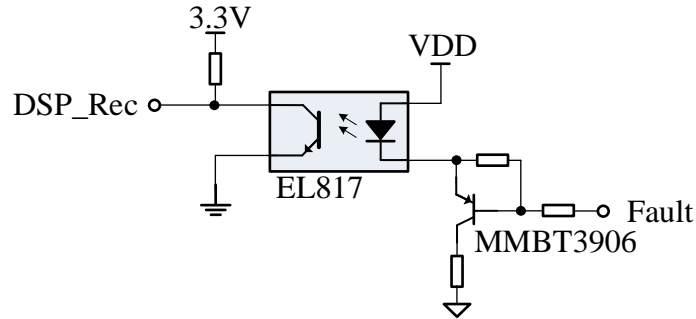


Figure 7.16 Feedback circuit of the fault signal

The variables in each arm that needs to be sampled are the three capacitor voltages and the arm current. Since the DSP integrates the A/D converter, only an extra sensor and the processing circuit are required. To reduce the number of auxiliary power supplies, the single-supply sensor is adopted, where the voltage sensor is HBV05-A5. The relationship between the input current and output voltage of this sensor is shown in Figure 7.17.

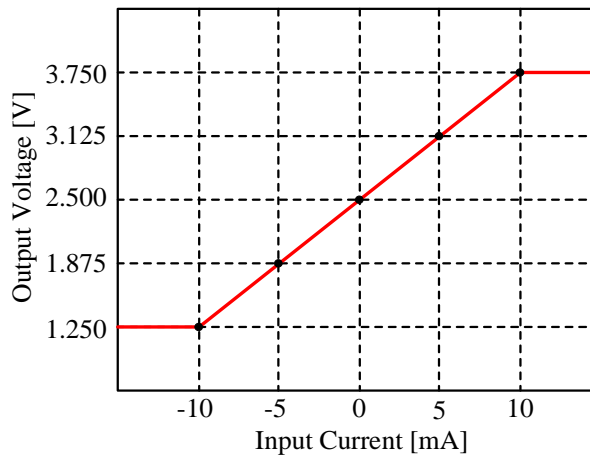


Figure 7.17 The relationship between input current and output voltage of hall voltage sensor

The schematic of the sampling and processing circuit of the capacitor voltage is shown in Figure 7.18. The maximum current of the hall sensor is 10mA and the sampling resistance is 20k Ω .

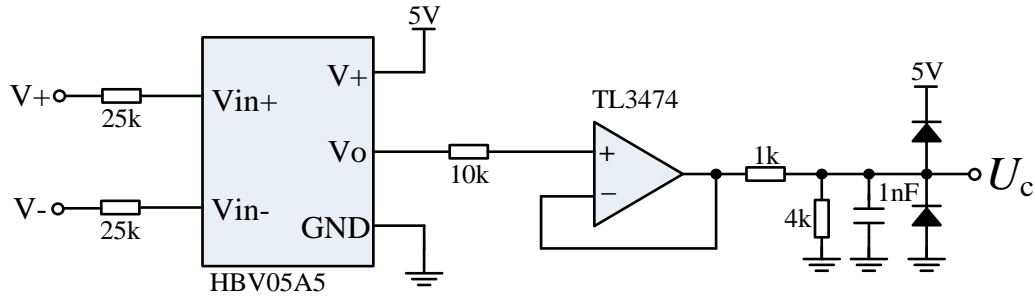


Figure 7.18 Sampling and processing circuit of the capacitor voltage

7.5 Experimental Results

In this section, experimental results of two proposed control methods as discussed in chapter 5 and chapter 6 are presented and analyzed. The experimental parameters is shown in Table 7.1.

Table 7.1 Experimental parameters of the proposed control methods

Description	Parameters	Value
Rated active power	P	0.63 kW
Input phase RMS voltage	E_i	60 V
Input frequency	f_i	50 Hz
Input inductance	L_i	1 mH
Output phase RMS voltage	E_o	56 V
Output frequency	f_o	16.7 Hz
Switching frequency	f_s	4kHz
Output inductance	L_o	1 mH
Capacitance of SM's capacitor	C_{xyz}	1 mF
Rated dc capacitor voltage	U_{Cxyz}^*	70 V
Arm inductance	L	4 mH
Load Resistance	R_o	16 Ω
Number of SMs per arm	n	3

7.5.1 The design of the pre-charge and soft-start process of the prototype

If the prototype is started directly, the capacitor voltage control loop will be instantaneously saturated which creates an instantaneous inrush current to the input side and is very harmful to the device in the prototype. Therefore, it is necessary to design the system's pre-charge and soft-start strategies. The pre-charge process is now designed and discussed in further details.

(1) Uncontrolled rectifier stage. All PWM signals are disabled and each arm is regarded as a series connected uncontrolled rectifier. In order to prevent the inrush current, a current limiting resistor is added to the input side as shown in Figure 7.19. At the uncontrolled rectifier stage, there is no current flowing through the load which can be considered as a short-circuited situation. For example, when $e_A > e_C > e_B$, the charging current loop is shown in Figure 7.19. Assuming the effective value of the input three-phase voltage is e_i , then:

$$e_A - e_B = \sqrt{2}e_i \sin(\omega t) - \sqrt{2}e_i \sin(\omega t - \frac{2\pi}{3}) = \sqrt{6}e_i \cos(\omega t - \frac{\pi}{3}) \quad (7.5)$$

The maximum value of the right hand side of Equation (7.5) is $\sqrt{6}e_i$. Since there are six series connected SMs in these two sub-converters, the maximum capacitor voltage for each capacitor that could be charged is $e_i/\sqrt{6}$.

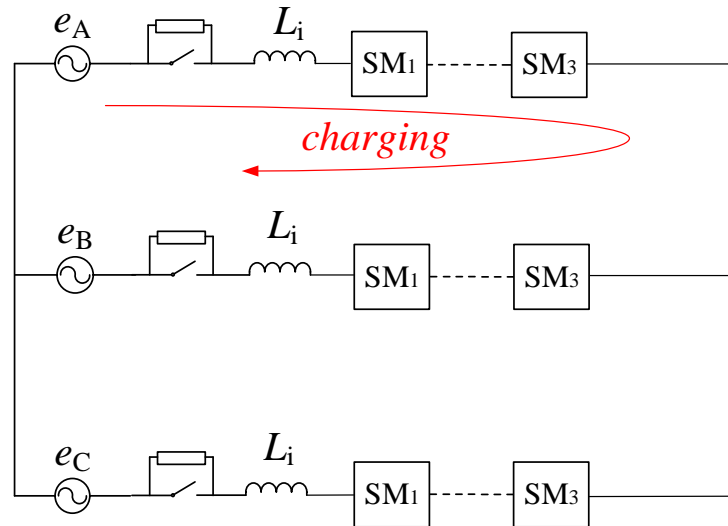


Figure 7.19 An example current flow path at the uncontrolled rectifier stage

(2) Function as the controlled rectifier. The PWM signal is enabled which means the prototype operates in the rectifier state. Unlike the normal operation state, the output side voltage is controlled as zero. Only the input side of the prototype is being controlled, and the capacitor

voltage is controlled as the ramp as shown in Figure 7.20.

- (3) Soft-start. When the output voltage is being uncontrolled it might increase too fast and this will cause the system to stop working properly. Therefore, the output voltage needs to be controlled and increased slowly during the soft-start operation.

The experimental results of the pre-charge and soft-start process are shown in Figure 7.20. When $t=0$ s, the current limiting resistors are connected into the circuit which means the pre-charging process of the prototype starts. When $t_1=0.15$ s, the power supply of the prototype is switched on. M^3C is working in the uncontrolled rectifier state. From $t_2=0.4$ s to $t_3=1.3$ s, the capacitor voltage is being charged to the rated value. Then, the output voltage control of the prototype is soft started as discussed previously. When $t_4=3.5$ s, the output voltage is being controlled at the rated value. Finally, the system is working in the steady state.

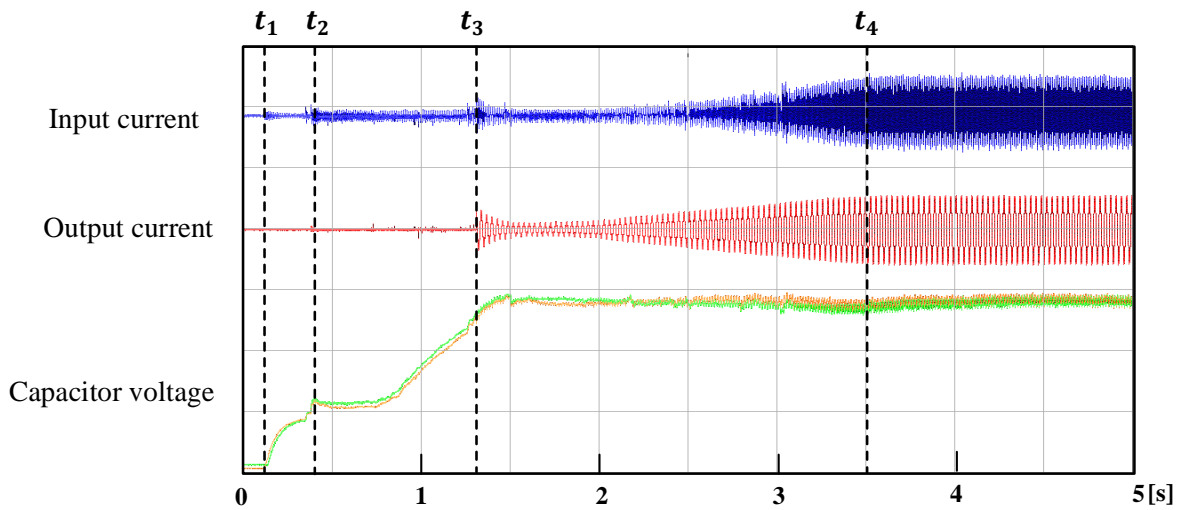


Figure 7.20 Experimental results of the pre-charge and soft-start process

7.5.2 The experimental results of the Hierarchical Energy Balance Control Method for M^3C based on Injecting Output Frequency Circulating Currents

Case I: Steady-state operation

Figure 7.21 shows the experimental results of M^3C under steady-state operation condition. Specifically, Figure 7.21(b) shows the input current is in-phase with the input voltage, which demonstrates the unity power factor operation achieved by the proposed control method. The

output current has been controlled well with the desired low frequency of 16.7 Hz as can be seen from Figure 7.21(d). As expected, the arm current contains two frequency components, which is experimentally shown in Figure 7.21(c). Once again, the circulating current has no effect on either the input or the output currents as demonstrated experimentally in Figure 7.21(b), (c) and (d). Three capacitor voltages are presented in Figure 7.21(e) where the zoomed figure shows the voltage fluctuates by only ± 2 V ($\pm 2.9\%$) from the desired voltage of 70V, which again confirms the effectiveness of the proposed control technique. Finally, the output voltage of arm_{Aa} is shown in Figure 7.21(f).

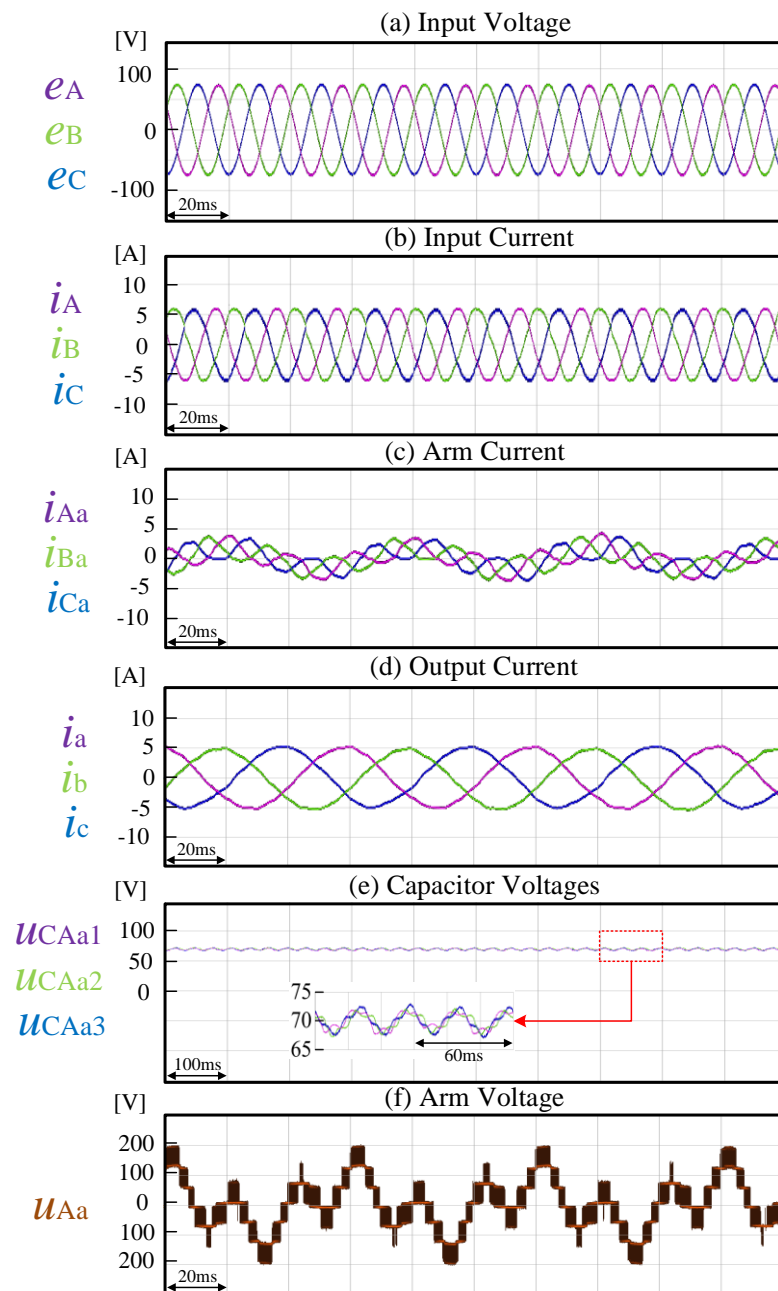


Figure 7.21 Experimental results under steady-state operation

Figure 7.22 below shows the simulated arm current, where the input frequency to M³C is 16.7 Hz and the output frequency is 50 Hz. As it can be seen from spectrum illustrated in Figure 7.22(b), the arm current contains these two frequency components. Similarly, when the input frequency is 50Hz and the output frequency is 16.7 Hz, again the FFT analysis of the arm current in Figure 7.23(b) shows the same components i.e. 50 Hz and 16.7 Hz. Therefore, although the shape of the arm current is different in the two cases, however, it contains the same components that are depend on the input and output frequencies.

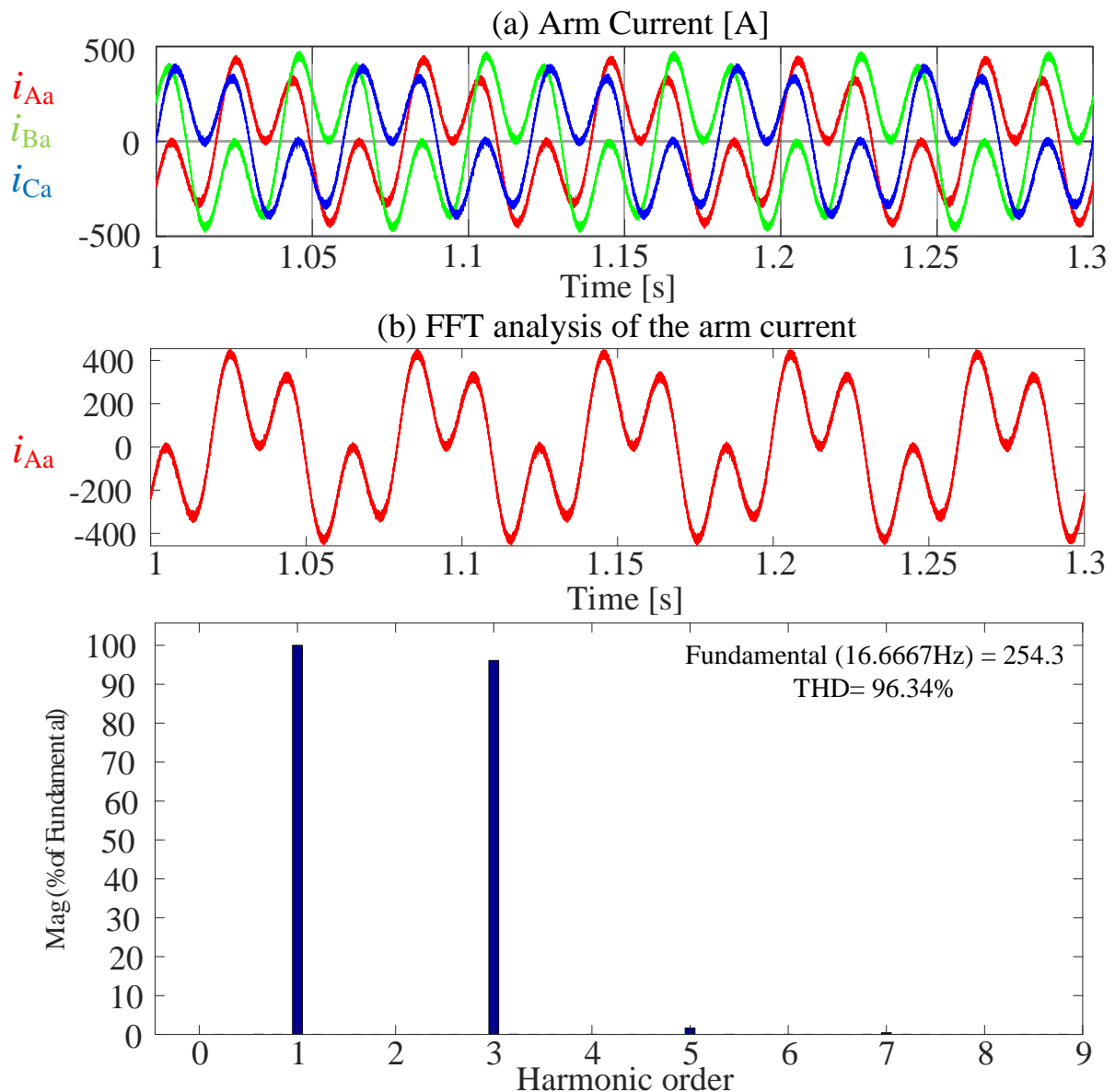


Figure 7.22 The simulation results of arm current and the corresponding FFT analysis

when $f_i=16.7$ Hz and $f_o=50$ Hz

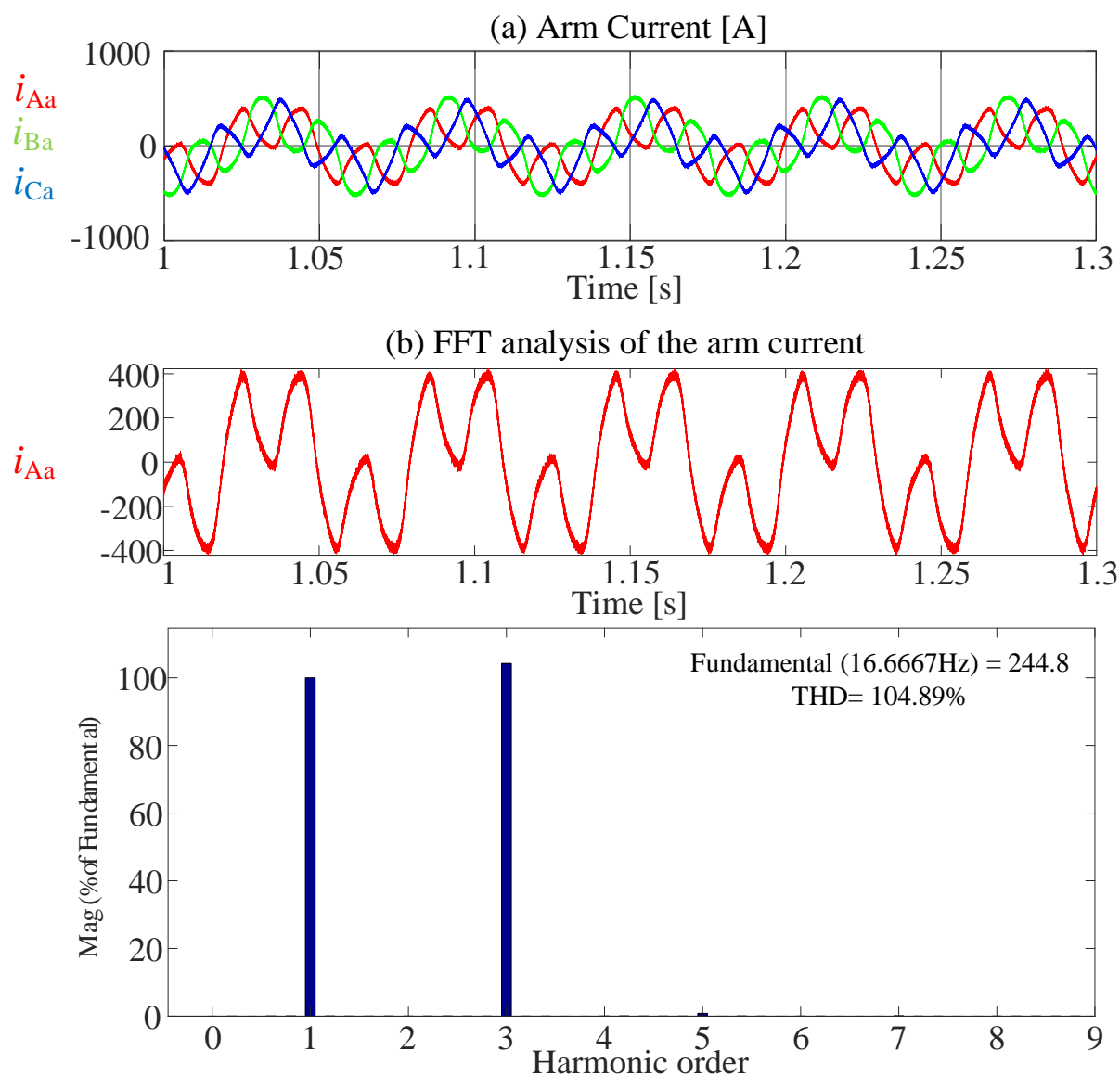


Figure 7.23 The simulation results of arm current and the corresponding FFT analysis

when $f_i=50$ Hz and $f_o=16.7$ Hz

The emphasis of this work is to use M^3C as a frequency changer between the offshore and onshore grids to facilitate the adoption of LFAC transmission system. Furthermore, the proposed M^3C in this paper is intended to be at onshore, where the input frequency is 16.7 Hz and the output is 50 Hz to matched to electricity network. However, due to the unavailability of low frequency (16.7 Hz) programmable AC source in the lab, the output side is connected to the passive load with 16.7Hz to demonstrate the capability of the proposed converter in changing the frequency. Therefore, the scenario of the experiments is different from the simulations, but it can be regarded as a supplement to the simulation results which further validates the effectiveness of the proposed methods experimentally.

In order to give a better explanation and presentation, Figure 7.24 shows the simulation results (when $f_i=50$ Hz and $f_o=16.7$ Hz) of the proposed control method in chapter 5 under steady-state condition which is a perfect match to the experimental results.

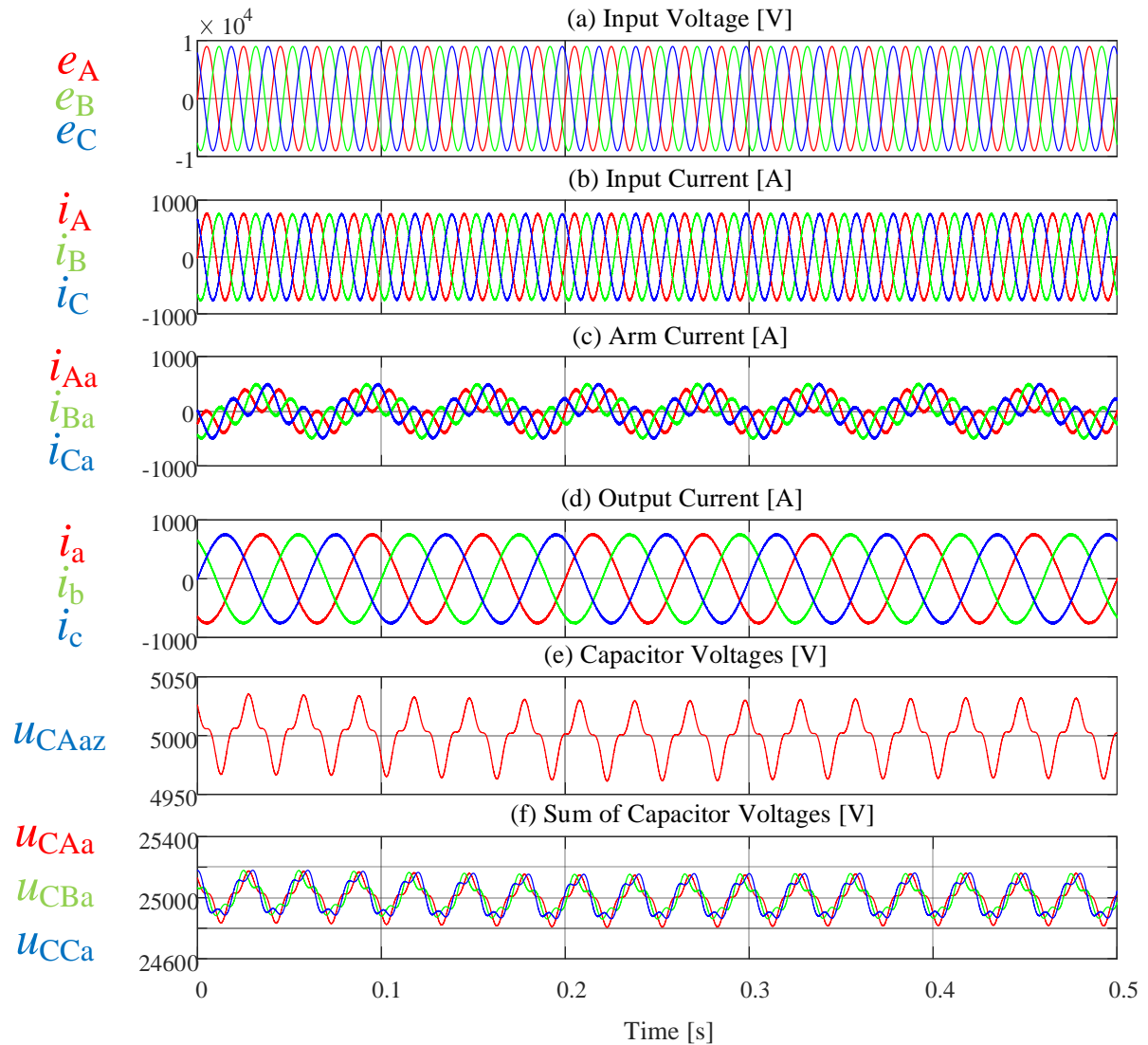


Figure 7.24 Simulation results of the proposed control method when $f_i=50$ Hz and $f_o=16.7$ Hz

Case II: Dynamic output frequency operation

Furthermore, the performance of the proposed system is experimentally validated with two step change operating conditions. Figure 7.25 illustrates the step change in the output frequency, i.e. 16.7 Hz to 5 Hz. The lower the output frequency the higher ac voltage ripple of the capacitor voltage. This test aims to demonstrate the performance of the proposed control technique with a very low output frequency. However, the measured capacitor voltages shows only ± 5 V

($\pm 7.1\%$) variation from the 70 V reference voltage as shown in Figure 7.25(d), which again proves the robustness of the control method.

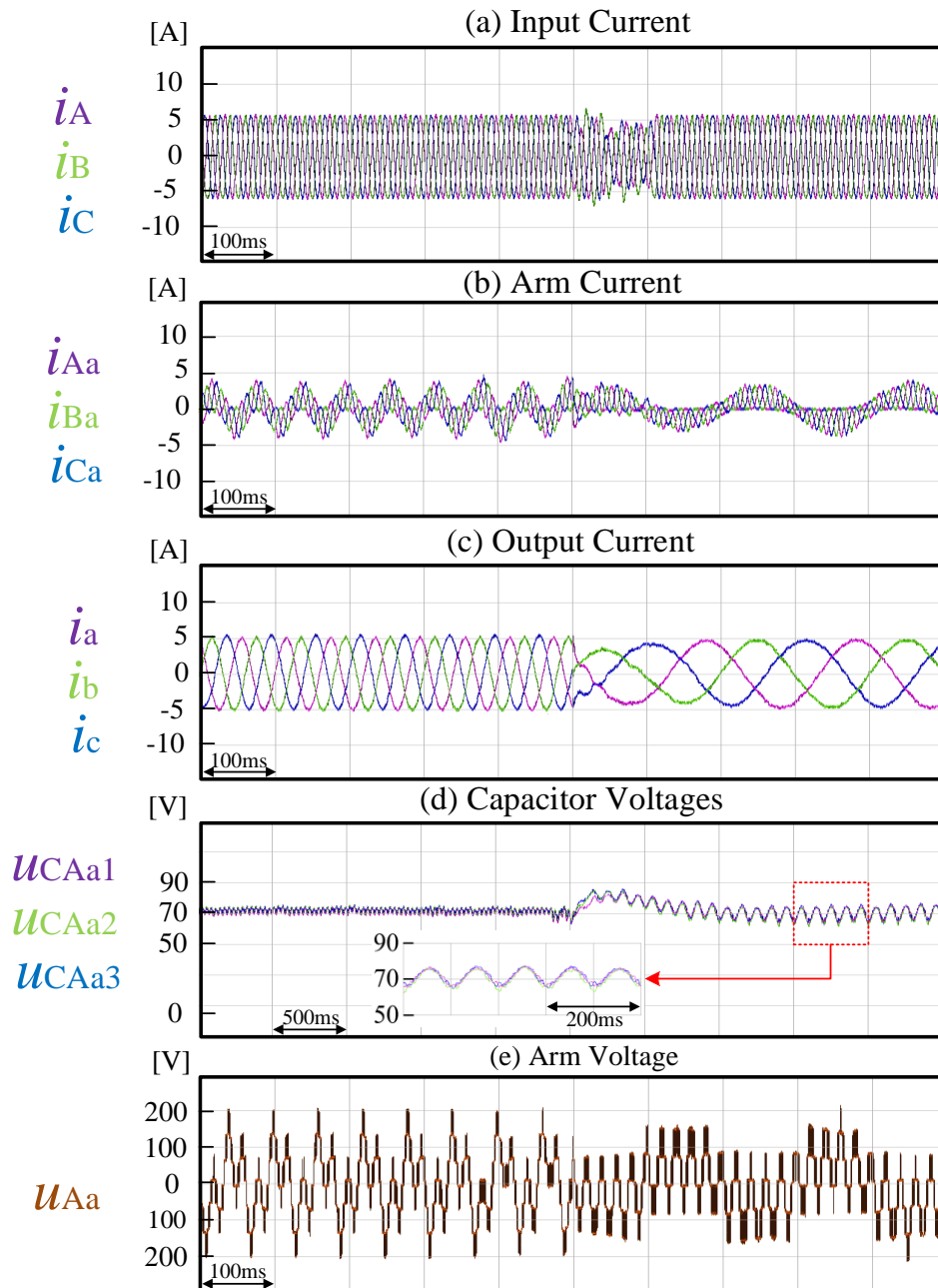


Figure 7.25 Experimental results under output frequency step change operation

Case III: Dynamic output voltage operation

Step change in the output voltage is also demonstrated experimentally, where the voltage changed from 43 V to 56 V as portrayed in Figure 7.26. As the demand on the output side increased as shown in Figure 7.26(c), the input current increases accordingly as depicted in Figure 7.26(a). Three capacitor voltages damped for compensating the increasing power

demand from the output side, but well balanced at 70 V.

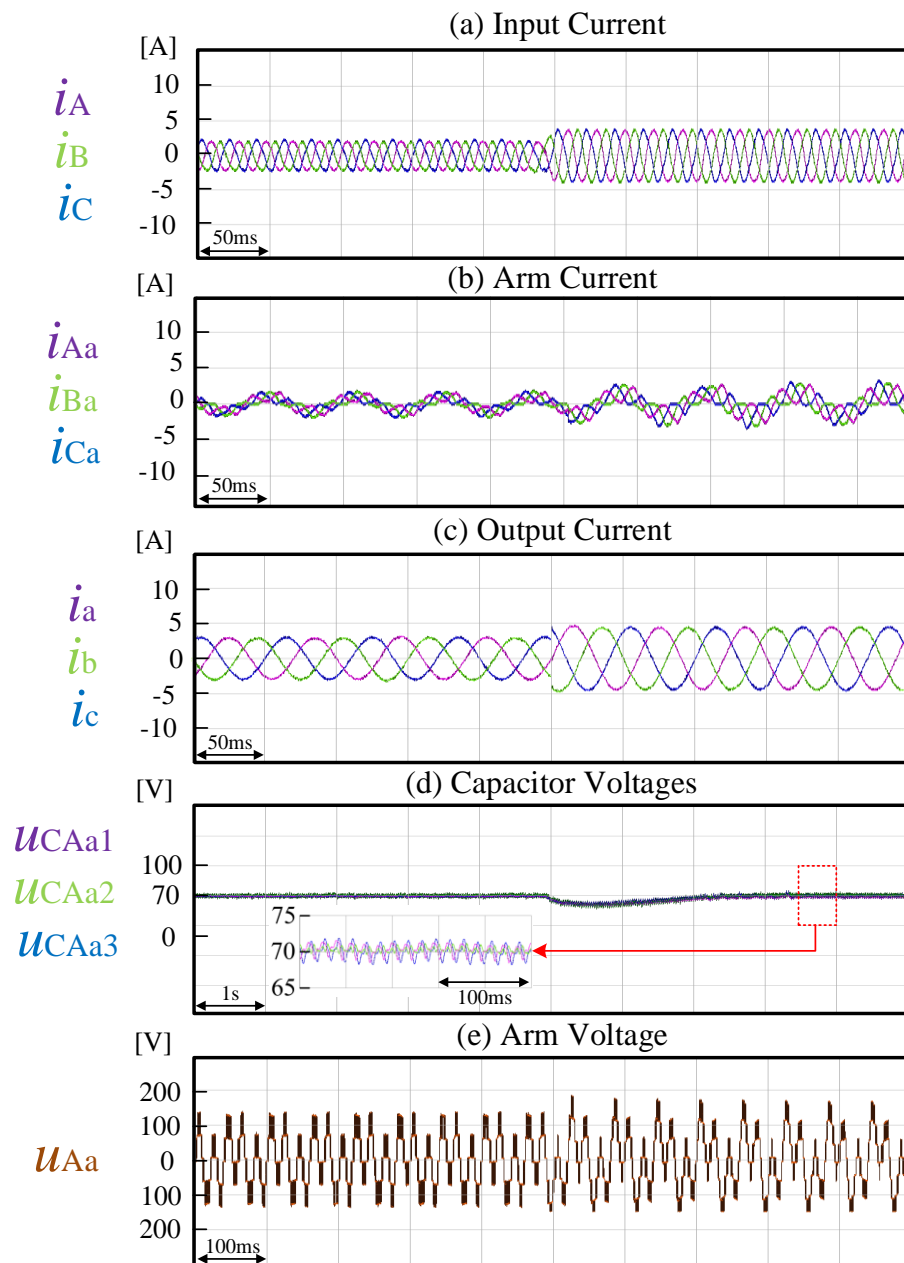


Figure 7.26 Experimental results under output voltage step change operation

7.5.3 The experimental results of the Hierarchical Energy Balance Control Method for M^3C based on Injecting Two Frequency Circulating Currents

Case I: Steady-state operation

Experiment results of the overall energy balance control method under steady-state operation condition are presented in Figure 7.27. First of all, Figure 7.27(b) shows the input current is in-

phase with the input voltage, which again demonstrates the unity power factor operation. As the circulating current control balances the energy between sub-converters, three capacitor voltages in Figure 7.27(e) shows the voltage fluctuates by only ± 2 V ($\pm 2.9\%$) from the desired voltage of 70 V, which again confirms the effectiveness of the proposed control technique. Finally, the output voltage of arm_{Aa} is shown in Figure 7.27(f).

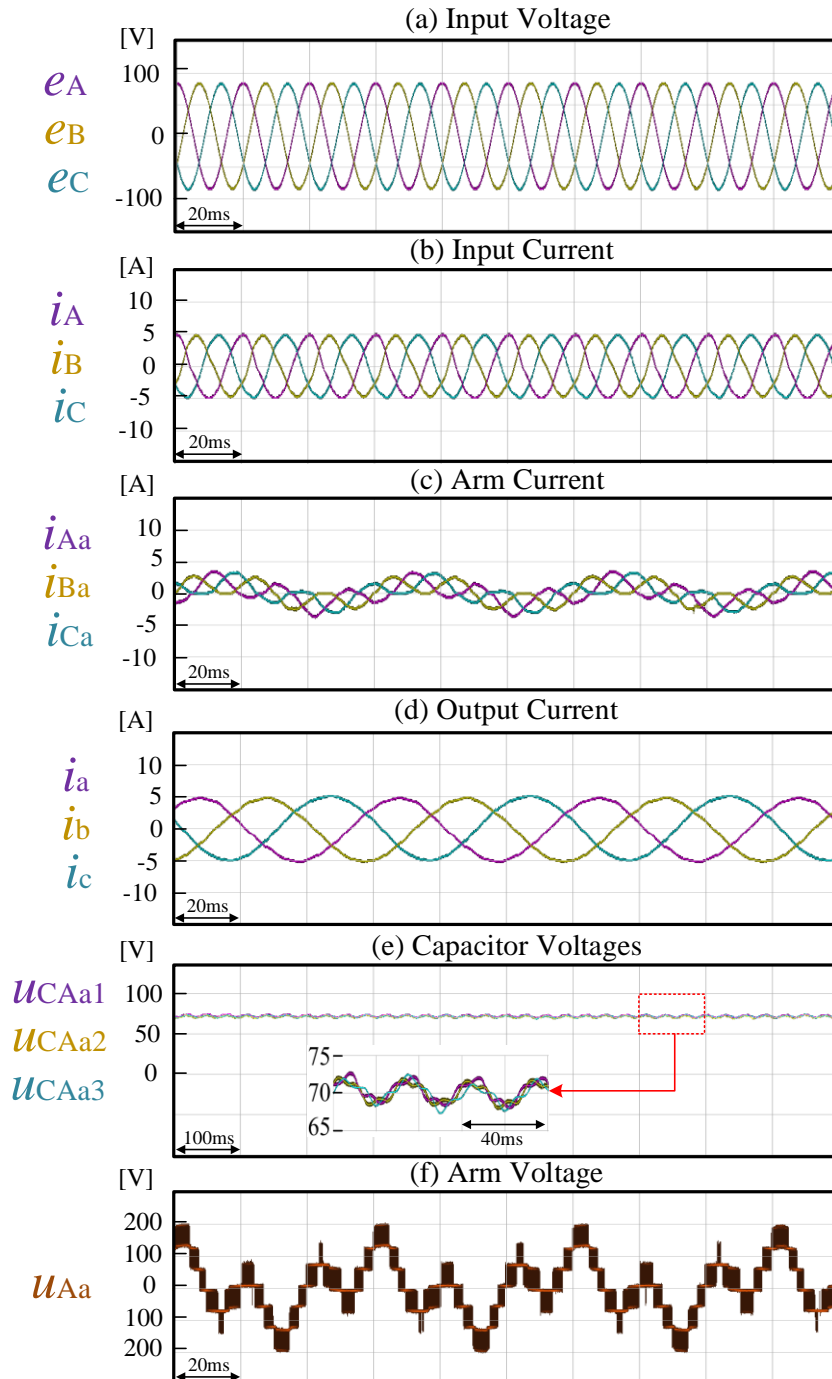


Figure 7.27 Experimental results under steady-state operation

Case II: Dynamic output frequency operation

In order to have a better observation between two proposed control methods, the performance of the proposed system is also experimentally validated with two step change operating conditions. Figure 7.28 illustrates the step change in the output frequency from 16.7 Hz to 5 Hz. The measured capacitor voltages shows only ± 5 V ($\pm 7.1\%$) variation from the 70V reference voltage as shown in Figure 7.28(d). Compared with the capacitor voltages in Figure 7.25(d), the performance is very similar which again proves the robustness of the control method.

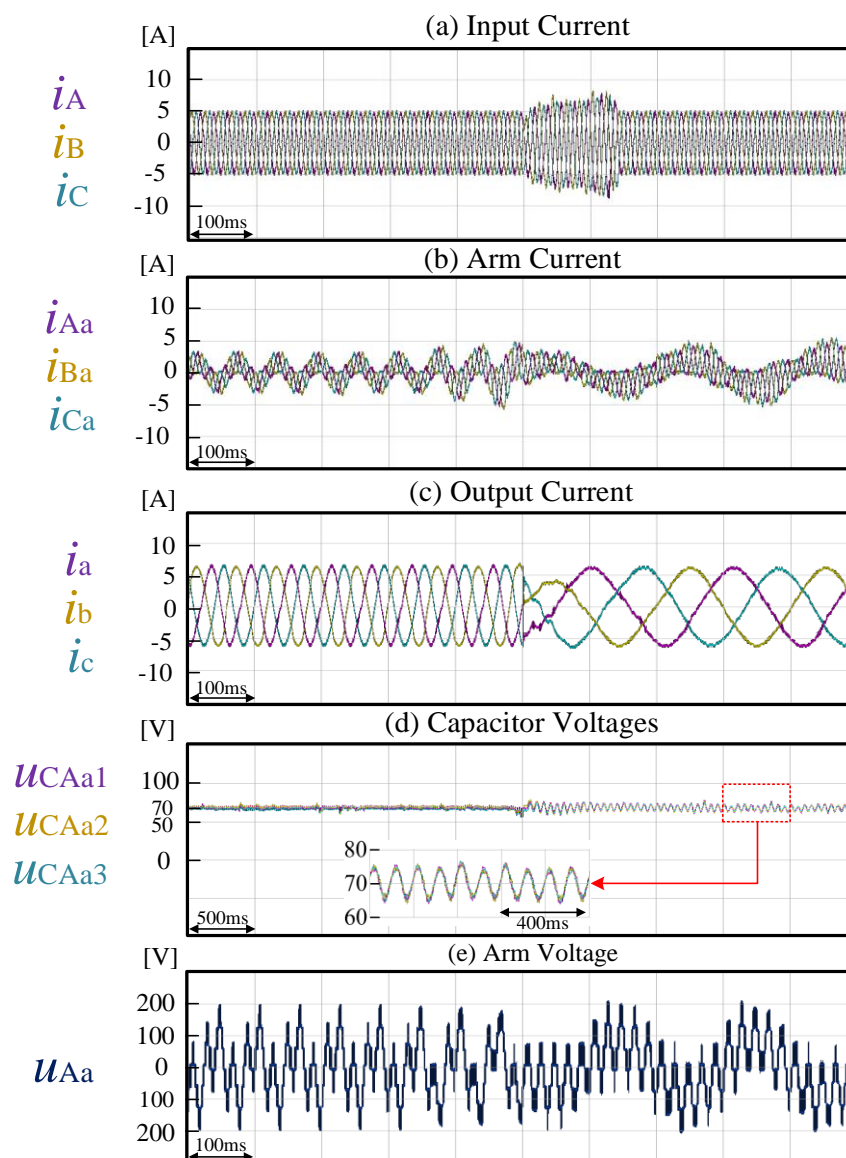


Figure 7.28 Experimental results under output frequency step change operation

Case III: Dynamic output voltage operation

Experiment results of the step change in the output voltage is demonstrated where the voltage changed from 43 V to 56 V as portrayed in Figure 7.29. As the demand on the output side increased as shown in Figure 7.29(c), the input current increases accordingly as depicted in Figure 7.29(a). Three capacitor voltages damped for compensating the increasing power demand from the output side, but well balanced at 70 V. Obviously, the performance compared with the Figure 7.26 is very similar which also effectively proved the performance of the proposed control methods.

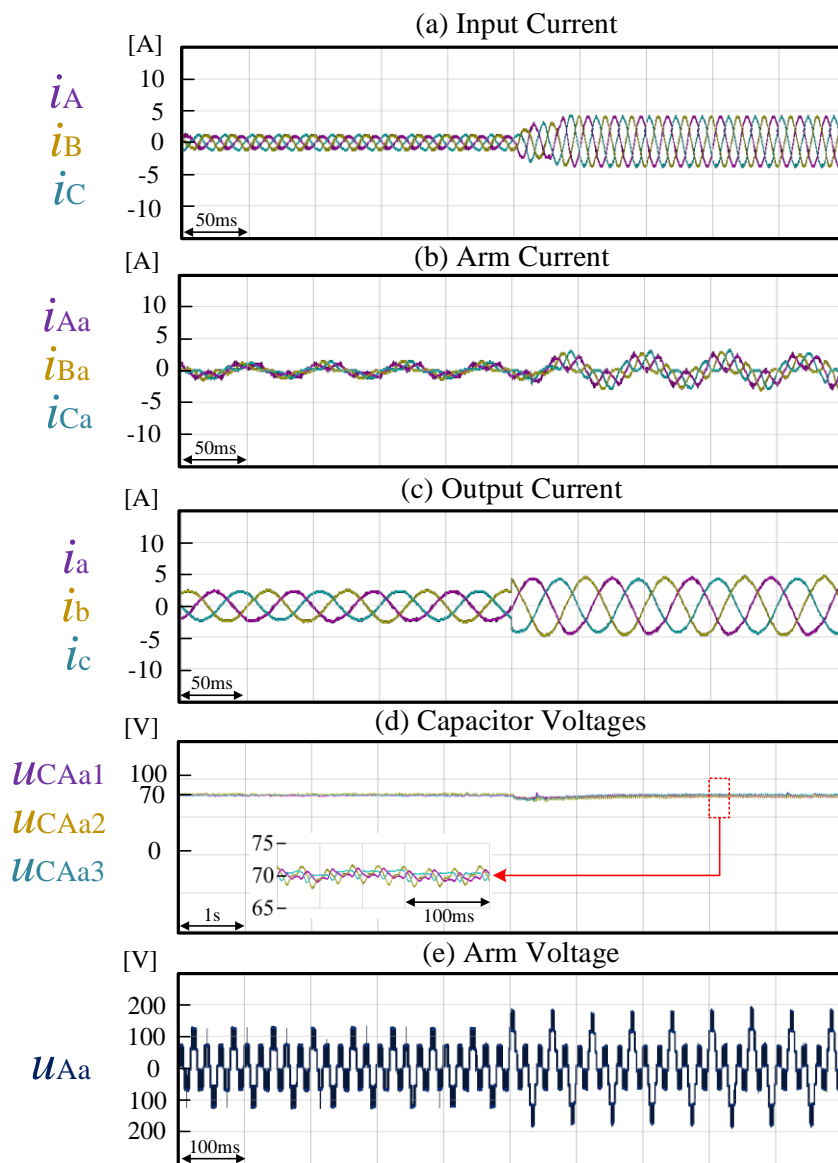


Figure 7.29 Experimental results under output voltage step change operation

7.6 Summary

The proposed control methods are designed as each sub-converter controlled independently while one sub-converter's control could be equally applied to the other sub-converters of M³C. The distributed control network has been applied to a small laboratory prototype for taking full advantages of flexibility and scalability of the proposed control methods of M³C. The design of the distributed control architecture distributed the real-time current loop to each arm controller which eased the communication burden and greatly reduced the negative impact of the communication delay. The similar experiment results under various conditions prove the effectiveness of the two proposed control methods and the perfect match compared with the simulation results.

Chapter 8 Conclusions and Future Work

8.1 Conclusions

In Chapter 3, the mathematical model of M³C quantify the relationship between the arm power and capacitor voltage which is the fundamental of capacitor voltage balancing control. Although there are two frequency components in the arm current, the frequency analysis presents that there are four frequency components in the arm power and the capacitor voltage. It identified the relationship between the capacitor voltage ripple and the input/output frequency ratio: 1) when the output frequency is being decreased, the capacitor voltage ripple in the frequency components $2\omega_o$ is increasing which will unbalance the system; 2) when the output frequency is close to the input frequency, the capacitor voltage ripple in the frequency components $\omega_i\omega_o$ is increasing which will unbalance the system. However, as the background of this thesis is M³C functioning as the frequency changer for the LFAC transmission system, the input frequency/output frequency ratio is fixed at 1/3. But this chapter provides the fundamental analysis and mathematical model for the future work.

In Chapter 4, the commonly used control method ‘double $\alpha\beta 0$ transformation’ control method has been studied and presented. The mathematical model of M³C is developed based on the $\alpha\beta 0$ frame to decouple the input current, output current and circulating current. The arm power analysis based on $\alpha\beta 0$ frame gives nine arm power components to control the overall capacitor voltage balance and the capacitor voltage between nine arms. According to its mathematical relationship between the arm power and capacitor voltage, the frequency of circulating currents are randomly selected from either input frequency or the output frequency. Simulation results under different conditions proved its performance. However, as discussed in Chapter 4, several times of $\alpha\beta 0$ transformation brings the massive mathematical calculation and greatly increase the control complexity.

In Chapter 5, the proposed control method achieved the fully independent control of each sub-converter. The injection of output frequency circulating current has been designed easily and accurately for the purpose of compensating the energy difference between the three arms of the

sub-converter. The selective voltage mapping modulation technique is designed that balances the energy between n sub-modules within each arm. The experimental results from a scaled down laboratory prototype proved the performance of the proposed control method under steady-state and different dynamic operating conditions.

In Chapter 6, an improved energy balance control method with injecting both input and output frequency circulating currents is proposed. The M³C is divided into six sub-converters and each sub-converter is controlled independently. The input and output frequency circulating current balanced the capacitor voltage between nine arms within six sub-converters. The magnitudes of the circulating current responsible for the energy balance control in either frequency are half reduced as compared to the single frequency injection method in Chapter 5. This arrangement alleviates the negative impact of the injected circulating current on the external grid and allows the M³C systems work through larger grid unbalance situations.

In Chapter 7, the three phase-to-three phase M³C experimental platform is validated to test the performance of the proposed control methods. As M³C has the advantages of flexibility and scalability, the platform is designed as the distributed control network which contains ten controllers (TMS320F2837xS) with one master controller for M³C's system control and one arm controller for each arm. As the emphasis of this work is to use M³C as a frequency changer between the offshore and onshore grids to facilitate the adoption of LFAC transmission system and the proposed M³C in this thesis is intended to be at onshore, where the input frequency is 16.7 Hz and the output is 50 Hz to matched to electricity network. However, due to the unavailability of low frequency (16.7 Hz) programmable AC source in the lab, the output side is connected to the passive load with 16.7 Hz to demonstrate the capability of the proposed converter in changing the frequency. Therefore, the scenario of the experiments is different from the simulations, but it can be regarded as a supplement to the simulation results which further validates the effectiveness of the proposed methods experimentally.

8.2 Future work

The research on the subject of the offshore wind power transmission system has far-reaching significance and it still has a long way to go. This thesis has carried out the research on several

key issues such as control strategies and modulation technology of M^3C -LFAC which have achieved some results. However, the author believes that there are still some problems that need further research:

- The fault diagnosis of M^3C . The high-voltage and high-capacity industrial projects require a large number of sub-modules in M^3C . Once the failure occurs in a sub-module, if it is not detected and removed in time, it may affect the operation of the entire converter. Therefore, the real-time fault diagnosis is needed to achieve the accurate detection of fault.
- The control of M^3C under the three-phase unbalanced condition. The control capability of M^3C under the three-phase unbalance condition is essential to meet the requirements which can handle the risk from the grid. The effective number of degrees of freedom is not enough, therefore the control strategy should be different in terms of different control objectives.

Reference

- [1] Y. Zhou, D. E. Macpherson, W. Blewitt, and D. Jovcic, "Comparison of DC-DC converter topologies for offshore wind-farm application," in *Power Electronics, Machines and Drives (PEMD 2012), 6th IET International Conference on*, 2012, pp. 1-6.
- [2] S. Liu, X. Wang, L. Ning, B. Wang, M. Lu, and C. Shao, "Integrating offshore wind power via fractional frequency transmission system," in *IEEE Transactions on Power Delivery*, vol. 32, no. 3, pp. 1253-1261, June 2017.
- [3] X. Wang and X. Wang, "Feasibility study of fractional frequency transmission system," in *IEEE Transactions on Power Systems*, vol. 11, no. 2, pp. 962-967, May 1996.
- [4] W. Fischer, R. Braun and I. Erlich, "Low frequency high voltage offshore grid for transmission of renewable power," *2012 3rd IEEE PES Innovative Smart Grid Technologies Europe (ISGT Europe)*, Berlin, 2012, pp. 1-6.
- [5] W. Kawamura, M. Hagiwara and H. Akagi, "Control and Experiment of a Modular Multilevel Cascade Converter Based on Triple-Star Cells," in *IEEE Transactions on Industry Applications*, vol. 50, no. 5, pp. 3536-3548, Sept.-Oct. 2014.
- [6] S. Liu, X. Wang, Y. Meng, P. Sun, H. Luo and B. Wang, "A Decoupled Control Strategy of Modular Multilevel Matrix Converter for Fractional Frequency Transmission System," in *IEEE Transactions on Power Delivery*, vol. 32, no. 4, pp. 2111-2121, Aug. 2017.
- [7] B. Fan, K. Wang, P. Wheeler, C. Gu and Y. Li, "A Branch Current Reallocation Based Energy Balancing Strategy for the Modular Multilevel Matrix Converter Operating Around Equal Frequency," in *IEEE Transactions on Power Electronics*, vol. 33, no. 2, pp. 1105-1117, Feb. 2018.
- [8] D. Karwatzki and A. Mertens, "Generalized Control Approach for a Class of Modular Multilevel Converter Topologies," in *IEEE Transactions on Power Electronics*, vol. 33, no. 4, pp. 2888-2900, April 2018.
- [9] T. Nakamori, M. A. Sayed, Y. Hayashi, T. Takeshita, S. Hamada and K. Hirao, "Independent Control of Input Current, Output Voltage, and Capacitor Voltage Balancing for a Modular Matrix Converter," in *IEEE Transactions on Industry Applications*, vol. 51,

- no. 6, pp. 4623-4633, Nov.-Dec. 2015.
- [10] D. Lu, S. Wang, J. Yao, T. Yang and H. Hu, "Cluster Voltage Regulation Strategy to Eliminate Negative Sequence Currents under Unbalanced Grid for Star-Connected Cascaded H-Bridge STATCOM," in *IEEE Transactions on Power Electronics*.
- [11] A. Mora, M. Espinoza, M. Díaz and R. Cárdenas, "Model Predictive Control of Modular Multilevel Matrix Converter," *2015 IEEE 24th International Symposium on Industrial Electronics (ISIE)*, Buzios, 2015, pp. 1074-1079.
- [12] S. Rodrigues et al. "A Multi-Objective Optimization Framework for Offshore Wind Farm Layouts and Electric Infrastructures," *Energies* 9.3(2016):216.
- [13] O. Anaya-Lara et al, "Wind Energy Generation Modeling and Control", 1st ed. Chichester, U.K.: Wiley, 2009.
- [14] T. Funaki and K. Matsuura, "Feasibility of the low frequency AC transmission," *2000 IEEE Power Engineering Society Winter Meeting. Conference Proceedings (Cat. No.00CH37077)*, Singapore, 2000, pp. 2693-2698 vol.4.
- [15] K. H. Sobrink, D. Woodford, R. Belhomme, and E. Joncquel (2003), "A.C. cable v D.C. cable transmission for offshore wind farms, a study case," presented at *the 4th International Workshop on Largescale Integration of Wind Power and Transmission Networks for Offshore Wind Farms*, Billund, Denmark.
- [16] P. Bresesti, W. L. Kling, R. L. Hendriks and R. Vailati, "HVDC Connection of Offshore Wind Farms to the Transmission System," in *IEEE Transactions on Energy Conversion*, vol. 22, no. 1, pp. 37-43, March 2007.
- [17] SKM, Review of Worldwide Experience of Voltage Source Converter (VSC) High Voltage Direct Current Technology (HVDC) Installations, 2013 (Online).
- [18] K. Friedrich, "Modern HVDC PLUS application of VSC in Modular Multilevel Converter topology," *2010 IEEE International Symposium on Industrial Electronics*, Bari, 2010, pp. 3807-3810.
- [19] B. Jacobson, P. Karlsson, G. Asplund, L. Harnefors, T. Jonsson, "VSC-HVDC transmission with cascaded two-level converters," in *CIGRÉ SC B4 Session*, 2010.
- [20] J. Glasdam, "Harmonics in Offshore Wind Power Plants," Springer International

- Publishing, 2016.
- [21] T. Takeda et al., "Space charge behavior in full-size 250 kV DC XLPE cables," in *IEEE Transactions on Power Delivery*, vol.13, pp. 28-39, 1998.
- [22] M. Fu, G. Chen, L. A. Dissado, and J. C. Fothergill, "Influence of thermal treatment and residues on space charge accumulation in XLPE for DC power cable application," *IEEE Transactions on Dielectrics and Electrical Insulation*, vol. 14, pp. 53-64, 2007.
- [23] H. Waje-Andreassen, "Low Frequency AC Transmission-Investigating the Dynamics of an Export Cable for Offshore Wind Power Applications," MS thesis, NTNU, 2016.
- [24] N. Qin, Y. S. Z. Xu and V. Akhmatov, "Offshore Wind Farm Connection with Low Frequency AC Transmission Technology," *2009 IEEE Power & Energy Society General Meeting, Calgary, AB*, 2009, pp. 1-8.
- [25] X. Wang, "The Fractional Frequency Transmission System," in *1994 IEE Japan Power & Energy*, pp. 53-58.
- [26] X. Wang, Y. Teng, L. Ning, Y. Meng and Z. Xu. "Feasibility of integrating large wind farm via Fractional Frequency Transmission System a case study,". *Int Trans Electr Energy Syst 2014*; 24: pp. 64–74.
- [27] T. Schutte, B. Gustavsson, and M. Strom (2001), "The use of low frequency AC for offshore wind power". *Proceedings of the Second International Workshop on Transmission Networks for Offshore Wind Farms (ed T.Ackermann)*, Royal Institute of Technology, Stockholm.
- [28] P. B. Wyllie, Y. Tang, L. Ran, T. Yang, and J. Yu, "Low frequency AC transmission - elements of a design for wind farm connection," in *Proc. 2015 Int. Conf. AC and DC Power Transmission*, 2015.
- [29] J. Ruddy, R. Meere, and T. O'Donnell. "Low Frequency AC transmission for offshore wind power: A review." *Renewable & Sustainable Energy Reviews* 56(2016):75-86.
- [30] X. Wang, C. Cao and Z. Zhou, "Experiment on fractional frequency transmission system," in *IEEE Transactions on Power Systems*, vol. 21, no. 1, pp. 372-377, Feb. 2006.
- [31] H. Chen, M. H. Johnson and D. C. Aliprantis, "Low-Frequency AC Transmission for Offshore Wind Power," in *IEEE Transactions on Power Delivery*, vol. 28, no. 4, pp. 2236-

- 2244, Oct. 2013.
- [32] N. Lianhui, W. Xifan and T. Yufei, "Experiment on wind power integration grid via fractional frequency transmission system: Realization of the variable-speed variable-frequency power wind," *2011 4th International Conference on Electric Utility Deregulation and Restructuring and Power Technologies (DRPT)*, Weihai, Shandong, 2011, pp. 444-449.
- [33] Y. Tang, P. B. Wyllie, J. Yu, X. M. Wang, L. Ran and O. Alatise, "Offshore low frequency AC transmission with back-to-back modular multilevel converter (MMC)," *11th IET International Conference on AC and DC Power Transmission, Birmingham*, 2015, pp. 1-8.
- [34] S. Debnath, J. Qin, B. Bahrani, M. Saeedifard and P. Barbosa, "Operation, Control, and Applications of the Modular Multilevel Converter: A Review," in *IEEE Transactions on Power Electronics*, vol. 30, no. 1, pp. 37-53, Jan. 2015.
- [35] M. A. Perez, S. Bernet, J. Rodriguez, S. Kouro and R. Lizana, "Circuit Topologies, Modeling, Control Schemes, and Applications of Modular Multilevel Converters," in *IEEE Transactions on Power Electronics*, vol. 30, no. 1, pp. 4-17, Jan. 2015.
- [36] B. Wu, "High-Power Converters and AC Drives." *Sirirajmedj Com* (2014).
- [37] S. Kouro et al., "Recent Advances and Industrial Applications of Multilevel Converters," in *IEEE Transactions on Industrial Electronics*, vol. 57, no. 8, pp. 2553-2580, Aug. 2010.
- [38] A. Lesnicar and R. Marquardt, "An innovative modular multilevel converter topology suitable for a wide power range," *2003 IEEE Bologna Power Tech Conference Proceedings*, 2003, pp. 6 pp. Vol.3.
- [39] K. Sharifabadi et al., "Design, Control and Application of Modular Multilevel Converters for HVDC Transmission Systems," 2016.
- [40] S. Du et al., "Modular Multilevel Converters: Analysis, Control and Applications," 2017.
- [41] N. Cherix, "Functional Description and Control Design of Modular Multilevel Converters: Towards Energy Storage Applications for Traction Networks," *Religi3n Y Escuela La Revista Del Profesorado De Religi3n*, 2015.
- [42] R. Zeng, L. Xu, L. Yao and B. W. Williams, "Design and Operation of a Hybrid Modular

- Multilevel Converter," in *IEEE Transactions on Power Electronics*, vol. 30, no. 3, pp. 1137-1146, March 2015.
- [43] R. Marquardt, "A Universal Concept for HVDC-Networks and extended DC-Busapplications," in *Proc. IPEC Conference*, Sapporo, June 2010.
- [44] A. Nami, L. Wang, F. Dijkhuizen, and A. Shukla, "Five level cross connected cell for cascaded converters," *Proceedings of the 2013 15th European Conference on Power Electronics and Applications*, pp. 1–9, 2013.
- [45] J. Qin, M. Saeedifard, A. Rockhill, and R. Zhou, "Hybrid design of modular multilevel converters for HVDC systems based on various submodule circuits," *IEEE Transactions on Power Delivery*, vol. 30, no.1, pp. 385–394, Feb. 2015.
- [46] W. Kawamura, M. Hagiwara and H. Akagi, "Control and Experiment of a Modular Multilevel Cascade Converter Based on Triple-Star Arms," in *IEEE Transactions on Industry Applications*, vol. 50, no. 5, pp. 3536-3548, Sept.-Oct. 2014
- [47] H. Akagi, S. Inoue and T. Yoshii, "Control and Performance of a Transformerless Cascade PWM STATCOM With Star Configuration," in *IEEE Transactions on Industry Applications*, vol. 43, no. 4, pp. 1041-1049, July-aug. 2007.
- [48] H. Akagi, "Classification, Terminology, and Application of the Modular Multilevel Cascade Converter (MMCC)," in *IEEE Transactions on Power Electronics*, vol. 26, no. 11, pp. 3119-3130, Nov. 2011.
- [49] M. Glinka and R. Marquardt, "A new AC/AC multilevel converter family," in *IEEE Transactions on Industrial Electronics*, vol. 52, no. 3, pp. 662-669, June 2005.
- [50] M. Glinka and R. Marquardt, "A new AC/AC-multilevel converter family applied to a single-phase converter," *The Fifth International Conference on Power Electronics and Drive Systems*, 2003. PEDS 2003., 2003, pp. 16-23 Vol.1.
- [51] M. A. Perez, J. Rodriguez, E. J. Fuentes and F. Kammerer, "Predictive Control of AC–AC Modular Multilevel Converters," in *IEEE Transactions on Industrial Electronics*, vol. 59, no. 7, pp. 2832-2839, July 2012.
- [52] F. Kammerer, J. Kolb and M. Braun, "A novel cascaded vector control scheme for the Modular Multilevel Matrix Converter," *IECON 2011 - 37th Annual Conference of the*

-
- IEEE Industrial Electronics Society*, Melbourne, VIC, 2011, pp. 1097-1102.
- [53] Y. Okazaki et al., "Experimental Comparisons Between Modular Multilevel DSCC Inverters and TSBC Converters for Medium-Voltage Motor Drives," in *IEEE Transactions on Power Electronics*, vol. 32, no. 3, pp. 1805-1817, March 2017.
- [54] L. Baruschka and A. Mertens, "A New Three-Phase AC/AC Modular Multilevel Converter With Six Branches in Hexagonal Configuration," in *IEEE Transactions on Industry Applications*, vol. 49, no. 3, pp. 1400-1410, May-June 2013.
- [55] L. Baruschka and A. Mertens, "A new 3-phase AC/AC modular multilevel converter with six branches in hexagonal configuration," *2011 IEEE Energy Conversion Congress and Exposition*, Phoenix, AZ, 2011, pp. 4005-4012.
- [56] J. Kucka, D. Karwatzki and A. Mertens, "Optimised operating range of modular multilevel converters for AC/AC conversion with failed modules," *2015 17th European Conference on Power Electronics and Applications (EPE'15 ECCE-Europe)*, Geneva, 2015, pp. 1-10.
- [57] R. W. Erickson and O. A. Al-Naseem, "A new family of matrix converters," *Industrial Electronics Society, 2001. IECON '01. The 27th Annual Conference of the IEEE*, Denver, CO, 2001, pp. 1515-1520 vol.2.
- [58] S. Angkititrakul and R. W. Erickson, "Control and implementation of a new modular matrix converter," *Applied Power Electronics Conference and Exposition, 2004. APEC '04. Nineteenth Annual IEEE*, 2004, pp. 813-819 vol.2.
- [59] S. Angkititrakul and R. W. Erickson, "Capacitor voltage balancing control for a modular matrix converter," *Twenty-First Annual IEEE Applied Power Electronics Conference and Exposition*, 2006. APEC '06., Dallas, TX, 2006, pp. 7 pp.-.
- [60] Y. Miura, T. Mizutani, M. Ito and T. Ise, "A novel space vector control with capacitor voltage balancing for a multilevel modular matrix converter," *2013 IEEE ECCE Asia Downunder*, Melbourne, VIC, 2013, pp. 442-448.
- [61] Y. Miura, K. Inubushi, M. Ito and T. Ise, "Multilevel modular matrix converter for high voltage applications: Control, design and experimental characteristics," *IECON 2014 - 40th Annual Conference of the IEEE Industrial Electronics Society*, Dallas, TX, 2014, pp. 4690-4696.

- [62] C. Oates, "A methodology for developing 'Chainlink' converters," *2009 13th European Conference on Power Electronics and Applications*, Barcelona, 2009, pp. 1-10.
- [63] C. Oates and G. Mondal, "DC circulating current for capacitor voltage balancing in modular multilevel matrix converter," *Proceedings of the 2011 14th European Conference on Power Electronics and Applications*, Birmingham, 2011, pp. 1-7.
- [64] F. Kammerer, J. Kolb and M. Braun, "Fully decoupled current control and energy balancing of the Modular Multilevel Matrix Converter," *2012 15th International Power Electronics and Motion Control Conference (EPE/PEMC)*, Novi Sad, 2012, pp. LS2a.3-1-LS2a.3-8.
- [65] W. Kawamura and H. Akagi, "Control of the modular multilevel cascade converter based on triple-star bridge-cells (MMCC-TSBC) for motor drives," *2012 IEEE Energy Conversion Congress and Exposition (ECCE)*, Raleigh, NC, 2012, pp. 3506-3513.
- [66] W. Kawamura and H. Akagi, "Control of the modular multilevel cascade converter based on triple-star bridge-cells (MMCC-TSBC) for motor drives," *2012 IEEE Energy Conversion Congress and Exposition (ECCE)*, Raleigh, NC, 2012, pp. 3506-3513.
- [67] W. Kawamura, M. Hagiwara and H. Akagi, "A broad range of frequency control for the modular multilevel cascade converter based on triple-star bridge-cells (MMCC-TSBC)," *2013 IEEE Energy Conversion Congress and Exposition*, Denver, CO, 2013, pp. 4014-4021.
- [68] F. Kammerer, M. Gommeringer, J. Kolb and M. Braun, "Energy balancing of the Modular Multilevel Matrix Converter based on a new transformed arm power analysis," *2014 16th European Conference on Power Electronics and Applications*, Lappeenranta, 2014, pp. 1-10.
- [69] F. Kammerer, D. Braeckle, M. Gommeringer, M. Schnarrenberger and M. Braun, "Operating Performance of the Modular Multilevel Matrix Converter in Drive Applications," *Proceedings of PCIM Europe 2015; International Exhibition and Conference for Power Electronics, Intelligent Motion, Renewable Energy and Energy Management, Nuremberg, Germany*, 2015, pp. 1-8.
- [70] M. Díaz, M. Espinoza, A. Mora, R. Cárdenas and P. Wheeler, "The application of the

- modular multilevel matrix converter in high-power wind turbines," *2016 18th European Conference on Power Electronics and Applications (EPE'16 ECCE Europe)*, Karlsruhe, 2016, pp. 1-11.
- [71] M. Diaz, R. Cárdenas, M. Espinoza, A. Mora and P. Wheeler, "Modelling and control of the Modular Multilevel Matrix Converter and its application to Wind Energy Conversion Systems," *IECON 2016 - 42nd Annual Conference of the IEEE Industrial Electronics Society, Florence*, 2016, pp. 5052-5057.
- [72] M. Diaz et al., "Control of Wind Energy Conversion Systems Based on the Modular Multilevel Matrix Converter," in *IEEE Transactions on Industrial Electronics*, vol. 64, no. 11, pp. 8799-8810, Nov. 2017.
- [73] Y. Hayashi, T. Takeshita, M. Muneshima and Y. Tadano, "Independent control of input current and output voltage for Modular Matrix Converter," *IECON 2013 - 39th Annual Conference of the IEEE Industrial Electronics Society, Vienna*, 2013, pp. 888-893.
- [74] D. Karwatzki, L. Baruschka, J. Kucka and A. Mertens, "Current control and branch energy balancing of the Modular Multilevel Matrix Converter," *2015 IEEE Energy Conversion Congress and Exposition (ECCE)*, Montreal, QC, 2015, pp. 6360-6367.
- [75] D. Karwatzki and A. Mertens, "Control approach for a class of modular multilevel converter topologies," *2016 IEEE Energy Conversion Congress and Exposition (ECCE)*, Milwaukee, WI, 2016, pp. 1-9.
- [76] D. Karwatzki, M. Dokus and A. Mertens, "Control of a three-phase to five-phase modular multilevel matrix converter based on a generalized control concept," *2017 19th European Conference on Power Electronics and Applications (EPE'17 ECCE Europe)*, Warsaw, 2017, pp. P.1-P.10.
- [77] P. Himmelmann and M. Hiller, "A Generalized Approach to the Analysis and Control of Modular Multilevel Converters," *PCIM Europe 2017; International Exhibition and Conference for Power Electronics, Intelligent Motion, Renewable Energy and Energy Management*, Nuremberg, Germany, 2017, pp. 1-8.
- [78] Y. Meng et al., "Research on Modeling and Control Strategy of Modular Multilevel Matrix Converter Based on Doubledq Coordinate Transformation," *Proceedings of the Csee*, 2016.

- [79] L. Huang, X. Yang, B. Zhang, L. Qiao, H. Li and M. Tian, "Hierarchical model predictive control of modular multilevel matrix converter for low frequency AC transmission," *2015 9th International Conference on Power Electronics and ECCE Asia (ICPE-ECCE Asia)*, Seoul, 2015, pp. 927-933.
- [80] H. Nademi, L. E. Norum, Z. Soghomonian and T. Undeland, "Low frequency operation of modular multilevel matrix converter using optimization-oriented predictive control scheme," *2016 IEEE 17th Workshop on Control and Modeling for Power Electronics (COMPEL)*, Trondheim, 2016, pp. 1-6.
- [81] B. Fan, K. Wang, P. Wheeler, C. Gu and Y. Li, "An Optimal Full Frequency Control Strategy for the Modular Multilevel Matrix Converter Based on Predictive Control," in *IEEE Transactions on Power Electronics*, vol. PP, no. 99, pp. 1-1.
- [82] W. Kawamura, K. L. Chen, M. Hagiwara and H. Akagi, "A Low-Speed, High-Torque Motor Drive Using a Modular Multilevel Cascade Converter Based on Triple-Star Arms (MMCC-TSBC)," in *IEEE Transactions on Industry Applications*, vol. 51, no. 5, pp. 3965-3974, Sept.-Oct. 2015.
- [83] W. Kawamura, Y. Chiba, M. Hagiwara and H. Akagi, "Experimental Verification of an Electrical Drive Fed by a Modular Multilevel TSBC Converter When the Motor Frequency Gets Closer or Equal to the Supply Frequency," in *IEEE Transactions on Industry Applications*, vol. 53, no. 3, pp. 2297-2306, May-June 2017.
- [84] W. Kawamura, Y. Chiba and H. Akagi, "A Broad Range of Speed Control of a Permanent Magnet Synchronous Motor Driven by a Modular Multilevel TSBC Converter," in *IEEE Transactions on Industry Applications*, vol. 53, no. 4, pp. 3821-3830, July-Aug. 2017.
- [85] D. Braeckle, F. Kammerer, M. Schnarrenberger, M. Hiller and M. Braun, "A Modular Multilevel Matrix Converter for High Speed Drive Applications," *PCIM Europe 2016; International Exhibition and Conference for Power Electronics, Intelligent Motion, Renewable Energy and Energy Management, Nuremberg, Germany*, 2016, pp. 1-8.
- [86] B. Fan, K. Wang, C. Gu, P. Wheeler and Y. Li, "A branch current reallocation based energy balancing strategy for the Modular multilevel matrix converter operating around equal frequency," *IECON 2016 - 42nd Annual Conference of the IEEE Industrial Electronics*

- Society*, Florence, 2016, pp. 3111-3116.
- [87] Y. Miura, K. Inubushi, T. Yoshida, T. Fujikawa and T. Ise, "Operation of modular matrix converter under close input and output frequency by using voltage space vector modulation," *IECON 2015 - 41st Annual Conference of the IEEE Industrial Electronics Society*, Yokohama, 2015, pp. 005136-005141.
- [88] F. Li and G. Wang. "Control Scheme of Modular Multilevel Matrix Converters for Expanding Low-frequency Operating Range." *Automation of Electric Power Systems*, 40.22, 2016.
- [89] F. Li and G. Wang. "Control Strategy for Low Frequency Operation of Modular Multilevel Matrix Converters with Similar Input and Output Frequencies." *Transactions of China Electrotechnical Society*, 2016.
- [90] D. Braeckle, P. Himmelmann, M. Schnarrenberger and M. Hiller, "Control strategy for modular multilevel matrix converters at high output frequencies," *2017 IEEE Energy Conversion Congress and Exposition (ECCE)*, Cincinnati, OH, 2017, pp. 2137-2143.
- [91] S. Shao, P. W. Wheeler, J. C. Clare and A. J. Watson, "Fault Detection for Modular Multilevel Converters Based on Sliding Mode Observer," in *IEEE Transactions on Power Electronics*, vol. 28, no. 11, pp. 4867-4872, Nov. 2013.
- [92] Y. Miura, T. Yoshida, T. Fujikawa, T. Miura and T. Ise, "Operation of modular matrix converter with hierarchical control system under cell failure condition," *2016 IEEE Energy Conversion Congress and Exposition (ECCE)*, Milwaukee, WI, 2016, pp. 1-8.
- [93] B. Fan, K. Wang, Z. Zheng, L. Xu and Y. Li, "Optimized Branch Current Control of Modular Multilevel Matrix Converters Under Branch Fault Conditions," in *IEEE Transactions on Power Electronics*, vol. 33, no. 6, pp. 4578-4583, June 2018.
- [94] D. Karwatzki, M. von Hofen, L. Baruschka and A. Mertens, "Operation of modular multilevel matrix converters with failed branches," *IECON 2014 - 40th Annual Conference of the IEEE Industrial Electronics Society*, Dallas, TX, 2014, pp. 1650-1656.
- [95] F. Li and G. Wang. "Steady-state Analysis of Sub-modular Capacitor Voltage Ripple in Modular Multilevel Matrix Converters." *DianjiGongchengXuebaoChina /proceedings of the Chinese Society of Electrical Engineering*, 33.24(2013):52-58.

- [96] High Quality Capacitors. ELNA co., Ltd, [http:// www. elna. co. jp/ en/ capacitor/ pdf/ catalog_13_14_e.pdf](http://www.elna.co.jp/en/capacitor/pdf/catalog_13_14_e.pdf)
- [97] Global Wind Report Annual Market Update. [http://files.gwec.net/files/GWR2016. pdf.](http://files.gwec.net/files/GWR2016.pdf)
Accessed 4 June 2017.